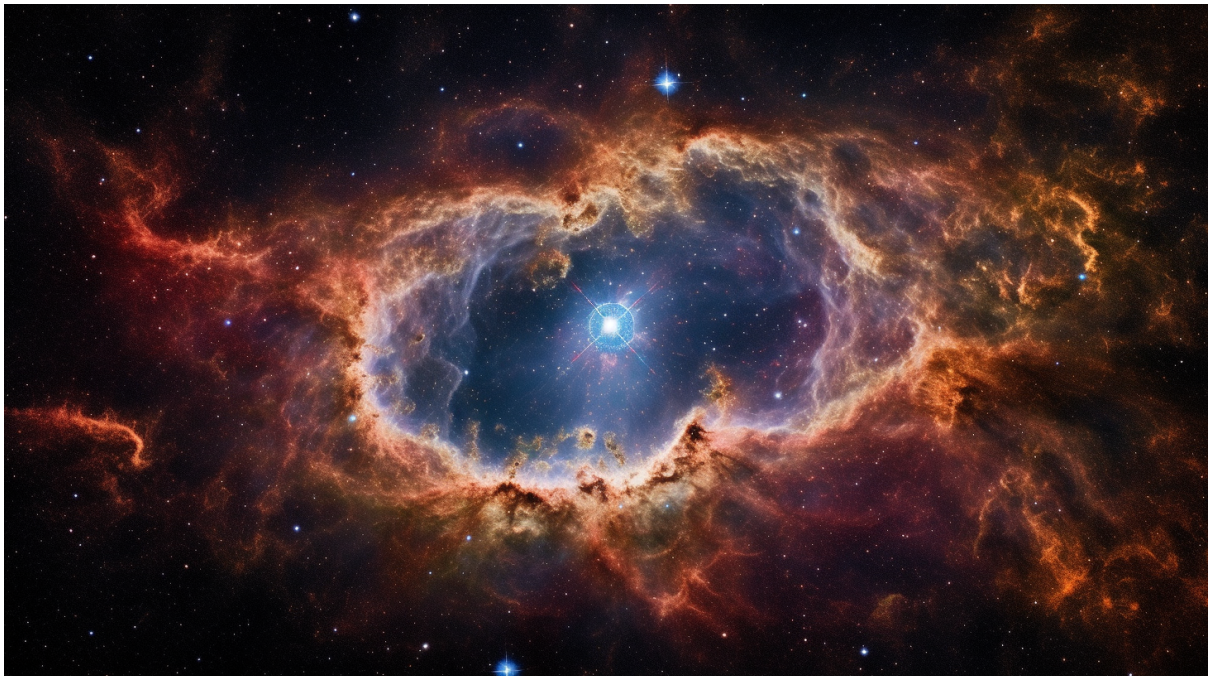


OBSERVATION OF COSMIC GAMMA-RAY BURSTS WITH THE ASIM  
MISSION ONBOARD THE INTERNATIONAL SPACE STATION



Master Thesis in Space Physics

by

**Andreas Ramsli**

Department of Physics and Technology  
University of Bergen  
Norway  
May 2, 2023



# Contents

|          |   |           |
|----------|---|-----------|
| <b>1</b> | <b>Introduction</b>                                     | <b>6</b>  |
| <b>2</b> | <b>Cosmic Gamma-Ray Bursts (GRBs)</b>                   | <b>7</b>  |
| <b>3</b> | <b>Instruments and datasets</b>                         | <b>11</b> |
| 3.1      | General Overview of Instruments . . . . .               | 11        |
| 3.2      | ASIM instrument . . . . .                               | 13        |
| 3.2.1    | MXGS instrumental effects . . . . .                     | 14        |
| 3.3      | Konus-WIND instrument . . . . .                         | 15        |
| 3.4      | Fermi Instrument . . . . .                              | 16        |
| 3.5      | Datasets . . . . .                                      | 17        |
| <b>4</b> | <b>Methods</b>  | <b>18</b> |
| 4.1      | GRB Identification in ASIM . . . . .                    | 18        |
| 4.2      | ASIM Data Preparation . . . . .                         | 18        |
| 4.2.1    | Cross Correlation of Light Curves . . . . .             | 18        |
| 4.3      | Basics of Spectral Fitting . . . . .                    | 19        |
| 4.3.1    | Xspec . . . . .   | 19        |
| 4.3.2    | Spectra . . . . .                                       | 19        |
| 4.3.3    | Response Files . . . . .                                | 20        |
| 4.3.4    | Models . . . . .  | 22        |
| 4.3.5    | Fitting Procedure . . . . .                             | 22        |
| 4.4      | ASIM Data Analysis Consistency Check . . . . .          | 23        |
| 4.5      | Fermi/GBM Data Preparation . . . . .                    | 23        |
| <b>5</b> | <b>Results &amp; Discussions</b>                        | <b>24</b> |
| 5.1      | ASIM GRB database . . . . .                             | 24        |
| 5.2      | Joint Spectral Analysis . . . . .                       | 28        |
| 5.3      | ASIM Data Analysis Pipeline Consistency Check . . . . . | 34        |
| 5.3.1    | Light Curve Analysis . . . . .                          | 34        |
| 5.3.2    | Background Ratemeter Analysis . . . . .                 | 34        |
| 5.3.3    | DRM Analysis . . . . .                                  | 36        |
| 5.3.4    | Energy Calibration Coefficients Analysis . . . . .      | 37        |
| 5.3.5    | Consistency of the Mass Model . . . . .                 | 38        |
| 5.3.6    | ASIM FITS Analysis . . . . .                            | 38        |
| 5.4      | Case Studies . . . . .                                  | 39        |
| 5.4.1    | GRB 210619B . . . . .                                   | 39        |
| 5.4.2    | GRB 211211A . . . . .                                   | 41        |
| <b>6</b> | <b>Summary and outlook</b>                              | <b>44</b> |
| <b>A</b> | <b>GRB Archive</b>                                      | <b>45</b> |
| A.1      | GRB 181222B . . . . .                                   | 45        |
| A.1.1    | KW spectra . . . . .                                    | 47        |
| A.2      | GRB 190206A . . . . .                                   | 48        |
| A.2.1    | KW spectra . . . . .                                    | 49        |
| A.3      | GRB190305A . . . . .                                    | 50        |
| A.3.1    | KW spectra . . . . .                                    | 51        |
| A.4      | GRB 190606A . . . . .                                   | 52        |
| A.4.1    | KW spectra . . . . .                                    | 53        |
| A.5      | GRB 200521A . . . . .                                   | 54        |
| A.5.1    | KW spectra . . . . .                                    | 55        |
| A.6      | GRB 200716C . . . . .                                   | 56        |
| A.6.1    | KW spectra . . . . .                                    | 57        |
| A.7      | GRB 201227A . . . . .                                   | 58        |
| A.7.1    | KW spectra . . . . .                                    | 59        |
| A.8      | GRB 210619B . . . . .                                   | 61        |

|          |   |           |
|----------|---|-----------|
| A.8.1    | KW spectra . . . . .                                    | 63        |
| A.9      | GRB 211211A . . . . .                                   | 64        |
| <b>B</b> | <b>ASIM Data Processing and Spectral Analysis Tools</b> | <b>67</b> |
|          | <b>Bibliography</b>                                     | <b>68</b> |

## Acknowledgements

This thesis is the culmination of tireless efforts and invaluable insights from the brilliant minds who have come before me. They have laid the foundation upon which I stand, allowing me to reach further and build on their accomplishments. I am truly standing on the shoulders of giants.

I am deeply grateful for the mentorship and guidance provided by my primary supervisor, Martino Marisaldi, at the Birkeland Centre for Space Science (BCSS). His keen intellect and profound understanding of the field have been instrumental in shaping this thesis. His willingness to engage in dialogue and offer assistance has been invaluable. I feel truly honored to have had the opportunity to work with and learn from such a remarkable individual. His guidance during my bachelor's studies on Terrestrial Gamma-rays (TGFs) paved the way for our continued collaboration throughout my master's degree.

My heartfelt gratitude goes to my co-supervisor, David Sarria, also at BCSS, for his sharp mind and significant contributions to this thesis. His expertise has been crucial in realizing this work.

I would like to express my appreciation to Anders Lindanger for his insightful guidance during the early stages of my thesis work. Though he eventually moved on to new opportunities, his initial support as a co-supervisor left a lasting impact.

I am also profoundly grateful to the international scientists Cristiano Guidorzi from the University of Ferrara, Italy; Anastasia Tsvetkova, of the Konus-WIND team, now at the University of Cagliari, Italy; and María Caballero-García at the Instituto de Astrofísica de Andalucía, Glorieta de la Astronomía, Granada. Their vast expertise and comprehensive knowledge of the field have significantly enhanced my work.

Finally, I would like to extend my thanks to Andrey Mezentsev (also at BCSS) for sharing his expertise, which has been essential in navigating the complexities of the ASIM data. His guidance has been indispensable in making this thesis possible.

I would be remiss if I did not express my heartfelt gratitude to my family and friends for their unwavering support and encouragement throughout this thesis work. Their belief in me and understanding have been a constant source of strength, and their contributions, both large and small, have played a pivotal role in the realization of this thesis. I am truly grateful for their presence in my life and for the countless ways they have uplifted and inspired me.

From an early age, I have been mesmerized by the mysteries of space and the universe, a fascination that has only intensified over time. I am extremely grateful to have had the opportunity to delve into a field that I find not only deeply captivating but also truly inspiring. I would like to express my gratitude to the Birkeland Centre for Space Science for providing me with the chance to work on this thesis. The universe is filled with remarkable cosmic wonders, and through this thesis, I have had the unique privilege of investigating and learning about these exceptional phenomena.

The research presented in this thesis has been supported by funding from the European Union's Horizon 2020 Programme, specifically through the AHEAD2020 project (grant agreement no. 871158).

## Abstract

This thesis investigates the detection of cosmic gamma-ray bursts (GRBs) by the Atmosphere-Space Interactions Monitor (ASIM) mission, which primarily focuses on terrestrial gamma-ray flashes (TGFs). From June 1st, 2018, to December 31st, 2021, ASIM identified 12 GRBs, significantly expanding its scientific scope. ASIM's capabilities as a GRB detector were demonstrated through the detection of a magnetar flare, as detailed in Castro-Tirado et al. (2021).

A comprehensive methodology for joint spectral analysis of GRBs was developed, involving GRB identification, ASIM and Fermi data preparation, cross-correlation of light curves, spectral fitting, and data consistency verification. This approach utilized the ASIM trigger list, InterPlanetary Network (IPN), GRBweb collaboration, and custom software for data handling and spectral fitting.

Notable findings include the detection of GRB 210619B, a kilonova in a distant dwarf galaxy at a redshift of  $z = 1.937$ , ranking among the top 10 most luminous bursts detected by the Fermi/GBM gamma-ray monitor. The spectral analysis of GRB 211211A suggests a merger between a  $1.23 M_{\odot}$  neutron star and an  $8.21 M_{\odot}$  black hole, with a Super Flare observed in the precursor of the burst, believed to result from the destruction of a highly magnetized magnetar.

In conclusion, ASIM has proven effective as a GRB detector, with 12 GRBs identified over 3.5 years. Despite discrepancies in the cross-calibration constant, the spectra were successfully fitted, yielding a satisfactory reduced  $\chi^2$ . This work extends the scientific impact of ASIM beyond its primary mission goals and has resulted in publication in collaboration with international partners (Caballero-García et al., 2023). The current work will be compiled into a paper, submitted to an Astrophysics journal in collaboration with international partners.

# 1 Introduction

The first systematic exploration of cosmological Gamma-Ray Bursts (GRBs) detected by the Atmosphere-Space Interactions Monitor (ASIM), in conjunction with observations from Konus-WIND (KW) and the Fermi Gamma-ray Burst Monitor (Fermi/GBM), was conducted in this thesis. The capabilities of ASIM as a GRB detector were investigated, and its performance was cross-validated with other spacecraft. ASIM is renowned for its ability to detect magnetar flares, as reported by Castro-Tirado et al. (2021), and its high sensitivity and rapid detection time render it well-suited for GRB observation.

The primary objective of this thesis was to investigate the capabilities of the Atmosphere-Space Interactions Monitor (ASIM) as a gamma-ray burst (GRB) detector and to cross-validate its performance with other spacecraft. ASIM, a European Space Agency mission, was launched in April 2018 and is hosted onboard the International Space Station (ISS). It is dedicated to studying the physics of Transient Luminous Events (TLEs) and Terrestrial Gamma-ray Flashes (TGFs) and their relation to lightning, with its primary instrument being the Modular X-ray and Gamma-ray Sensor (MXGS). However, ASIM has also observed cosmic events, such as the magnetar flare detailed in Castro-Tirado et al. (2021).

To assess ASIM's GRB detection capabilities, a database of GRBs detected by ASIM was compiled as the primary dataset, and data from Konus-WIND and the Fermi Gamma-ray Burst Monitor (GBM) were cross-correlated to validate the performance of ASIM's MXGS. This thesis presents 12 confirmed GRBs identified by ASIM, along with a detailed description of the methods used for joint spectral analysis, model parameters, and a consistency check of the ASIM data preparation pipeline. Furthermore, a dedicated case study section highlights two peculiar GRBs and their origins.

During the course of this thesis, the opportunity to collaborate with esteemed researchers at the Birkeland Centre for Space Science (BCSS) was invaluable. Working with these experts provided unique insights into the field, enabling the acquisition of essential knowledge, the refinement of skills, and a broader understanding of the subject matter. This experience at BCSS greatly enriched the academic journey and contributed to the successful completion of the thesis.

A significant portion of the research conducted in this thesis was dedicated to preparing ASIM and Fermi data for joint spectral analysis of numerous GRBs. This process required the development of customized software for processing ASIM data in spectral fitting. Consequently, the ASIM Fits program was created to facilitate the generation of FITS files for ASIM data, enhancing the effectiveness of the data analysis pipeline and serving as a fundamental tool for further exploration of GRB science capabilities with ASIM.

Proficiency in using the modeling software Xspec for fitting GRB spectra with advanced models was gained during a visit from July 4th to July 8th, 2022, through the AHEAD 2020 Trans-national access program in computational astrophysics at the Università di Ferrara, Italy. Essential guidance on the procedure was provided by a key expert in the field, making this experience invaluable. The KW spectral files for the selected GRBs were kindly provided by the Konus-WIND team, who also imparted valuable knowledge regarding the spectral fitting and cross-correlation process.

The European Geosciences Union (EGU) general assembly in Vienna, Austria, has accepted my attendance from April 24th to April 28th, 2023. I will present a poster showcasing the interesting results obtained in this thesis. An abstract, titled "Validation of the ASIM MXGS performance using cosmic Gamma-Ray Bursts," has been accepted for the conference, with me as the first author.

An article was published in the Monthly Notices of the Royal Astronomical Society (Caballero-García et al., 2023) based on the joint spectral fit analysis of GRB 210619B in collaboration with a group from Granada, Spain. Moreover, an upcoming paper in a peer-reviewed journal will detail our collaboration with the same Spanish team on GRB 211211A, which involved a joint spectral fit using ASIM, Fermi/GBM, and Swift data. Additionally, the ASIM team at the Birkeland Centre for Space Science and the KW-team are collaborating on a dedicated paper that incorporates the results from this thesis, currently being prepared for publication in the *Astronomy & Astrophysics* journal.

## 2 Cosmic Gamma-Ray Bursts (GRBs)

Imagine harnessing the energy from every star within thousands of galaxies, each containing billions of stars. This extraordinary phenomenon, known as Gamma-Ray Burst (GRB), truly exists.

To comprehend Gamma-Ray Bursts (GRBs), we must first understand gamma rays. Gamma rays are a form of electromagnetic radiation, which consists of waves that carry energy through space. Visible light represents only a minuscule portion of the electromagnetic spectrum, with lower-energy waves like radio waves, microwaves, and infrared waves, and higher-energy waves such as ultraviolet, X-rays, and gamma-rays. These Gamma-rays possess extraordinary potency, with the energy carried by a single gamma-ray photon surpassing that of a million photons of visible light. This heightened energy characterizes gamma rays as ionizing radiation, signifying their capacity to disintegrate atomic bonds, rendering them hazardous to living organisms.

Figure 1 provides an illustration of the observable universe in a logarithmic scale, which condenses a vast range of values into an easily comprehensible format. This enables us to visualize and compare both the minuscule and enormous aspects of the universe in a single figure and provides a sense of the cosmic scale of GRBs. The observable universe is estimated to be around  $\sim 14$  billion years old (Knox et al., 2001), and it expands over an astonishing distance of about 28,400 Mpc or 93 billion light years (Halpern and Tomasello, 2016), while continuing to expand. ASIM detects cosmic Gamma-Ray Bursts that originate from distant galaxies far away, some of which have journeyed for several billion years. If the distance of these GRBs were to be mapped to the figure, they would originate at the inner edge of the second ring (counting outwards from the Sun), where galaxies and galactic clusters are found.

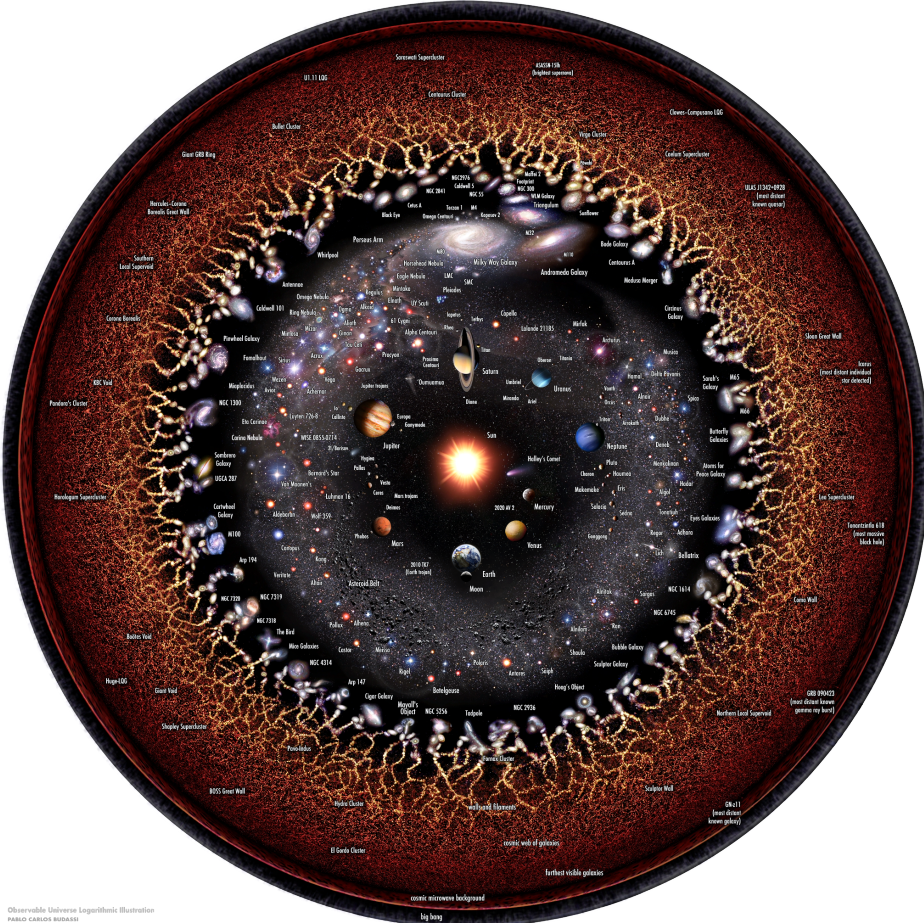


*Figure 1: Illustration of the observable universe on a logarithmic scale with the Sun in center <sup>1</sup>*

<sup>1</sup>Retrieved from: [https://it.wikipedia.org/wiki/File:Observable\\_Universe\\_logarithmic\\_illustration\\_\(circular\\_layout\\_english\\_annotations\).png](https://it.wikipedia.org/wiki/File:Observable_Universe_logarithmic_illustration_(circular_layout_english_annotations).png)

Earth's atmosphere absorbs gamma rays, protecting us from their harmful effects. However, this raises the question: how were GRBs from space discovered if our atmosphere blocks them? The answer lies in the USA's spy satellites, which were designed to detect gamma rays from potential nuclear bomb tests. While they didn't find any bombs, these satellites did observe faint bursts of gamma rays, leading to the discovery of GRBs. The first GRB was detected on July 2, 1967, by the Vela satellites. A catalog of the detected GRBs by the Vela satellites can be found in Strong et al. (1974).

Following the discovery of GRBs by the Vela satellites, several important missions played crucial roles in advancing our understanding of these mysterious phenomena. The Burst and Transient Source Experiment (BATSE) onboard the Compton Gamma-Ray Observatory (CGRO) provided significant insights into the isotropic distribution and intensity of GRBs (Harmon et al., 2001). Isotropic distribution refers to the uniformity of GRB events in all directions across the sky. The data collected by BATSE showed that GRBs were not preferentially concentrated in any particular direction or region of the sky. This isotropic distribution was an essential clue that suggested the extragalactic nature of GRBs, as events within our galaxy would have been more likely to cluster along the galactic plane. CGRO was operational from 1991 to 2000, and BATSE detected over 2,700 GRBs during its lifetime, leading to a better understanding of the characteristics and properties of these events (Harmon et al., 2001; Paciesas et al., 1999).

The Italian-Dutch satellite BeppoSAX, launched in 1996, was another vital mission in the GRB field. BeppoSAX was the first to identify an X-ray afterglow associated with a GRB, leading to the localization of GRBs and the discovery of their host galaxies (Wijers et al., 1997; Van Paradijs et al., 1997). This breakthrough helped to establish that GRBs were of extragalactic origin and at cosmological distances.

In the early 21st century, the Swift satellite, launched in 2004, became a key player in GRB research. Swift was designed specifically for the rapid detection and follow-up of GRBs, with its Burst Alert Telescope (BAT) detecting and localizing GRBs, followed by its narrow-field X-ray and UV/optical telescopes observing the afterglows (Gehrels et al., 2004). Swift has observed over 1,500 GRBs since its launch, providing valuable data on the prompt emission and afterglow phases of these events (Gehrels et al., 2004).

Today, thanks to these pioneering missions and continued advancements in gamma-ray detection, we detect approximately one GRB every day (Zhang, 2018). The study of GRBs has provided valuable insights into some of the most energetic and distant phenomena in the universe, making it a continually evolving and exciting field of research.

GRBs are associated with some of the most violent, cataclysmic events in the universe and the formation of black holes (Taylor and Wheeler, 2000). GRBs have huge amounts of energy and, more importantly, exhibit the highest isotropic luminosities in the universe. Isotropic luminosity refers to the total amount of electromagnetic radiation emitted per unit time by an astronomical object, such as a star, galaxy, or quasar, assuming that the emission is uniform in all directions.

Building upon these insights, researchers classified GRBs into two primary categories: long-duration GRBs (LGRBs) and short-duration GRBs (SGRBs), each with distinct origins. Figure 2 illustrates this distinction<sup>2</sup>. LGRBs, persisting for more than 2 seconds, are believed to occur during the final stages of massive star evolution when the stellar core collapses to form a black hole. In contrast, SGRBs, with durations of less than 2 seconds, are thought to result from mergers between neutron stars or a neutron star and a black hole, ultimately leading to black hole formation (Zhang, 2018).

Now, in both scenarios, the resulting black hole find itself surrounded by a magnetized accretion disk composed of gas remnants from its progenitor stars. As the black hole's rotation amplifies the magnetic field, channeling hot, relativistic particle jets. The gas within these jets generates two highly focused beams of high-energy gamma rays, acting like celestial laser beams. Unlike other cosmic explosions that disperse and diminish over time, GRBs maintain their focus and can be observed from billions of light-years away.

The standard fireball model, as described by Zhang (2018), offers a widely-accepted framework for understanding the basic physics of GRBs. Now, this model suggests that the initial energy release in a GRB occurs in the form of a highly relativistic outflow, or "fireball," composed of radiation and matter. As the fireball expands, it interacts with the surrounding medium, producing internal shocks and external

<sup>2</sup>Retrieved from <https://esahubble.org/images/opo0620h>

## Gamma-Ray Bursts (GRBs): The Long and Short of It

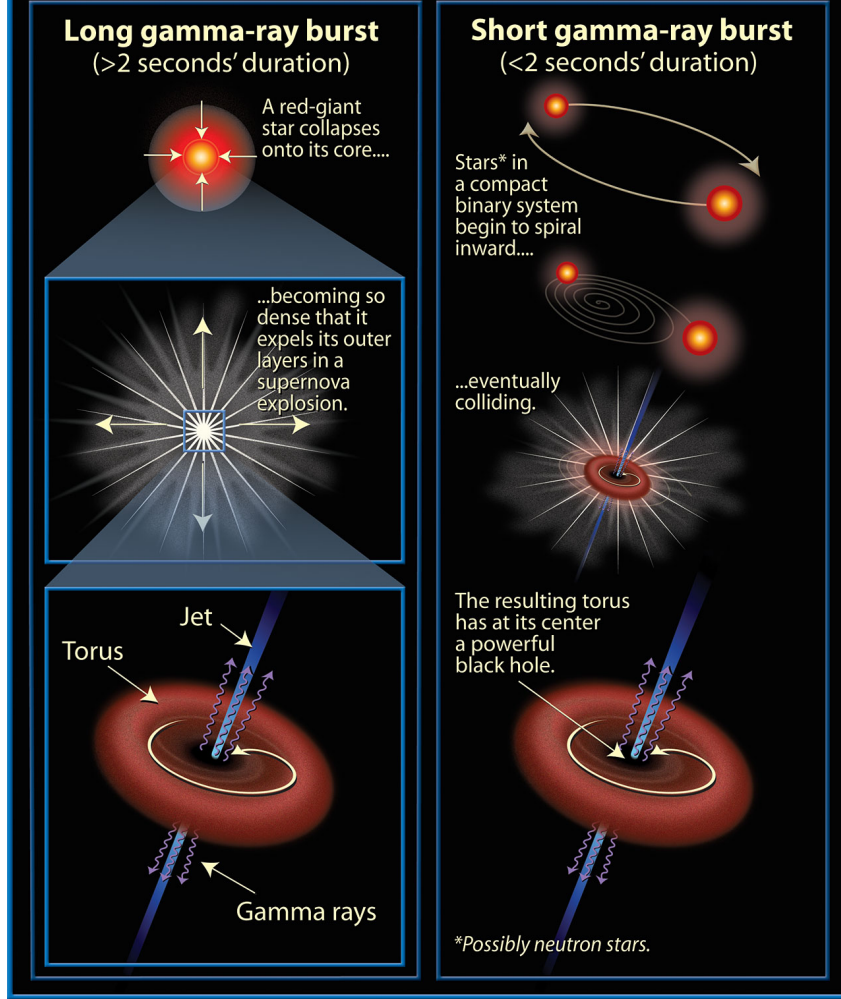


Figure 2: Illustration of the primary classification of GRBs

shocks. The intriguing part is that these shock processes are responsible for the emission of gamma rays and afterglow emission at lower frequencies, such as X-rays, optical, and radio waves.

Various processes, such as inverse Compton scattering, synchrotron radiation, and photon-photon pair production, are involved in the generation of gamma rays. High-energy particles in the fireball collide with photons in these interactions, resulting in the transfer of energy and the creation of a cascade of gamma-ray photons (Zhang, 2018).

As we delve deeper into the mysteries of GRBs, an intriguing aspect of their observation is the transition from thermal to non-thermal emission. In the early stages of a GRB, the emission is predominantly thermal, characterized by a blackbody spectrum. However, as the fireball expands and the relativistic particles interact with the surrounding medium, the emission transitions to a non-thermal spectrum (Zhang, 2018).

Three fundamental processes play a crucial role in shaping the non-thermal spectrum observed in GRBs: synchrotron radiation, inverse Compton scattering, and pair production. Synchrotron radiation is emitted when relativistic charged particles spiral in a magnetic field, producing a power-law spectrum (Rybicki and Lightman, 1991). Inverse Compton scattering, on the other hand, involves the scattering of low-energy photons to high energies by ultrarelativistic electrons, causing the photons to gain and the electrons to lose energy. This process is called inverse because the electrons lose energy rather than the photons, the opposite of the standard Compton effect (Sunyaev and Titarchuk, 1980).

Pair production is another key process in GRBs, where high-energy gamma-ray photons interact with

lower-energy photons or matter to create an electron-positron pair (Gould and Schréder, 1967). This process occurs when the energy of the gamma-ray photon is sufficient to create the mass of an electron and positron, and it plays a significant role in the attenuation and energy transfer within the GRB environment.

Together, synchrotron radiation, inverse Compton scattering, and pair production contribute to the complex, non-thermal signatures observed in GRBs, shedding light on the underlying physics of these cosmic events.

The GRB phenomenon continues to pose several open questions, as comprehensively discussed by Zhang (2018). Some of the most significant unresolved issues include:

- GRB jet composition and energy dissipation: The nature and composition of GRB jets remain uncertain, as does the specific mechanism(s) responsible for converting energy from other forms into radiation within these jets.
- Central engines and progenitors: The central engines driving GRBs are not well understood, and it is unclear whether there are different types, such as hyper-accreting black holes or millisecond magnetars. Additionally, the progenitors of both long and short GRBs are yet to be definitively identified, and the possibility of more than two types of progenitors remains open.
- Non-electromagnetic signals and cosmological implications: GRBs may emit non-electromagnetic signals, such as high-energy neutrinos, gravitational waves, and ultra-high-energy cosmic rays. Furthermore, GRBs can be used as indicators of the star formation history of the universe. The detection of gravitational waves from short-duration GRBs, as demonstrated by the groundbreaking observation of GW170817/GRB 170817A, in Abbott et al. (2017), has further established the potential of multi-messenger astronomy to provide unique insights into the astrophysics of compact object mergers and the nature of dense objects.

These open questions highlight the complexity of the GRB problem and emphasize the need for ongoing research to better understand the underlying mechanisms and broader implications of these enigmatic cosmological events.

### 3 Instruments and datasets

#### 3.1 General Overview of Instruments

| Parameters                      | KW                     |                         | ASIM                    |                          | FERMI                     |  |
|---------------------------------|------------------------|-------------------------|-------------------------|--------------------------|---------------------------|--|
|                                 | S1/S2                  | LED                     | HED                     | 12 × NaI                 | 2 × BGO                   |  |
| Orbit                           | $L_1$                  |                         | LEO                     |                          | LEO                       |  |
| Inclination                     | —                      |                         | 51.6°                   |                          | 25.6°                     |  |
| Launched                        | 1994                   |                         | 2018                    |                          | 2008                      |  |
| Energy Range                    | 0.020-15 MeV           | 20 - 400 keV            | 0.3 - 40 MeV            | 8 keV - 1 MeV            | 0.2 - 40 MeV              |  |
| Effective Area                  | 80-160 cm <sup>2</sup> | 100-300 cm <sup>2</sup> | 100-900 cm <sup>2</sup> | 10-110 cm <sup>2</sup> * | 100-200 cm <sup>2</sup> * |  |
| Detector Material               | NaI(Tl)                | CdZnTe                  | BGO                     | NaI(Tl)                  | BGO                       |  |
| Detector Type                   | Scintillator           | Semiconductor           | Scintillator            | Scintillator             | Scintillator              |  |
| Spectral data time resolution   | 64 ms - 8.192 s        | 0.3-20 ms               | 0.3-20 ms               | 64 ms - 1.024s           | 64 ms - 1.024s            |  |
| Total duration of spectral data | 79-492 s               | 2 s                     | 2 s                     | >330 s                   | >330 s                    |  |
| Time resolution of light curves | 2 ms - 256 ms          | 1 $\mu$ s               | 27.8 ns                 | 2 $\mu$ s                | 2 $\mu$ s                 |  |
| Dead-time                       | 40 $\mu$ s             | 1.4 $\mu$ s             | 550 ns                  | 2.6 $\mu$ s              | 2.6 $\mu$ s               |  |

Table 1: Key characteristics of the instruments used in this work

\* For each detector

In this thesis, we use data from three different gamma-ray instruments: Atmospheric Space Interactions Monitor (ASIM), Konus-Wind (KW), and Fermi Gamma-ray Burst Monitor (GBM). The instruments have distinct capabilities and specifications, which are crucial for understanding and interpreting the data they provide. We choose these two instruments because of their role as important and reliable GRB monitors with good access to their spectral data, their complementary energy ranges, and their overlapping operational periods, allowing for simultaneous observations of GRBs. Additionally, the established cross-calibration between KW and Fermi/GBM facilitates the validation of ASIM's MXGS measurements (Lipunov et al., 2016).

Table 1 provides a summary of key parameters for each gamma-ray instrument, including orbit, inclination, launch year, energy range, effective area, detector material, detector type, spectrum accumulation time, total duration, time resolution, and dead-time. The effective area represents the detector's sensitive region contributing to the detected signal, while the trigger time indicates the duration needed for the instrument to switch from waiting to triggered mode upon detecting a gamma-ray event. The total duration signifies the time during which the spectrum is accumulated, with Fermi continuously accumulating and downlinking the spectrum to Earth. Dead-time is the interval during which a detector is unable to process new incoming signals due to the processing of a previous event. It can result in the loss of information about subsequent events that occur during this period.

Semiconductor detectors, such as CZT, directly convert incident gamma-ray photons' energy into an electrical signal by generating electron-hole pairs within the crystal lattice (Knoll, 2010). In contrast, scintillator detectors like NaI or BGO, coupled with PMTs, rely on the emission of lower-energy photons (scintillation light) produced by gamma-ray photon interactions, which are then converted into an electrical signal using PMTs (Knoll, 2010; Leo, 2012).

Gamma-ray detection involves capturing high-energy photons using specialized crystals like NaI, CZT, and BGO (Knoll, 2010). Gamma-ray photons interact with crystal materials through various processes, such as photoelectric absorption and Compton scattering, depending on the photon's energy and crystal properties (Knoll, 2010). In photoelectric absorption, a gamma-ray photon is absorbed by an atom, ejecting an inner-shell electron, which is replaced by an outer-shell electron, emitting a secondary photon. Compton scattering involves a gamma-ray photon interacting with a loosely bound electron, causing the photon to change direction and lose energy.

Scintillation light, emitted as lower-energy photons, is collected and converted into an electrical signal by PMTs or other photosensors (Knoll, 2010). The PMT amplifies the signal by releasing secondary electrons upon scintillation light absorption (Leo, 2012). This current is proportional to the original gamma-ray photon's energy, and readout electronics process it to extract information about the photon's energy, arrival time, and possibly its direction (Knoll, 2010).

Figure 3 illustrates the positions of the three spacecraft in the solar system. KW is located at the Earth-Sun  $L_1$  Lagrange point, which provides a stable environment for long-term monitoring of gamma-ray bursts. ASIM and Fermi, on the other hand, operate in low Earth orbits (LEO), allowing for detailed observations and analyses of GRBs from different perspectives.

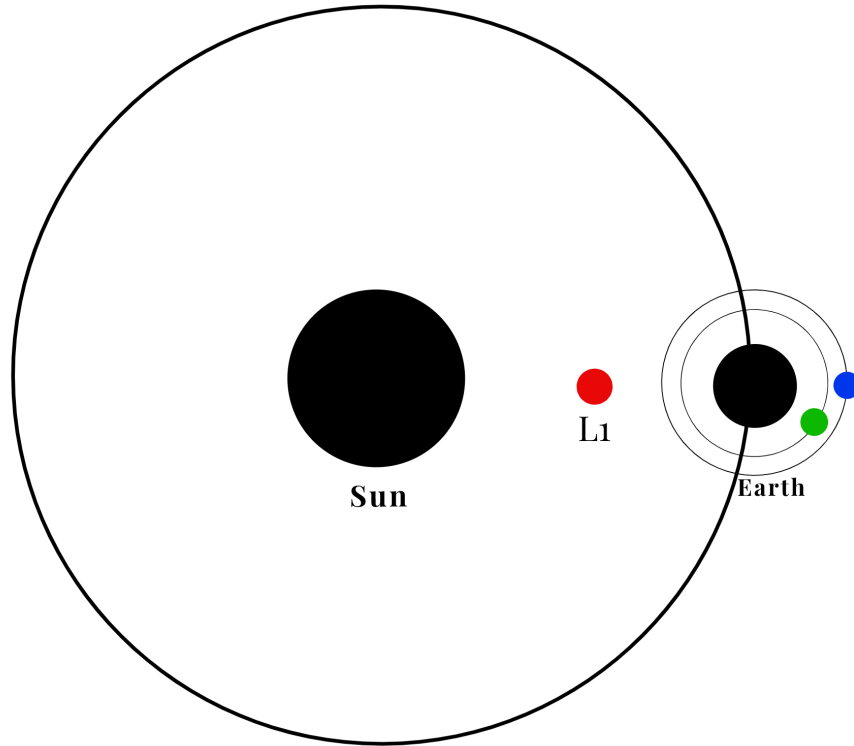


*Figure 3: KW is located at  $L_1$  and ASIM and Fermi is in low Earth orbit*

### 3.2 ASIM instrument

The Atmosphere-Space Interactions Monitor (ASIM) is a mission of the European Space Agency launched by SpaceX in April 2018 and hosted onboard the International Space Station (ISS) (Neubert et al., 2019), which is in low Earth orbit (LEO) with an orbital inclination of 51.6°. ASIM is dedicated to studying the physics of Transient Luminous Events (TLEs) and Terrestrial Gamma-ray Flashes (TGFs) and their relation to lightning. However, it has also made observations of cosmic events such as the magnetar flare described in Castro-Tirado et al. (2021). ASIM detects TGFs and other transient events by means of the Modular X- and Gamma-ray Sensor (MXGS) (Østgaard et al., 2019). The Modular Multispectral Imaging Assembly (MMIA) includes two cameras and three high speed photometers used for lightning and TLE detection. These two instruments make up the scientific payload onboard ASIM.

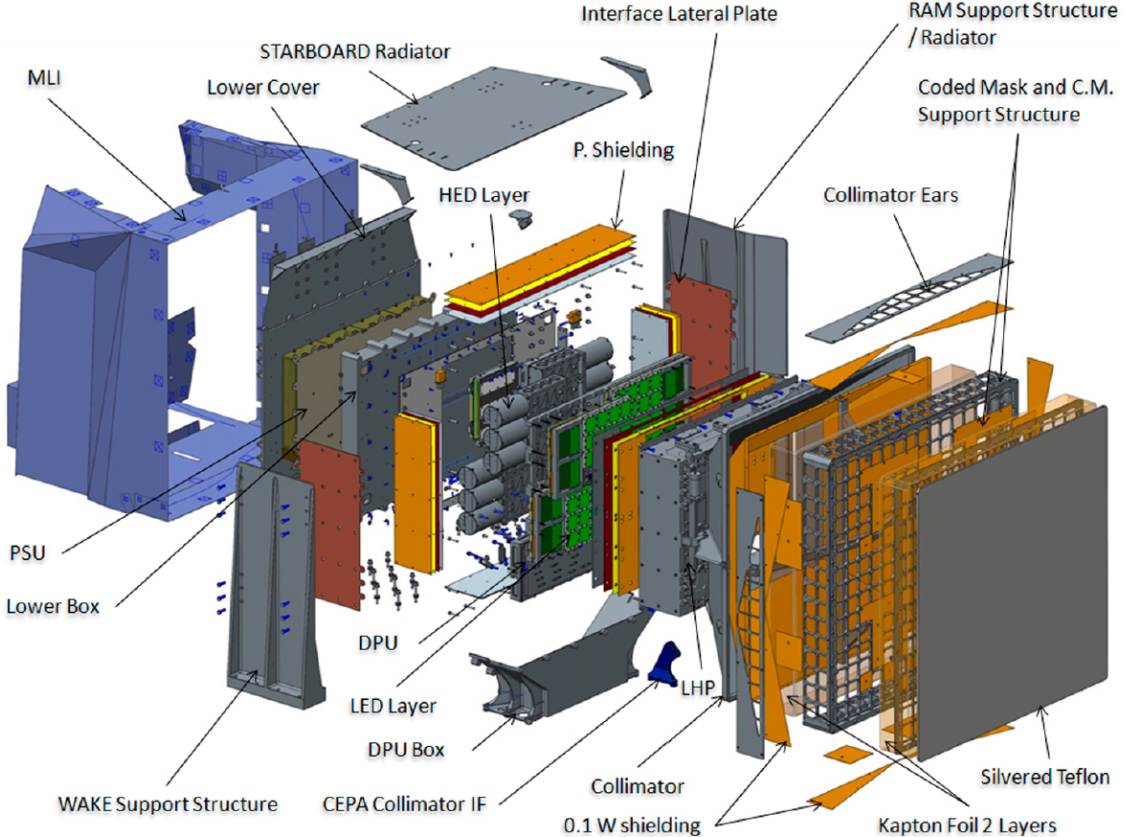


Figure 4: Exploded view of MXGS, taken from Østgaard et al. (2019)

In this study, the primary instrument utilized is the MXGS, which is composed of two parts, the Low Energy Detector (LED) and High Energy Detector (HED). The HED consists of 12 Bismuth-Germanium-Oxide (BGO) scintillators, each connected to a photomultiplier tube (PMT), capable of detecting photon energies between 300 keV and > 40 MeV, with a time resolution of 27.8 ns and a dead-time of ~ 550 ns. The LED consists of pixelated Cadmium-Zink-Telluride (CZT) detector crystals that are sensitive to photons energies between 20 to 400 keV, with a time resolution of ~ 1μs. The MXGS is mounted on the starboard side of the Columbus module (Figure 17) and has an absolute timing accuracy between ~ -10 ms and ~ 30 ms due to non-optimal timing interface between the ASIM payload and the ISS. However, we are able to correct the absolute timing accuracy with appropriate cross-correlation of light curves (LCs) from other  $\gamma$ -ray monitors used in this analysis.

The MXGS has two principal objectives: to image and capture the spectrum of X- and gamma-rays from TGFs, and for Modular Multi-Spectral Imaging Assembly (MMIA) to conduct high-speed photometry of Transient Luminous Events (TLEs) and lightning discharges (Østgaard et al., 2019; Neubert et al., 2019). TGFs are localized and infrequently observed simultaneously by multiple instruments, making GRBs a valuable calibration resource. Initially discovered in 1991 by the Burst and Transient Source Experiment (BATSE) on the Compton Gamma-Ray Observatory, TGFs were reported by Fishman et al. (1994) a few

years later. These phenomena present themselves as short-lived flashes during thunderstorms, lasting less than a millisecond and possessing energies above of 40 MeV.

### 3.2.1 MXGS instrumental effects

MXGS have various modes of operation, but the primary source of data used in this analysis are of the type; TGF Event Observation. When a trigger event occurs in MXGS or when an external trigger is received from MMIA (or both), all detector raw count data for a period of 2 seconds, approximately centered on the time of the trigger ( $T_0$ ), are downlinked via telemetry for detailed analysis on ground. Continuous adjustment of trigger thresholds is done to maintain approximately constant false trigger rates due to in-orbit variability of detector backgrounds. To prevent PMT ageing and degradation due to high fluxes of charged background particles, PMT high voltages are switched off during South Atlantic Anomaly (SAA) passages. Detailed information of the modes of operation and trigger mechanism can be found in Østgaard et al. (2019).

When a high energy particle hits the HED, a voltage drop occurs over the dynode chain in the PMTs. The voltage drop causes the measured energy of the recorded count to be lower than the actual energy. To ensure that the high voltage is restored before the next count, a safety-time (ST) criteria is applied, which is dependent on the energy of the previous count. Therefore, counts that fall within the ST-criteria are discarded before the spectrum accumulation. Note that the ST criteria was first introduced for the spectral analysis of TGFs, and the criteria is discussed in Lindanger et al. (2021). An interpolation of the ST as a function of energy for BGO detector with address 1 can be found in Figure 5. In our data analysis, we only use 'normal'-events, which are well separated counts in time.

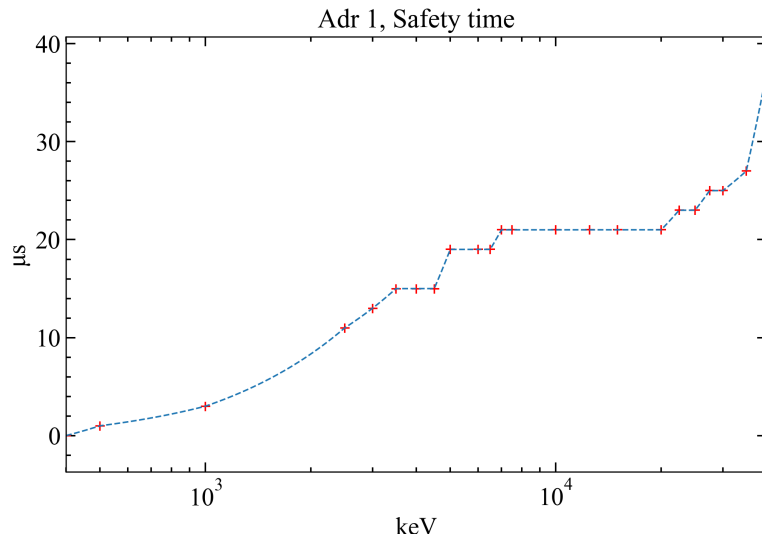


Figure 5: Example of ST as a function of energy for BGO detector in HED with address 1

### 3.3 Konus-WIND instrument

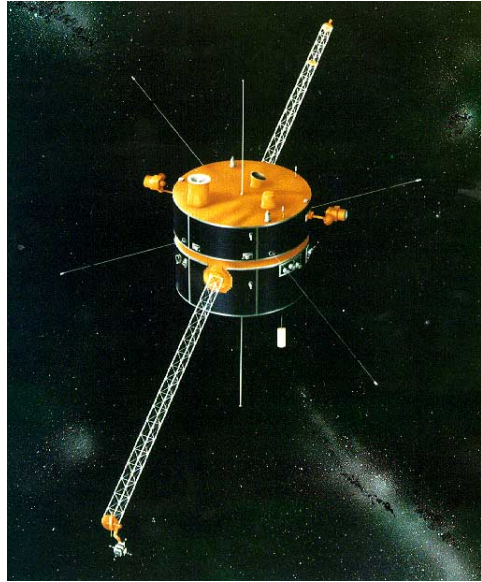


Figure 6: Konus-WIND <sup>3</sup>

Konus is a gamma-ray spectrometer installed on the WIND satellite to study solar wind. It has been in operation since 1994 Aptekar et al. (1995). Konus-WIND (KW) is an essential instrument for the study of gamma-ray bursts (GRBs) due to its unique properties. Its location offers advantages over low-Earth orbit GRB monitors, such as continuous coverage without Earth occultation, a stable background spectrum, and the ability to avoid trapped particles in Earth's radiation belt. Located up to 5.5 light seconds away from Earth, KW has detected and analyzed numerous GRBs, cataloged in Tsvetkova et al. (2017); Svinkin et al. (2016).

The KW detector features two identical omnidirectional NaI(Tl) detectors mounted on opposite faces of a rotationally stabilized spacecraft. Detector S1 points toward the south ecliptic pole, observing the south ecliptic hemisphere, while detector S2 observes the north ecliptic hemisphere. The detectors have an effective area of approximately 80-160 cm<sup>2</sup>, depending on the incident angle and photon energy.

KW detectors operate in two modes: waiting and triggered. In waiting mode, count rates are recorded in three energy windows (G1: 13-50 keV, G2: 50-200 keV, and G3: 200-760 keV) with a time resolution of 2.944 s. If the count rate in window G2 exceeds roughly a 9-sigma threshold above the background within the time frame  $\Delta T_{trig}$  (1 s or 140 ms), the instrument switches to triggered mode. In triggered mode, count rates in the three energy windows are recorded with varying time resolutions, ranging from 2 ms up to 256 ms. These time histories, which include 0.512 s of pre-trigger history, have a total duration of  $\sim$ 230 seconds.

Spectral measurements are carried out in two overlapping energy intervals, PHA1 (13-760 keV) and PHA2 (160 keV-10 MeV), beginning at the trigger time T0. Within each interval, 64 spectra are recorded across a 63-channel, pseudo-logarithmic energy scale. The initial four spectra are measured with a fixed accumulation time of 64 ms, primarily for studying short bursts. An adaptive system then establishes the accumulation times for the subsequent 52 spectra, which may range from 0.256 to 8.192 s based on the current count rate in the G2 window. The final eight spectra are obtained for 8.192 s each. As a result, the minimum duration of spectral measurements is 79.104 s, while the maximum duration is 491.776 s, approximately 260 s longer than the time history duration. Once the triggered-mode measurements are finished, KW enters a data-readout mode for about an hour, during which no measurements are available.

KW uses a standard KW dead time correction procedure for both light curves, with a dead time of a few microseconds, and spectra, with a dead time of around 42 microseconds, as described in Tsvetkova et al. (2017). Dead time refers to the period when a detector is unable to register new events due to the time constraints of its electronic components. The detector response matrix (DRM), which depends solely on

---

<sup>3</sup>Retrieved from: [https://en.wikipedia.org/wiki/Wind\\_\(spacecraft\)#/media/File:Wind\\_probe.jpg](https://en.wikipedia.org/wiki/Wind_(spacecraft)#/media/File:Wind_probe.jpg)

the burst angle relative to the instrument axis, is calculated using the GEANT4 package (Agostinelli et al., 2003). The instrument response calculation is discussed in greater detail in Terekhov et al. (1998).

KW has an extensive history of GRB detections, and cross-calibration with Swift-BAT and Suzaku-WAM has been performed, as explained in Sakamoto et al. (2011). Additionally, joint spectral fits were conducted with Fermi-GBM, as described in Lipunov et al. (2016). These joint spectral analyses demonstrate that KW’s capabilities are consistent with those obtained from other GRB monitors, with a spectrum normalization difference of less than 20% in joint fits.

### 3.4 Fermi Instrument

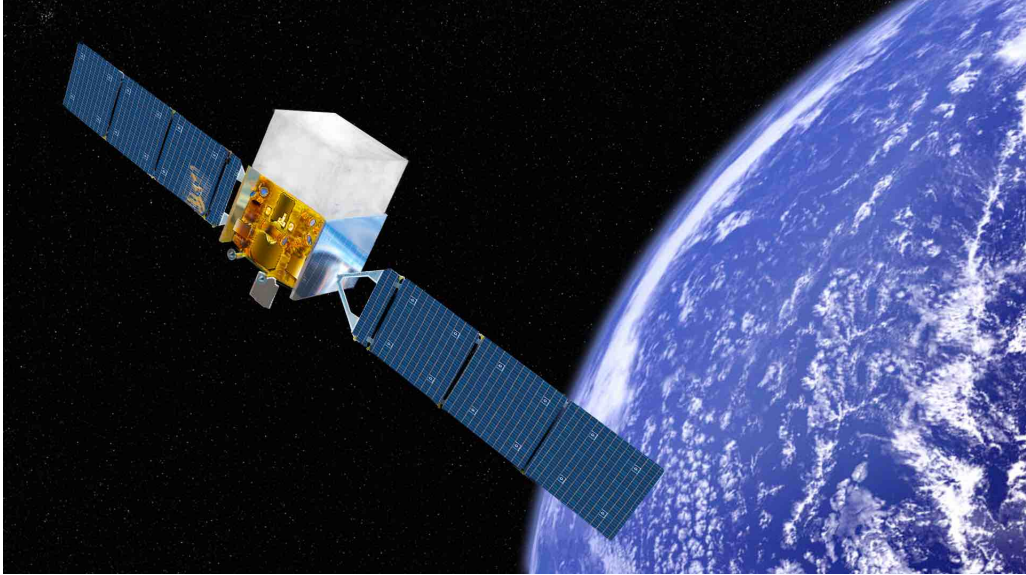


*Figure 7: Illustration of Fermi spacecraft above Earth* <sup>4</sup>

The Fermi Gamma-Ray Space Telescope was launched on 2008 June 11, into a 565 km orbit with an inclination of 25.6°. The payload comprises two science instruments, the Large Area Telescope (LAT) and the Gamma-Ray Burst Monitor (GBM). See Atwood et al. (2009) and Meegan et al. (2009) for a description of LAT and GBM, respectively. The LAT observes gamma-rays above  $\sim$ 20 MeV from a wide variety of astronomical sources. The primary instrument we will use in our joint spectral analysis is the GBM. The role of the GBM is the study of GRBs by making observations at energies from  $\sim$ 8 keV to  $\sim$ 40 MeV.

The GBM observes the whole sky that is not occulted by the Earth ( $\sim$ 1/3rd of the entire sky). It consists of twelve NaI(Tl) detectors and two Bismuth Germanate (BGO) scintillation detectors. The NaI crystals have a thickness of 1.27 cm and a diameter of 12.7 cm, covering an energy range of 8 keV–1 MeV. They are arranged around the spacecraft, with three at each of the four corners, so that the position of the GRB can be determined by comparing the count rates in the individual detectors. The two BGO crystals have a diameter and thickness of 12.7 cm and cover an energy range of 200 keV–40 MeV. They are located on opposite sides of the spacecraft so that at least one is always illuminated from any direction. A detailed detector response model has been developed based on Geant4 simulations. More information about the GBM detectors, their calibration, and the GRB catalog can be found in Meegan et al. (2009), Bissaldi et al. (2009), Goldstein et al. (2012), and Hoover et al. (2008).

The geometrical area of each detector is  $\sim$ 127cm<sup>2</sup>, while the effective area of the NaI and BGO detectors depend on the photon energy and angle of incidence. A more detailed description and the plots depicting the effective area can be found in Meegan et al. (2009) and Bissaldi et al. (2009), but we will summarize it here. For a normal incident angle the effective area of the NaI detectors varies from  $\sim$ 10cm<sup>2</sup> to  $\sim$ 110cm<sup>2</sup>, while in the BGOs the effective area varies from  $\sim$ 100cm<sup>2</sup> to  $\sim$ 200cm<sup>2</sup>.

At high photon rates, the performance of scintillation detectors can be impaired by two effects: dead time and pulse pile-up. Dead time limits the maximum rate of digitized pulses, with a nominal dead

---

<sup>4</sup>Retrieved from: <https://www.nasa.gov/sites/default/files/thumbnails/image/fermi.jpg>

time setting for GBM that results in a fixed dead time of  $2.6 \mu\text{s}$  per event, independent of energy, except for events in the overflow channel, which are assigned  $10 \mu\text{s}$  dead time.

The Fermi GBM has been shown to be accurate and consistent in detecting and analyzing GRBs in numerous studies. For instance, joint spectral fits were carried out with Fermi-GBM and KW, which demonstrated that the capabilities of Fermi-GBM are consistent with those obtained from other GRB monitors Lipunov et al. (2016). A large number of GRBs have been detected and cataloged in Gruber et al. (2014).

In conclusion, Fermi-GBM has been shown to be an accurate and consistent monitor for detecting and analyzing GRBs. Its accuracy has been verified through cross-calibration efforts and joint spectral fits, and it has been used extensively in a wide range of GRB studies with consistent and reliable results.

### 3.5 Datasets

The Interplanetary Network (IPN)<sup>5</sup> is a collaborative effort between various GRB mission science teams, with the aim of detecting and locating GRBs by triangulation on cross-correlation of light curves. By using a network of spacecraft, the IPN is able to triangulate the location of a GRB and provide accurate coordinates for follow-up observations. The astronomical locations of GRBs are determined by comparing the arrival times of the event at the locations of the detectors. Note that very few GRB missions have good localization performance, because it's very challenging to do imaging in gamma-rays.

We queried from the IPN database a list of confirmed GRBs in our search window, along with coordinate information in the  $\text{RA}_{J2000}$  and  $\text{Dec}_{J2000}$  format. These coordinates are used in astronomy to locate celestial objects on the celestial sphere, with RA being measured in degrees eastward from the Vernal Equinox point, and Dec being measured in degrees north or south of the celestial equator. The J2000 designation indicates that the coordinates are referenced to the position of celestial objects relative to the date and time 12:00 on January 1, 2000.

The GRBweb<sup>6</sup> database is a near real-time resource for detected GRBs, providing researchers with up-to-date information on these cosmic events. Events from this catalog were added to our dataset of confirmed triggers up until the end of 2021.

To retrieve information on the subset of GRBs detected by ASIM, we also utilized the Gamma-ray Coordinate Network (GCN) archive<sup>7</sup>, which is a collaborative effort among various space mission science teams. Hosted on a NASA server, this online database provides access to real-time alerts and notifications of new GRBs, as well as a searchable database of past events. With a wealth of information, including observational data, spectral analyses, and source identifications, the GCN archive serves as a valuable resource for the study of GRBs.

ASIM data is fetched from a local database. Software developed by my colleagues at the Birkeland Center for Space Science were used to extract and process the raw data. Note that software had to be developed from scratch to further process the data. Please see Appendix B for more information.

Data from KW was provided to us by our research colleagues operating the instrument. The light curves (LCs) and the data as FITS files (see Appendix B and section 4.3.5 for a more detailed description of FITS files) were provided. Note that the spectrums from the KW instrument are accumulated over a fixed time interval and this dictates when we accumulate the spectrum from ASIM and Fermi.

For Fermi we fetched the relevant GRB data from the Fermi/GBM burst database<sup>8</sup>. Fermi/GBM software, Goldstein et al. (2022)<sup>9</sup> is used in a Python environment to handle the raw data, extract the spectrum for the burst and background and produce the FITS files.

---

<sup>5</sup>IPN:<https://heasarc.gsfc.nasa.gov/w3browse/all/ipngrb.html>

<sup>6</sup>GRBweb: [https://user-web.icecube.wisc.edu/~grbweb\\_public/Summary\\_table.html](https://user-web.icecube.wisc.edu/~grbweb_public/Summary_table.html)

<sup>7</sup>GCN: [https://gcn.gsfc.nasa.gov/gcn3\\_archive\\_GRB.html](https://gcn.gsfc.nasa.gov/gcn3_archive_GRB.html)

<sup>8</sup>Fermi/GBM database: <https://heasarc.gsfc.nasa.gov/FTP/fermi/data/gbm/bursts/>

<sup>9</sup>Fermi/GBM software: [https://fermi.gsfc.nasa.gov/ssc/data/analysis/gbm/gbm\\_data\\_tools/gdt-docs/index.html](https://fermi.gsfc.nasa.gov/ssc/data/analysis/gbm/gbm_data_tools/gdt-docs/index.html)

## 4 Methods

The complete workflow of the methodology involves identifying GRBs, preparing ASIM and Fermi data for spectral analysis, cross-correlating light curves, performing spectral fitting, and ensuring data consistency. Initially, a GRB identification is determined between the ASIM trigger list and GRBs identified by the InterPlanetary Network (IPN) or the GRBweb collaboration. ASIM and Fermi data are then prepared and cross-correlated to align the light curves in the correct reference frame of KW. Fermi/GBM data preparation is carried out using GBM software and custom functions to handle raw data, extract relevant light curves and spectra, and shift the data by a time lag. The same is true for ASIM, that custom developed software was applied to handle the raw data. Spectral fitting is conducted using a forward folding method with the chosen model, and the goodness-of-fit, cross-calibration coefficients and confidence intervals are calculated. A data consistency check is performed to ensure accuracy in the ASIM data analysis pipeline. This comprehensive methodology forms the basis for conducting a joint spectral analysis of GRBs.

### 4.1 GRB Identification in ASIM

The goal was to determine a correlation between the ASIM trigger list and gamma-ray bursts (GRBs) identified by the InterPlanetary Network (IPN) or the IceCube collaboration. Between June 1st, 2018, and December 31st, 2021, the ASIM trigger list contained around 270,000 triggers for both HED and LED. Most of these triggers were related to other atmospheric phenomena or cosmic rays

CSV files containing the trigger times ( $T_0$ ) of KW, Fermi, and other spacecrafts were obtained by me from the databases mentioned earlier, in order to identify a correspondence. A correspondence between ASIM and the other triggered instruments was sought, within a  $\pm 10$ -second time window, taking into account the photon propagation time between the instruments. The preliminary search yielded 31 matches, which necessitated further examination to confirm their classification as GRBs. In order to eliminate random coincidences and insignificant signals, the ASIM light curve was extracted by me and cross-referenced with other instruments. Eventually, 12 confirmed GRBs suitable for spectral analysis were pinpointed.

### 4.2 ASIM Data Preparation

Several important metrics were extracted from the ASIM database by me to prepare the ASIM data for spectral analysis. It is noteworthy that all 12 GRB candidates were triggers in the high-energy detector (HED). A MATLAB code developed by researchers at UiB was used to extract the ASIM data for our GRB candidates, and the extracted data was then imported into a Python environment for data analysis. The relevant data included the time of arrival of individual photons with microsecond resolution relative to  $T_0$ , as well as corresponding BGO address, detector assembly unit address, detector address, energy channel, and type. The handling of this large amount of ASIM data required the use of important libraries such as Pandas and NumPy to create a DataFrame or matrix.

To ensure accurate energy measurements, the energy channel was calibrated to keV using time-dependent calibration coefficients for each BGO with a quadratic fit. The calibration equation used was Energy [keV] =  $A \times \text{CHANNEL}^2 + B \times \text{CHANNEL} + C$ , where  $A$ ,  $B$ , and  $C$  were the calibration coefficients determined using the 511 keV line and 1274.5 keV line from the on-board Na-22 calibration source. It should be noted that a portion of the 511 keV line is also due to secondaries from cosmic protons, and the proton peak at about 31 MeV in the background energy spectrum was also used. A specific set of calibration coefficients had to be retrieved and applied for each burst.

The application of the safety-time criteria (ST) and the cross-correlation procedure, aimed to ensure accurate processing of ASIM data while accounting for any uncertainties in timing. It is worth noting that only a fraction of a percent of data were removed as a result of these procedures.

#### 4.2.1 Cross Correlation of Light Curves

The mathematical technique of cross-correlation, which allows the measurement of similarity between two signals as a function of time lag, was used in the preparation of data for joint spectral analysis. In order to accurately align the light curves (LCs) from different instruments in the correct reference frame, cross-correlation was performed as a necessary step. This was especially important due to the different trigger logics and reference times ( $T_0$ ) of each instrument.

To align the LCs in the correct reference frame, the FERMI and ASIM data were initially shifted based on the instrument's T0 and time of flight (ToF) to center the relevant LCs at approximately the same T0, facilitating the cross-correlation between the LC objects. The LCs from KW, which have varying bin sizes in powers of 2, were cut at the appropriate time interval and aligned with the FERMI and ASIM data by aligning the data with KW's fixed accumulation times for the spectral files.

For the cross-correlation procedure, the software package `stingray` was utilized in a Python environment to create a LC object for each instrument. The LC objects' bin edges had to be identical, and a cross-correlation object was created with the LC objects passed in as parameters. From the cross-correlation object, the time lags that would produce the highest correlation between the LC objects were estimated.

An example of a cross-correlation plot was displayed in Figure 8, which showed the correlation factor as a function of time lags between the KW and ASIM/HED LCs. The ASIM data were shifted by the estimated time lag, bringing the data into the reference frame of KW.

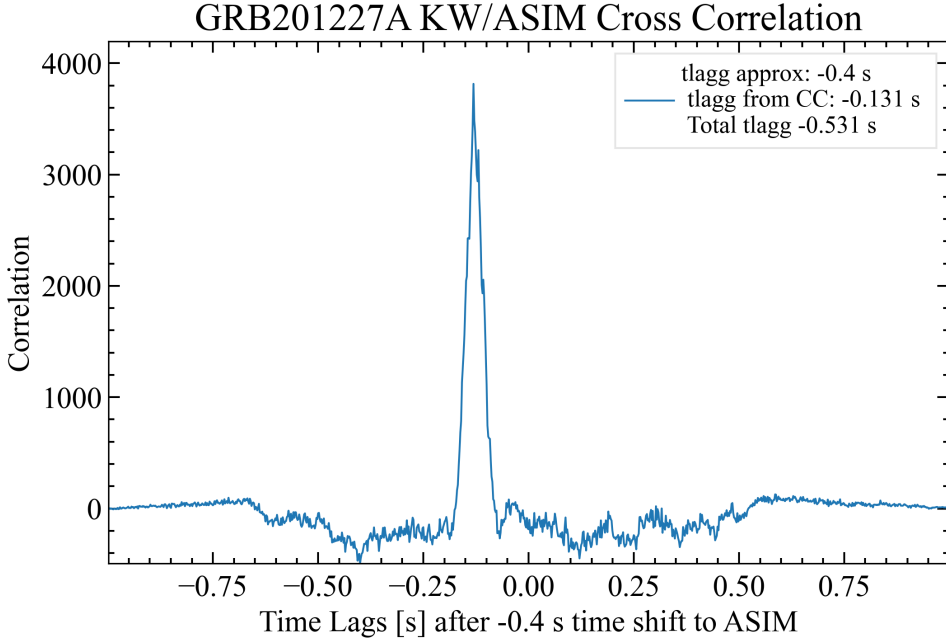


*Figure 8: Cross-correlation plot for GRB 201227A between ASIM/HED and KW, showing maximum correlation with a time lag of -531 ms, which is applied to HED LC. y-axis shows the correlation and the x-axis shows the time lags. A time lag of -0.4 s was applied before the cross-correlation with KW. Cross-correlation function outputs max correlation for -131 ms, resulting in a total time lag of -531 ms*

### 4.3 Basics of Spectral Fitting

#### 4.3.1 Xspec

`Xspec` is a spectral fitting software used to analyze X-ray and  $\gamma$ -ray data. It provides a suite of models to fit the spectra and can compute various parameters and goodness-of-fit statistics. `Xspec` provides models such as the cutoff power law and the Band function. I utilize locally modified versions of these models, as developed by Takanori Sakamoto (see section 4.3.4). Please refer to the `Xspec` Manual<sup>10</sup> for a detailed description of the software.

#### 4.3.2 Spectra

A spectrometer measures photon counts  $C$  in specific instrument channels  $I$ , not the actual spectrum of a source. The observed spectrum  $C(I)$  consists of two files: the data (spectrum) file, containing  $D(I)$ , and the background file, containing  $B(I)$ . The data file tells Xspec how many total photon counts were detected by the instrument in a given channel. Xspec then uses the background file to derive the set

<sup>10</sup>Xspec Manual: <https://heasarc.gsfc.nasa.gov/xanadu/Xspec/XspecManual.pdf>

of background-subtracted spectra  $C(I)$  in units of counts per second. The background-subtracted count rate is given by, for each spectrum:

$$C(I) = \frac{D(I)}{a_{D(I)} t_D} - \frac{b_{D(I)}}{b_{B(I)} a_{B(I)} t_B} \frac{B(I)}{a_{B(I)} t_B} \quad (1)$$

where  $D(I)$  includes all counts from the event of interest (the GRB in our case), but there are also background counts.  $B(I)$  includes only the background and is usually accumulated before the event of interest, but as close in time as possible.  $t_D$  and  $t_B$  are the exposure times in the data and background files;  $b_{D(I)}$  and  $b_{B(I)}$ ,  $a_{D(I)}$  and  $a_{B(I)}$  are the background and area scaling values from the spectrum and background respectively, which together refer the background flux to the same area as the observation as necessary. Note that  $a_{D(I)}$ ,  $b_{B(I)}$  and  $a_{B(I)}$  is 1 for ASIM. When this is done, Xspec has an observed spectrum to which the model spectrum can be fit.

The observed spectrum is linked to the source model spectrum  $f(E)$  through,

$$C(I) = \int f(E) R(I, E) dE \quad (2)$$

where  $R(I, E)$  represents instrumental response (DRM), which is proportional to the probability of detecting an incoming photon with energy  $E$  in channel  $I$ . Inverting this equation to obtain  $f(E)$  is not feasible, so I therefore apply a "forward folding method", where I choose a appropriate  $f(E)$  and I try to modify the parameters such that it will fit the observed spectrum. See details in Section 4.3.5.

An alternative type of spectrum that may provide informative insights is the unfolded spectrum, which is typically expressed as  $\nu F_\nu$  or  $E^2 N(E)$  and measured in units of  $\text{keV}^2(\text{photons} \cdot \text{cm}^{-2}\text{s}^{-1}\text{keV})$ . To plot this spectrum in Xspec, the data must be fitted, and then call the command `p1 eeufspec delchi` to plot the  $\nu F_\nu$  spectrum along with the residuals. This spectrum is of theoretical significance and can provide valuable insights into the properties of the source by exhibiting the spectral energy distribution. Figure 11 demonstrates an example  $\nu F_\nu$  or unfolded spectrum from two sources. One significant observation that can be made from these, is the presence of  $E_{peak}$ , which is a measure of the energy where most of the power per energy bin is emitted.

### 4.3.3 Response Files

The response of an instrument is proportional to the probability that an incoming photon of energy  $E$  will be detected in a given channel  $I$ . This probability is described by a continuous function of  $E$ , which is then converted into a discrete function using a response matrix. The response matrix defines the energy ranges  $E_j$  and the response  $R_D(I; J)$  for each channel. The response function is given by the equation:

$$R_D(I, J) = \frac{\int_{E_{j-1}}^{E_j} R(I, E) dE}{E_j - E_{j-1}} \quad (3)$$

Here,  $R_D(I, J)$  is the response for channel  $I$  and energy range  $J$ , and  $R(I, E)$  is the instrumental response function for energy  $E$  and channel  $I$ .

The auxiliary response file contains an array  $A_D(J)$  that is multiplied into  $R_D(I; J)$ . This array represents the efficiency of the detector, with the response file representing a normalized Redistribution Matrix Function (RMF). The response is conventionally measured in units of  $\text{cm}^2$ . The auxiliary response file is particularly useful for correcting for the effects of dead time and pile-up, which can significantly impact the accuracy of the measured spectrum. By including information about the detector's efficiency and the RMF, `Xspec` is able to accurately model the measured spectrum. The RMF and AUX files accompany the provided spectral files from KW, while the ASIM and FERMI embed the auxiliary response into their DRMs.

To model the response of the ASIM/MXGS instrument to incoming radiation and particles, a mass model of the instrument and relevant elements, including MXGS and Columbus, was created using the Geant4 toolkit (Agostinelli et al., 2003). More details about this simulation can be found in Østgaard et al. (2019) and Sarria et al. (2019). To generate the DRM for ASIM, mono-energetic photon beams

were directed at the modeled detectors for all polar and azimuthal angles, with a resolution of  $15^\circ$ . For HED, logarithmically spaced energies from 100 keV to 100 MeV were used. Figure 9 shows the effective area of the CZT and BGO detectors as a heatmap. The simulated incident angle in polar coordinates was set to  $\vartheta, \varphi = 0^\circ, 0^\circ$ .

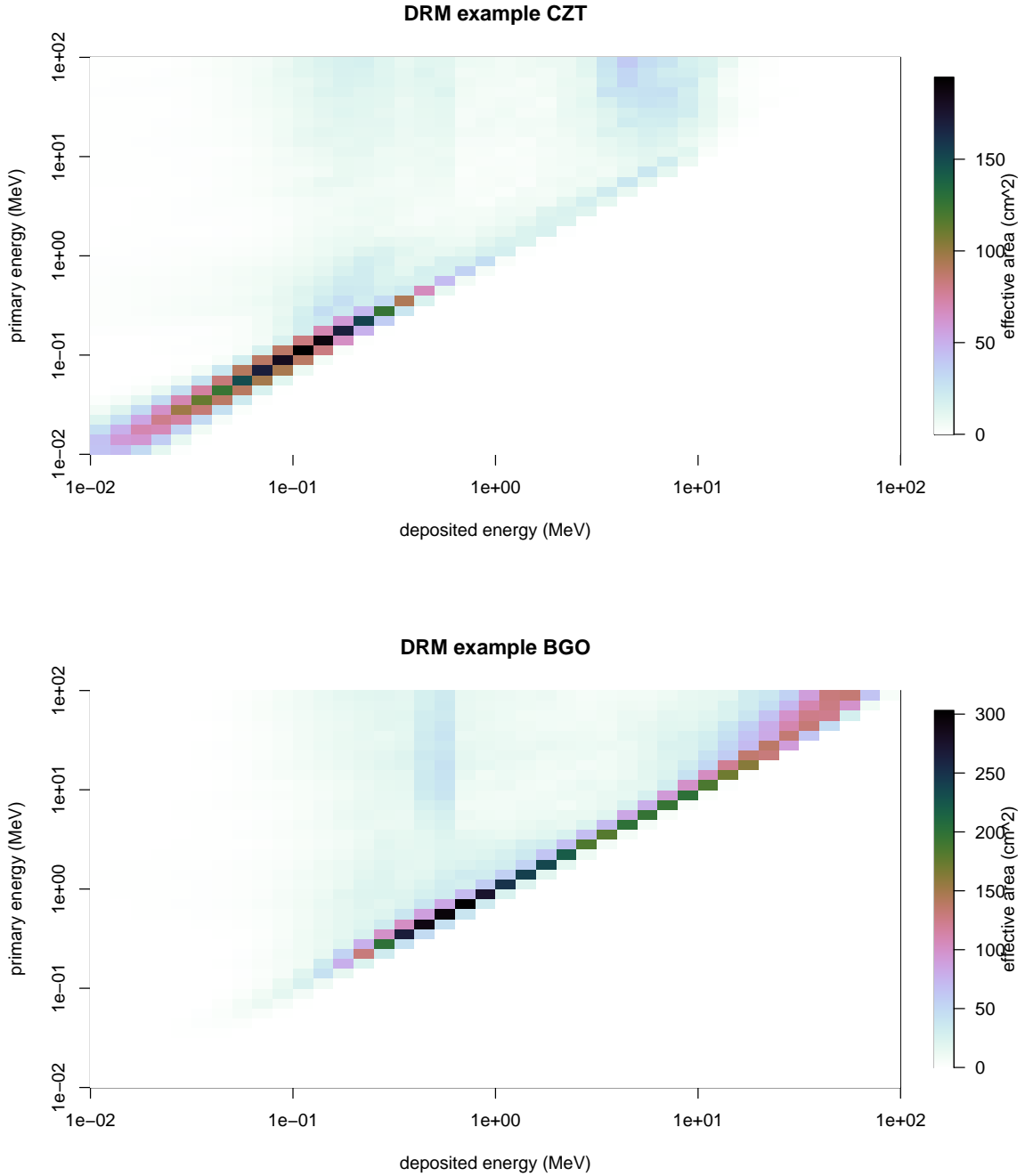


*Figure 9: Example heatmap of the effective area in the CZT and BGO detector*

#### 4.3.4 Models

In this section, I describe the models used for spectral fitting in our analysis. The joint spectral fits are performed by `Xspec` (ver. 12.13.0c). I use two local models for our fits, a cutoff power-law (CPL) model and the Band function, both parameterized with  $E_{peak}$ .

The CPL model is described by the equation:

$$f(E) = K_{100}^{\text{CPL}} \left( \frac{E}{100 \text{ keV}} \right)^{\alpha^{\text{CPL}}} \exp \left[ \frac{-E(2 + \alpha^{\text{CPL}})}{E_{peak}} \right] , \quad (4)$$

where  $\alpha^{\text{CPL}}$  is the power-law photon index,  $K_{100}^{\text{CPL}}$  is the normalization at 100 keV in units of photons  $\text{cm}^{-2} \text{ keV}^{-1}$ , and  $E_{peak}$  is the peak energy in the  $\nu F_\nu$  spectrum.

The Band function Band et al. (1993) is a phenomenological model used to describe the spectra of a large set of GRBs over a broad energy range, typically spanning from keV to MeV. The model consists of two power-law components that are smoothly connected at a break energy, which is often interpreted as the peak energy of the  $\nu F_\nu$  spectrum. The Band function is given by:

$$f(E) = \begin{cases} K_1 \left( \frac{E}{100 \text{ keV}} \right)^\alpha \exp \left[ -\frac{E(2+\alpha)}{E_{peak}} \right], & E < \left[ \frac{(\alpha-\beta)E_{peak}}{(2+\alpha)} \right] \\ K_1 \left[ \frac{(\alpha-\beta)E_{peak}}{(2+\alpha)100 \text{ keV}} \right]^{\alpha-\beta} \left( \frac{E}{100 \text{ keV}} \right)^\beta, & E \geq \left[ \frac{(\alpha-\beta)E_{peak}}{(2+\alpha)} \right] \end{cases} \quad (5)$$

where  $\alpha$  is the lower energy photon index,  $\beta$  is the high-energy photon index,  $E_{peak}$  is the peak energy in the  $\nu F_\nu$  spectrum, and  $K_1$  is the normalization at 100 keV in units of photons  $\text{cm}^{-2} \text{ s}^{-1} \text{ keV}^{-1}$ . The two spectral regimes are separated by the break energy  $E_0$ . The peak energy ( $E_{peak}$ ) in the  $\nu F_\nu$  spectrum is related to the break energy ( $E_0$ ) through:

$$E_{peak} = (2 + \alpha)E_0 \quad (6)$$

A constant normalization factor, also known as the cross-calibration coefficient, was introduced by me to account for systematic uncertainties in the instrument's DRM. This factor was multiplied into the spectral model to adjust for differences in the effective area of the instruments across different energy ranges. The constant factor was an important parameter, as it allowed for the evaluation of the consistency of HED measurements with those obtained from other spacecrafts after accounting for the instrument's response. By analyzing this parameter, valuable insights into the performance and accuracy of the HED instrument can be gained, and the consistency and reliability of our results can be ensured.

In the joint spectral fits of KW+HED+GBM, KW+HED, and HED+GBM, I fixed the normalization factor for the relevant data group (either KW or GBM) at unity, while the constant factors of the other data groups were set as free parameters. Following the fitting procedure, the "best-fit" model was determined, and it was expected that the constant factor(s) in the joint spectral fit would approximate unity. This would indicate that the respective DRMs and cross-calibration procedures had been effectively calibrated to the instruments and that the various spectral files had been properly implemented. Any large deviations from unity were thoroughly investigated.

#### 4.3.5 Fitting Procedure

To initiate the fitting procedure, I load the appropriate fits files, including the burst spectrum (with a .pha extension), background spectrum (.bak), and instrument response (.rsp/.rmf/.arf). Data from various instruments must then be assigned into data groups for a joint spectral fit. Typically, "bad" or unsuitable energy channels are ignored. If I am performing a joint spectral fit, I choose the optimal model and multiply it with a constant. I then fix the relevant data group to unity (as discussed section 4.3.4). When calling the `fit` command, the model  $f(E)$  is fit to the observed data  $C(I)$ , yielding our parameter values.

Data fitting typically involves a forward folding method where an appropriate model spectrum,  $f(E)$ , is selected and multiplied by the instrument's DRM to generate a predicted count spectrum ( $C_p(I)$ ). The resulting fit statistic assesses whether the chosen model matches the observed data. By adjusting parameters in  $f(E)$  until optimal values are obtained that produce an ideal fit statistic, one can identify

best-fit parameters. These optimized parameter values yield the most suitable fitted model represented as  $f_b(E)$ . The most common fit statistic in use for determining the “best-fit” model is the  $\chi^2$ .

Upon obtaining the ”best-fit” model in `Xspec`, the confidence intervals of the associated parameters can be determined using the ”error” command. This command calculates parameter errors by varying a parameter until the fit statistic exceeds the best-fit value by a predetermined amount. The standard confidence intervals are typically calculated based on a  $2.706\sigma$  or 90% confidence level.

To summarize, `Xspec` combines observed spectra, instrument response functions, and various models to approximate the source spectra. The goodness-of-fit and confidence interval calculations provide a measure of the accuracy and reliability of our results. `Xspec` provides a powerful tool for fitting the spectra for X-rays and  $\gamma$ -rays.

#### 4.4 ASIM Data Analysis Consistency Check

Due to a significant deviation in the cross-calibration coefficient for ASIM/HED ( $C_A$ ), as shown in Table 5, a data consistency check was performed for ASIM. It was expected that the calibration coefficient would deviate no more than 25% from unity, but events such as GRB190305A and 211211A had a constant factor of 0.349 and 0.359, respectively. The possibility of discrepancies in the data preparation pipeline could not be ruled out. Therefore, to ensure accuracy in the ASIM data analysis pipeline, a thorough investigation was conducted of every step that could potentially introduce errors. The steps examined are listed below:

- Light curve analysis: section 5.3.1
- Background analysis: section 5.3.2
- ASIM DRM analysis: section 5.3.3
- Energy calibration coefficients analysis: section 5.3.4
- Consistency of the Mass Model analysis: section 5.3.5
- ASIM Fits analysis: section 5.3.6

#### 4.5 Fermi/GBM Data Preparation

The burst data for the relevant triggers was fetched, as described in Section 3.5. Coordinate information was obtained from the IPN in the form of  $RA_{J2000}$  and  $Dec_{J2000}$ , which was used to calculate the angle of incidence for all detectors on board FERMI/GBM. In our spectral analysis, detectors with the lowest angle of incidence and the most illumination were typically selected. It should be noted that incident angles above  $60^\circ$ - $70^\circ$ should be approached with caution, as they may introduce errors in the analysis. The FERMI-GBM software<sup>11</sup> was used to handle the raw data and extract the relevant light curves and spectra. However, it is important to note that the GBM software does not have an in-built function to shift the data by a time lag, so a custom function was developed within the GBM-module specifically for this analysis.

---

<sup>11</sup>Fermi/GBM software: [https://fermi.gsfc.nasa.gov/ssc/data/analysis/gbm/gbm\\_data\\_tools/gdt-docs/index.html](https://fermi.gsfc.nasa.gov/ssc/data/analysis/gbm/gbm_data_tools/gdt-docs/index.html)

## 5 Results & Discussions

### 5.1 ASIM GRB database

From June 1st, 2018 to December 31st, 2021, ASIM detected 12 confirmed GRBs. A summary of these detections can be found in the table below. Table 2 displays the index, GRB identification, classification type (Short/Long - S/L), ASIM trigger time ( $T_0$ ), and corresponding coordinate information ( $RA_{J2000}$ ,  $Dec_{J2000}$ ). The magnetic latitude ( $mlat$ ) depends on the ISS position along its orbit and is directly related to the instrument background (refer to section 5.3.2). Finally, the table shows the angle of incidence on board the ISS ( $\vartheta$  and  $\varphi$ ). See Figure 17a for the corresponding reference frame

Figure 10 illustrates the stacked light curve of a short burst, specifically GRB 201227A. The HED and Fermi GBM light curves have been shifted into the reference frame of KW through cross-correlation. The counts for each instrument have been binned by 2 ms. The vertical dotted line represents the interval during which we accumulate spectra for spectral analysis. For this particular burst, the interval spans from  $T_0$  to  $T_0+0.064s$ . The full GRB catalog can be found in Appendix A.

In Table 2, each row corresponds to a GRB detected concurrently by either KW and/or Fermi. It is crucial to emphasize that most detected GRBs in our sample are of the short type. The overrepresentation of short GRBs is mainly due to the MXGS instrument’s triggering logic, which favors short events with time scales 20 ms or less.

Table 3 presents the data availability for each identified GRB, specifically from the LED, HED, KW, and Fermi/GBM instruments. A “✓” denotes available data, while an “✗” indicates unavailable data. Notably, for most GRBs, data can be obtained from either KW or Fermi instruments.

It is important to note that we have not used LED data in our joint spectral analyses; instead, we only used HED data. This decision was made because either a clear signal was not detectable in the LED data or LED data was not collected for the burst, as it is only gathered during local night-time.

We did not perform a joint spectral analysis for GRB 180720B, 200415A, and 210424B. GRB 180720B was excluded due to the difficulty in extracting a proper background in HED. GRB 200415A is a unique burst that originates from a distant giant magnetar flare (a highly magnetized neutron star) and is thoroughly described in Castro-Tirado et al. (2021). The burst was so bright that saturated both Fermi and KW, affecting the flux estimates. Therefore, it is not an event suitable for cross-calibration purposes.

We relied on Konus-Wind to determine the time intervals used for accumulating spectra for ASIM/HED and Fermi/GBM. While I were unable to modify or decide on the time interval used for KW spectra, I had control over those of HED and GBM. The KW spectra were provided to us by the KW-team, with specified start and stop times, which are shown Table 4 along with the propagation time between different instruments. It is important to note that we have excluded three GRBs from this table, as discussed previously.

For two cases (GRB 181222B, 210619B), we observe multiple separate time intervals within the same burst. We treated these intervals as individual spectra. Although our analysis includes a smaller number of unique GRBs, it covers a total of 4 spectra, allowing us to examine the specific characteristics of each burst. A more in-depth analysis of GRB 210619B and another peculiar burst (GRB 211211A) can be found in section 5.4. It is worth noting that all light curves for all instruments, along with joint spectra, are included in Appendix A.

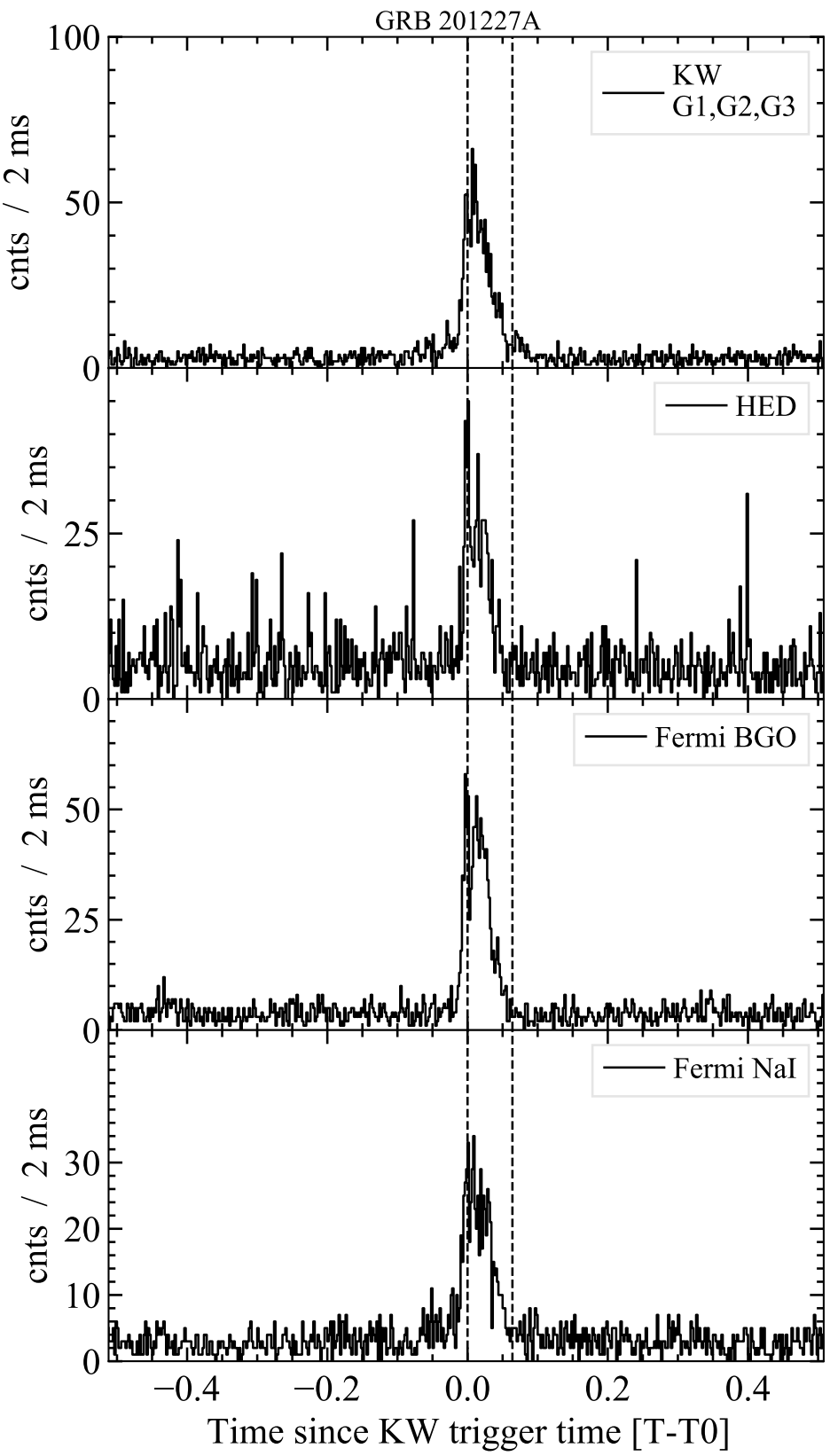


Figure 10: Stacked light curve of GRB 201227A

| I  | GRB     | Type | T0 [UT]                 | RA <sub>J2000</sub><br>[°] | Dec <sub>J2000</sub><br>[°] | mlat [°] | θ [°]   | φ [°]    |
|----|---------|------|-------------------------|----------------------------|-----------------------------|----------|---------|----------|
| 1  | 180720B | L    | 2018-12-22 20:11:36.136 | 0.528                      | -2.917                      | 38.5434  | 141.258 | -42.464  |
| 2  | 181222B | S    | 2018-12-22 20:11:36.136 | 312.572                    | 24.24                       | 55.2793  | 100.622 | -49.011  |
| 3  | 190206A | S    | 2019-02-06 03:49:28.229 | 313.33                     | -30.51                      | -54.2321 | 110.882 | -36.976  |
| 4  | 190305A | S    | 2019-03-05 13:05:20.615 | 11.627                     | 50.349                      | 29.9766  | 133.903 | -2.076   |
| 5  | 190606A | S    | 2019-06-06 01:55:06.781 | 76.561                     | -0.638                      | -47.4887 | 120.114 | -20.997  |
| 6  | 200415A | S    | 2020-04-15 08:48:05.557 | 11.885                     | -25.263                     | -45.2905 | 70.643  | -81.754  |
| 7  | 200521A | S    | 2020-05-21 12:16:39.004 | 169.531                    | 7.222                       | -15.8446 | 130.710 | -45.648  |
| 8  | 200716C | S    | 2020-07-16 22:57:39.947 | 196.01                     | 29.644                      | 39.4085  | 143.834 | -140.018 |
| 9  | 201227A | S    | 2020-12-27 15:14:06.322 | 170.121                    | -73.613                     | 14.4085  | 77.318  | -50.463  |
| 10 | 210424B | S    | 2021-04-24 08:01:55.095 | 284.716                    | 16.172                      | -32.3326 | 96.097  | -17.705  |
| 11 | 210619B | L    | 2021-06-19 23:59:24.910 | 319.716                    | 33.850                      | 41.2906  | 135.591 | -138.783 |
| 12 | 211211A | L    | 2021-12-11 13:10:03.099 | 212.271                    | 27.884                      | 46.4225  | 112.781 | -177.757 |

Table 2: Table showing the index, GRB identification, classification type, ASIM trigger time, and corresponding coordinate information of burst, magnetic latitude, and the angle of incidence on board ISS ( $\theta$ ,  $\varphi$ )

| GRB      | LED | HED | KW | FERMI |
|----------|-----|-----|----|-------|
| 180720B* | x   | ✓   | ✓  | ✓     |
| 181222B  | x   | ✓   | ✓  | ✓     |
| 190206A  | x   | ✓   | ✓  | x     |
| 190305A  | x   | ✓   | ✓  | x     |
| 190606A  | x   | ✓   | ✓  | ✓     |
| 200415A* | ✓   | ✓   | x  | x     |
| 200521A  | x   | ✓   | ✓  | x     |
| 200716C  | x   | ✓   | ✓  | ✓     |
| 201227A  | x   | ✓   | ✓  | ✓     |
| 210424B* | ✓   | ✓   | ✓  | x     |
| 210619B  | x   | ✓   | ✓  | ✓     |
| 211211A  | x   | ✓   | x  | ✓     |

Table 3: Data availability for LED, HED, KW, and FERMI. ✓ indicates that the data is available, x indicates that the data is not available. The GRBs that are marked with an asterisk symbol are not analyzed.

| GRB      | Interval | KW    |       | ToF      |           |
|----------|----------|-------|-------|----------|-----------|
|          |          | $t_i$ | $t_f$ | KW → ISS | ISS → GBM |
| 180720B  | —        | —     | —     | -4.2377  | -0.0051   |
| 181222B  | 1        | 0.0   | 0.512 | 2.8716   | 0.0026    |
|          | 2        | 0.128 | 0.256 | —        | —         |
| 190206A  | 1        | 0.0   | 0.064 | 4.9225   | 0.0189    |
| 190305A  | 1        | 0.768 | 1.280 | 3.4460   | —         |
| 190606A  | 1        | 0.0   | 0.064 | 4.0316   | -0.0081   |
| 200415A  | 1        | —     | —     | 4.1840   | -0.0246   |
| 200521A  | 1        | 0.0   | 0.256 | -0.6226  | —         |
| 200716C  | 1        | 0.0   | 0.256 | 3.0155   | 0.0109    |
| 201227A  | 1        | 0.0   | 0.064 | 0.7142   | -0.0008   |
| 210424B  | 1        | —     | —     | -0.5033  | 0.0254    |
| 210619B  | 1        | 0.512 | 0.768 | -2.6183  | 0.0227    |
|          | 2        | 0.0   | 2.048 | —        | —         |
| 211211A* | 1        | —     | —     | —        | 0.0049    |

Table 4: Spectral intervals used in the analysis and time of flight between instruments. All start and stop times are given relative to the KW T0 in seconds.

\* KW data not available. Spectrum  $t_i = 5.824\text{s}$  and  $t_f = 6.208\text{s}$  for HED and GBM

## 5.2 Joint Spectral Analysis

In the following sections, I will discuss the results of the joint spectral analysis and the model parameters obtained from fitting a subset of the GRBs.

In Table 5, I present the model parameters obtained from joint spectral fits utilizing the normalization constant factor and the Band function to validate the performance of ASIM/HED and Fermi/BGO against KW. The cross-calibration coefficient for HED ( $C_A$ ) is the primary focus of these fits. The table includes the GRB identification, the interval used for fitting, the resulting model parameters such as  $\alpha$ ,  $\beta$ ,  $E_{peak}$ , and the goodness of fit represented by  $\chi^2/\text{dof}$ . cross-calibration coefficients for HED and Fermi/GBM detectors are also listed. The error is computed in Xspec after the fit in a 90% confidence range ( $2.706\sigma$ ). For GRB 211211A where KW data is unavailable, I fix the cross-calibration constant for GBM at 1.

| GRB      | Int. | $\alpha$                   | $\beta$                    | $E_{peak}$ [keV]     | $\chi^2/\text{dof}$ | $C_A$                     | $C_F$                     |
|----------|------|----------------------------|----------------------------|----------------------|---------------------|---------------------------|---------------------------|
| 181222B  | 1    | $-0.538^{+0.025}_{-0.028}$ | $-3.077^{+0.094}_{-0.143}$ | $365^{+10}_{-9}$     | 265/204 (1.30)      | $0.850^{+0.055}_{-0.062}$ | $1.13^{+0.030}_{-0.032}$  |
|          | 2    | $-0.118^{+0.045}_{-0.043}$ | $-4.145^{+0.292}_{-0.359}$ | $430^{+11}_{-11}$    | 198/181 (1.06)      | $0.854^{+0.050}_{-0.047}$ | $1.12^{+0.045}_{-0.042}$  |
| 190206A  | 1    | $-0.344^{+0.088}_{-0.079}$ | $-3.30^{+0.264}_{-0.407}$  | $1104^{+124}_{-129}$ | 53/37 (1.43)        | $2.69^{+0.230}_{-0.217}$  | NA                        |
| 190305A  | 1    | $-0.179^{+0.073}_{-0.063}$ | $-3.015^{+0.126}_{-0.143}$ | $435^{+20}_{-22}$    | 89/68 (1.29)        | $0.349^{+0.027}_{-0.025}$ | NA                        |
| 190606A  | 1    | $-1.02^{+0.042}_{-0.044}$  | $-2.14^{+0.157}_{-0.253}$  | $1748^{+882}_{-589}$ | 138/104 (1.33)      | $1.18^{+0.163}_{-0.158}$  | $0.975^{+0.089}_{-0.078}$ |
| 200521A  | 1    | $-0.392^{+0.087}_{-0.083}$ | $-2.20^{+0.089}_{-0.079}$  | $1411^{+156}_{-268}$ | 47/45 (1.05)        | $1.37^{+0.109}_{-0.098}$  | NA                        |
| 200716C  | 1    | $-0.537^{+0.099}_{-0.089}$ | $-2.83^{+0.300}_{-0.729}$  | $702^{+107}_{-90}$   | 129/141 (0.91)      | $1.11^{+0.172}_{-0.144}$  | $0.985^{+0.079}_{-0.073}$ |
| 201227A* | 1    | $-0.199^{+0.083}_{-0.067}$ | $-3.57^{+0.508}_{-0.896}$  | $948^{+52}_{-68}$    | 72/68 (1.05)        | $1.22^{+0.125}_{-0.115}$  | $1.36^{+0.084}_{-0.078}$  |
| 210619B  | 1    | $-0.510^{+0.114}_{-0.116}$ | $-2.165^{+0.053}_{-0.055}$ | $581^{+63}_{-57}$    | 248/206 (1.12)      | $0.922^{+0.070}_{-0.057}$ | $1.18^{+0.048}_{-0.046}$  |
|          | 2    | $-0.733^{+0.047}_{-0.038}$ | $-2.217^{+0.028}_{-0.027}$ | $543^{+24}_{-28}$    | 325/222 (1.46)      | $0.848^{+0.033}_{-0.027}$ | $1.13^{+0.03}_{-0.03}$    |
| 211211A  | 1    | $-1.073^{+0.030}_{-0.024}$ | $-2.75^{+0.102}_{-0.189}$  | $1467^{+224}_{-82}$  | 246/148 (1.66)      | $0.359^{+0.014}_{-0.036}$ | 1                         |

Table 5: Model parameters from joint spectral fit in Xspec. The asterisk symbol indicates that  $\beta$  is given in  $1\sigma$  confidence range

The majority of our sample is composed of short GRBs. This trend can be explained by ASIM’s trigger logic, which functions on extremely short time scales, from  $300\ \mu\text{s}$  to  $20\ \text{ms}$ . These time scales are much shorter than those typical for GRBs. ASIM’s main focus is the detection of TGFs, which are characterized by their very brief flashes.  $E_{peak}$  is relatively high in most fits, indicating the energy where most of the power per energy bin is emitted (see sections 4.3.2 and 4.3.4). The average  $\beta$  value in our sample is around -2.86, which defines the spectral shape in the high-energy regime. A more negative  $\beta$  value would mean a steeper shape of the spectrum, i.e., the counts per second per energy bin would fall off more sharply, whereas a less negative value would mean that the count rate per energy bin would be more consistent, i.e., the count rate at higher energies is still relatively high.

Figure 11 present the folded and unfolded spectra of GRB 201227A and 190606A, along with fit residuals

of our joint spectral analysis. Figures 11a and 11c shows the observed (data points with error bars) and predicted count spectra obtained from the best fit Band model. The color-coded data used in the analysis are as follows: black for KW low energy spectrum, red for KW high energy spectrum, green for Fermi/GBM NaI detector, blue for Fermi/GBM BGO detector, and cyan for ASIM/HED.

The logarithmic scale is used for all axes except for the residuals between  $C_p(I)$  and  $C(I)$ , which are shown in the lower plot of the figures. It's worth noting that I excluded channels for the Fermi BGO detector above  $\sim 4$  MeV due to the `grppha` program flagging those higher channels as dubious when grouping the energy channels, because of low count statistics, and the same is true for the KW spectra. Because of this, only HED has valid high-energy data points in the 10 MeV range.

In Figures 11b and 11d, we observe the unfolded model. For GRB 201227A, the spectral shape is well-defined, with the  $E_{peak}$  parameter from the Band function at approximately 950 keV in the top plot. Beyond the peak, the count rate gradually declines. In contrast, the unfolded spectrum of GRB 190606A (bottom plot) displays an  $E_{peak}$  of around 1750 keV. Following the peak, the count rate remains high, which is unlike the unfolded spectrum of GRB 201227A.

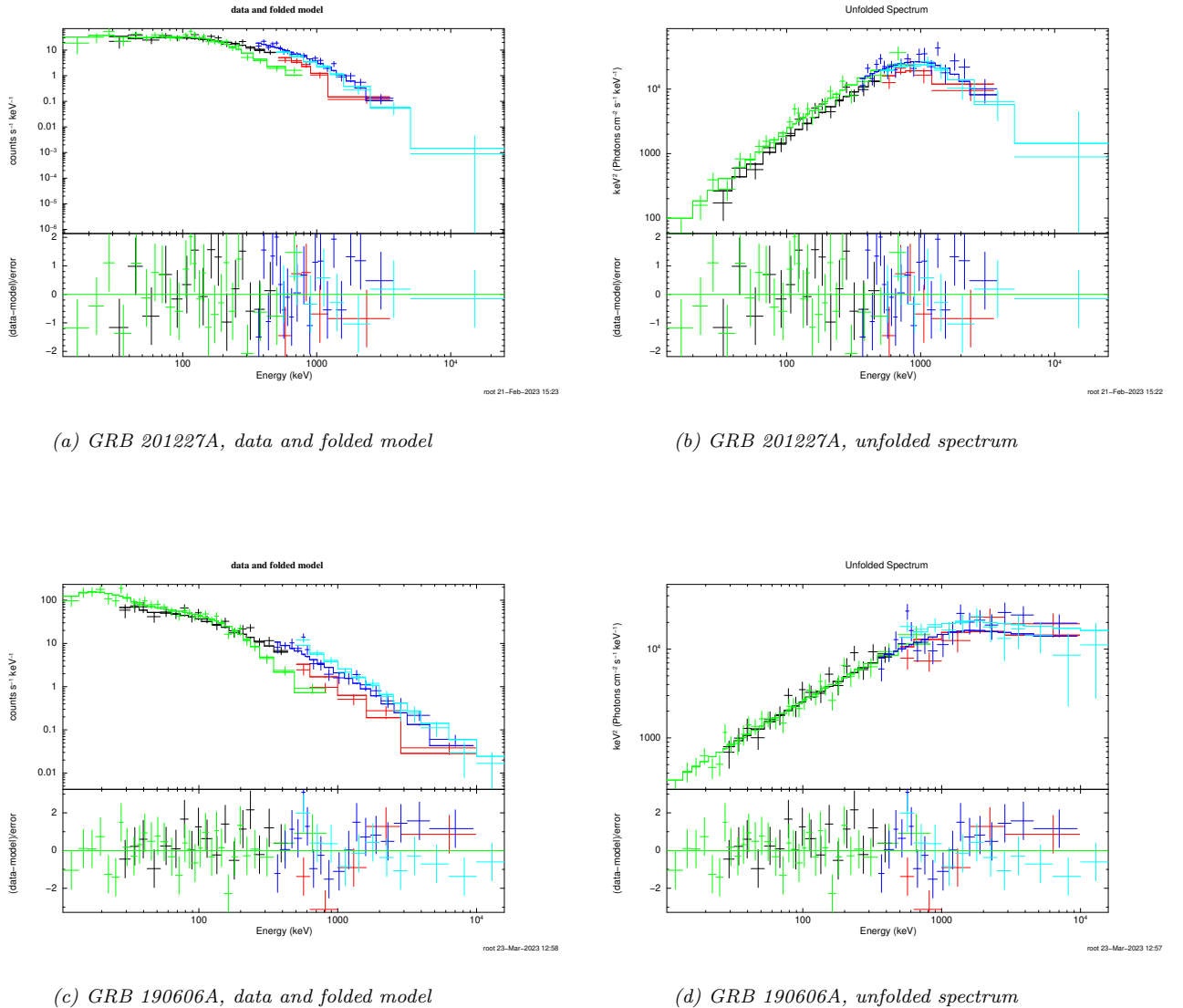


Figure 11: Joint spectral fit of GRB 201227A and 190606A. Band model used to fit all spectra. Color coding: black & red: KW low and high energy spectra, green & blue: Fermi/GBM NaI and BGO, cyan: HED

One of the most interesting parameters in Table 5 is the constant normalization factor  $C_A$ , which measures the agreement between the HED and KW detector. This constant factor is an essential parameter that delivers insights into the systematic uncertainties of the instrument's DRM. It adjusts for differences in the effective areas of the instruments across various energy ranges. Ideally, the constant factor(s) in the joint spectral fit should be close to unity. This indicates that the DRM's and cross-calibration procedures have been effectively calibrated to the instruments, and the various spectral files have been implemented correctly. I observe large deviations from unity in  $C_A$  for 190206A, 190305A and 211211A. These led to a thorough investigation in our data preparation pipeline, which is discussed further in section 5.3. I observe that  $C_F$  is within expected range of unity in our joint spectral analysis.

Prior to performing the joint spectral fit, I first fitted the KW spectra alone. The resulting data for each GRB can be found in Table 6. This table lists the GRB identification number, the interval used for fitting, the applied model, the resulting model parameters including  $\alpha$ ,  $\beta$ , and  $E_{peak}$ , as well as the goodness of fit represented by  $\chi^2/\text{dof}$ .

Because I use the KW spectra as a reference point (except for GRB 211211A) and fix the constant normalization factor to unity, it was necessary to ensure that the KW spectra were properly modeled and loaded into the Xspec program. The fits are generally satisfactory, with most bursts having  $\chi^2/\text{dof}$  values near unity. Some bursts are well-fitted using a Band function, whereas others require a CPL. If the latter is the case, results are provided for the CPL model parameters only. In Figure 12, I employ the findings to illustrate a comparative analysis of the model parameters derived from both the KW fit and the joint fit.

However, the largest reduced  $\chi^2$  is obtained for GRB210619B (Interval 2). In this case, the spectrum was accumulated over 2.048 seconds, i.e., a complex structure with several peaks was included in the spectra. Figure 20 shows the LC for this particular burst, and we clearly observe this complexity in the burst profile. A more accurate approach would have been to subdivide these peaks into separate intervals, as done in the case study presented in section 5.4.1. However, it is important to note that I was unable to use the KW spectra in this case study due to the fixed time intervals for KW spectra. As a result, we cannot fit the KW spectra to the time-resolved spectral analysis performed with HED and GBM, since their time intervals do not align.

| <b>GRB</b> | <b>Int.</b> | <b>Model</b> | <b><math>\alpha</math></b> | <b><math>\beta</math></b> | <b><math>E_{peak}</math> [keV]</b> | <b><math>\chi^2 / \text{dof}</math></b> |
|------------|-------------|--------------|----------------------------|---------------------------|------------------------------------|---|
| 181222B    | 1           | Band         | $-0.520^{+0.085}_{-0.076}$ | $-2.98^{+0.216}_{-0.314}$ | $368^{+28}_{-29}$                  | 52/61 (0.85)                            |
|            | 2           | Band         | $-0.110^{+0.126}_{-0.112}$ | $-3.53^{+0.410}_{-0.836}$ | $417^{+31}_{-32}$                  | 50/50 (1.00)                            |
| 190206A    | 1           | Band         | $-0.501^{+0.101}_{-0.100}$ | $-2.95^{+0.472}_{-2.95}$  | $1402^{+366}_{-324}$               | 30/27 (1.11)                            |
|            | 1           | CPL          | $0.788^{+0.110}_{-0.113}$  | _____                     | $1757^{+291}_{-781}$               | 22/31 (0.72)                            |
| 190305A    | 1           | Band         | $-0.162^{+0.072}_{-0.067}$ | $-2.96^{+0.127}_{-0.158}$ | $425^{+21}_{-21}$                  | 89/64 (1.40)                            |
| 190606A    | 1           | Band         | $-0.645^{+0.515}_{-0.367}$ | $-1.71^{+0.150}_{-0.218}$ | $435^{+308}_{-202}$                | 22/21 (1.05)                            |
| 200521A    | 1           | CPL          | $0.259^{+0.131}_{-0.141}$  | _____                     | $1333^{+195}_{-166}$               | 34/43 (0.79)                            |
|            | 1           | Band         | $-0.272^{+0.136}_{-0.141}$ | $-7.75^{+1.5}_{-1.5}$     | $1336^{+199}_{-131}$               | 33/37 (0.89)                            |
| 200716C    | 1           | Band         | $-0.544^{+0.208}_{-0.163}$ | $-2.31^{+0.284}_{-0.620}$ | $667^{+180}_{-153}$                | 54/48 (1.13)                            |
| 201227A    | 1           | CPL          | $0.19^{+0.370}_{-0.003}$   | _____                     | $882^{+138}_{-114}$                | 21/22 (0.95)                            |
|            | 1           | Band         | $-0.175^{+0.256}_{-0.187}$ | $-3.67^{+1.27}_{-3.62}$   | $858^{+142}_{-175}$                | 21/21 (0.99)                            |
| 210619B    | 1           | Band         | $-0.427^{+0.122}_{-0.109}$ | $-2.06^{+0.090}_{-0.114}$ | $587^{+94}_{-78}$                  | 92/74 (1.24)                            |
|            | 2           | Band         | $-0.500^{+0.061}_{-0.057}$ | $-2.01^{+0.036}_{-0.039}$ | $433^{+30}_{-28}$                  | 145/93 (1.56)                           |

Table 6: Model parameters from all the available KW spectrums. Some are fitted with the Band model, while others are fitted with the cutoff powerlaw model

A similar approach as outlined in Sakamoto et al. (2011) is followed to investigate if there are any systematic trends in the model parameters obtained from the joint spectral analysis and the KW fit alone. In Figure 12, three scatter plots are presented that depict the correlation between the Band parameters  $\alpha$ ,  $\beta$ , and  $E_{peak}$  obtained for the KW-ASIM and KW-only spectral analysis. Each subplot displays the values of one parameter obtained from the KW-only model on the  $x$ -axis and the corresponding values obtained from the KW-ASIM model on the  $y$ -axis. Horizontal and vertical lines represent the upper and lower error bars. A dashed black line is plotted in each subplot to indicate the line of equality where the values from both models would be the same. It is important to keep in mind that the spectral analysis of the KW data only, for some bursts, is best fitted by a CPL model, not the Band model.

While KW-ASIM values are generally consistent with KW-only values, deviations from the line of equality are observed, particularly for the  $E_{peak}$  plot. In most cases, the agreement is good, but outliers are present. Noteworthy for GRB 190606A. The discrepancy stems from the energy band on which the data is fitted. Since HED possesses a higher energy band, and the joint fit was conducted up to 40 MeV. As a result, it is expected that the  $E_{peak}$  will be significantly higher for this hard burst. It should also be noted that the reported  $E_{peak}$ -value in the GCN for the KW spectrum of this particular burst is  $664(+1038, -388)$  keV. The spectrum for this burst can be seen in Figure 11.

Figure 13 presents a stacked scatter plot illustrating the cross-calibration coefficients obtained from the

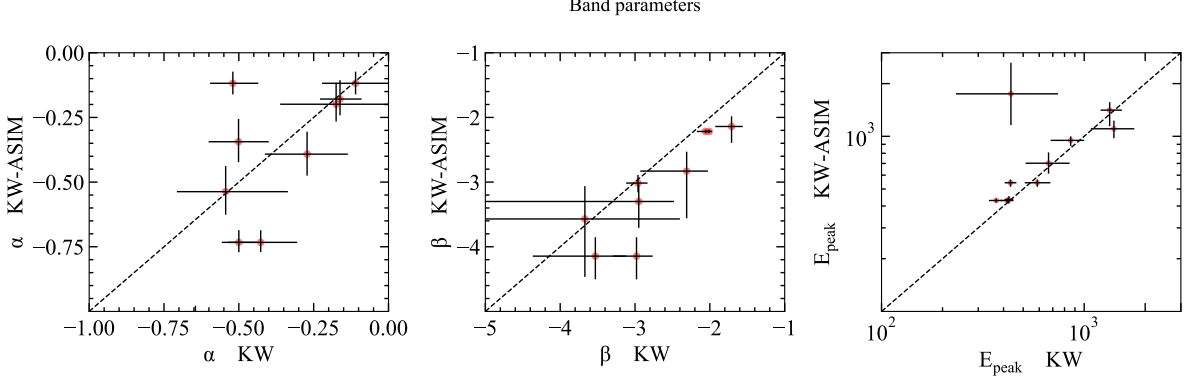


Figure 12: Scatter plots showing the correlation between the Band parameters obtained for the KW-ASIM and KW-only spectral analysis. These are bursts included: GRB 181222B, 190206A, 190305A, 190606A, 200521A, 200716C, 201227A, 210619B. Both intervals for 181222B and 210619B are included as separate data points

joint spectral analysis of KW-ASIM-Fermi, KW-ASIM, and Fermi-ASIM. The top three subplots display the cross-correlation coefficient ( $C_F$ ) as a function of  $\alpha$ ,  $\beta$ , and  $E_{peak}$  for KW-ASIM-Fermi joint spectral analysis. The bottom three subplots show the cross-correlation coefficient for ASIM ( $C_A$ ). Red dots indicate KW-ASIM-Fermi joint spectral analysis data, while blue data points represent KW-ASIM joint spectral analysis data. Additionally, green data points represent the joint spectral analysis of GRB 211211A between ASIM and Fermi/GBM. The green dashed line in each subplot represents the expected cross-calibration coefficient of 1. Each subplot displays upper and lower error bars. Outliers observed in the bottom plot are GRB 190206A, 190305A, and 211211A.

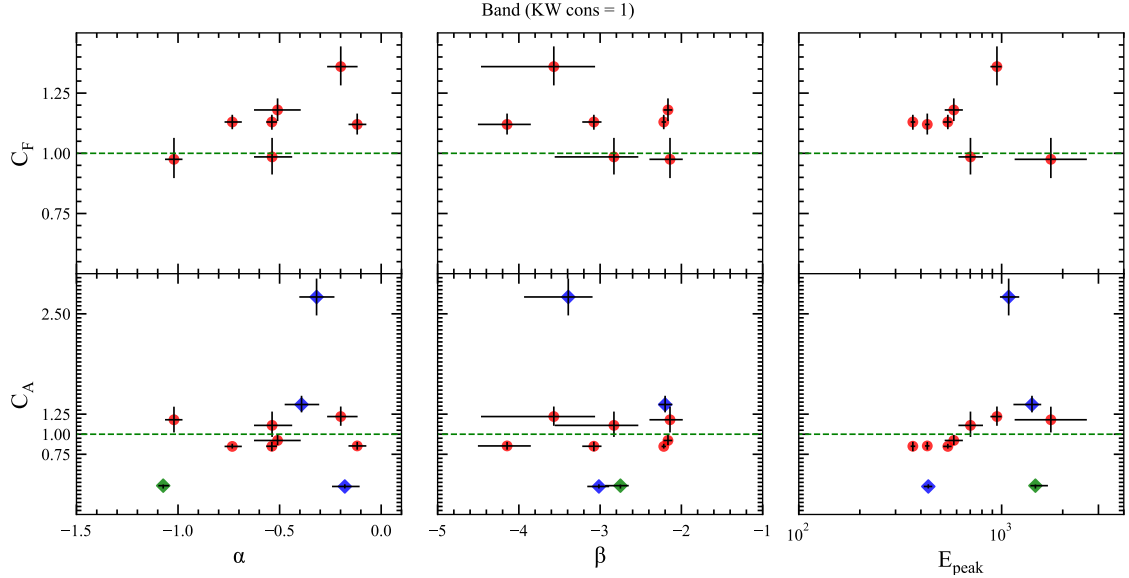


Figure 13: Stacked scatter plots showing the cross-calibration coefficients obtained for KW-ASIM-Fermi (red), KW-ASIM (blue) and ASIM-Fermi (green) joint spectral analysis

Unfortunately, the cross-calibration coefficient for ASIM ( $C_A$ ) deviates from the expected value of 1 for some bursts. This prompted us to perform a data consistency check for ASIM. I am currently investigating the cause of these discrepancies, and it is possible that errors may have occurred in our data preparation pipeline. Our starting point for this investigation is the polar plot shown in Figure 14, which displays the angle  $\vartheta, \varphi$  of incoming GRBs as viewed by the MXGS, with scatter points representing the data. The color of these points indicates whether the normalization constant factor for HED ( $C_A$ ) falls within the acceptable range. Gray shaded areas are designated as Sector I and II to label regions that are occulted by the Columbus module and the Earth, respectively. The numbers in the plot refer to the event index shown in Table 2, which presents the bursts in chronological order.

The plot reveals that most of the GRB data points in our sample are clustered in the fourth quadrant, corresponding to the lower right corner of the plot. It is currently unclear why the data points are distributed in this manner, and it is possible that this is simply due to chance coincidence, given the limited number of data points available.

It is worth mentioning that the outliers in  $C_A$  are not outliers in the spectral parameters, as seen in Figure 13. This means that even if the flux may be incorrect for some directions, the spectral parameters can still be considered reliable.

In the subsequent sections, I will elaborate on the steps taken to investigate the discrepancies and verify the precision of our ASIM data analysis pipeline.

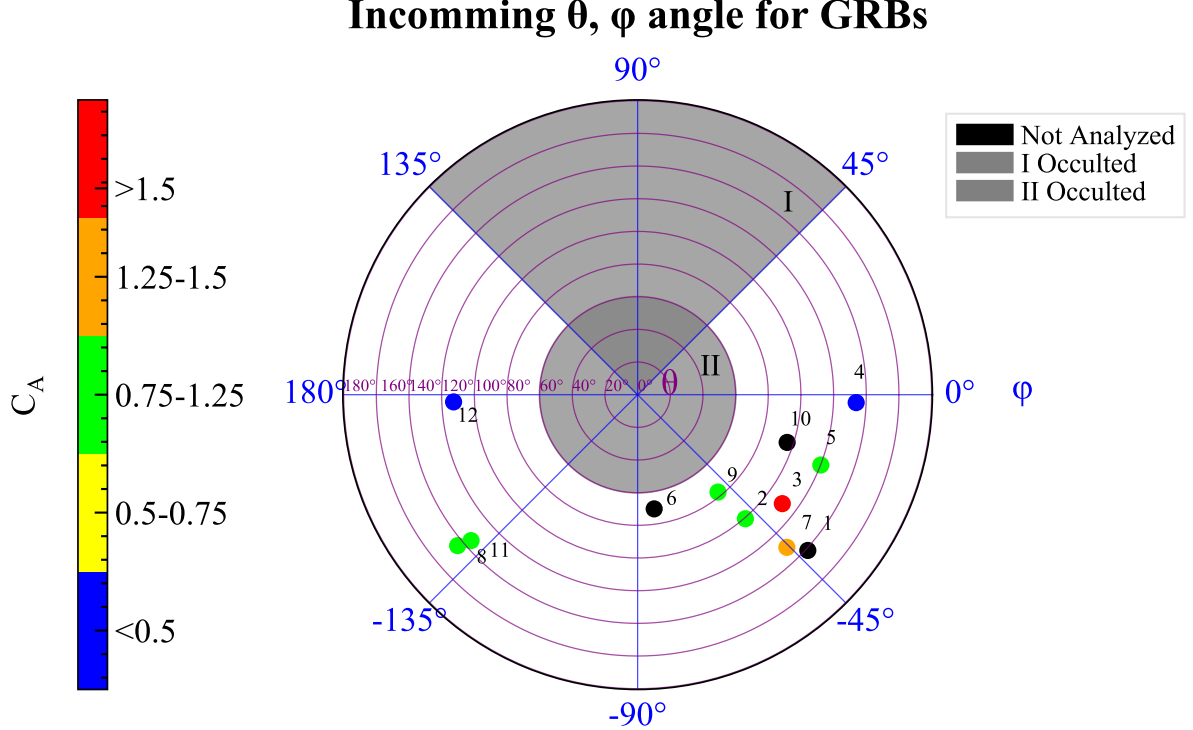


Figure 14: Polar plot illustrating the cross-calibration coefficient  $C_A$  for incoming GRBs as data points, based on their angle of incidence ( $\vartheta, \varphi$ ) as observed by the MXGS. The color-coded points represent the  $C_A$  values

## 5.3 ASIM Data Analysis Pipeline Consistency Check

### 5.3.1 Light Curve Analysis

In the light curve (LC) analysis, I aim to confirm that the spectrum was accumulated at appropriate time interval for the selected GRBs that had large deviations in the cross-calibration coefficients. Initially, I conjectured that I may have extracted the wrong spectrum at the incorrect time interval, so I conducted a LC analysis to investigate this possibility further. This entailed plotting the LC for the relevant spectrum accumulation interval. I concluded that another factor must be responsible for the cross-calibration coefficient discrepancy.

### 5.3.2 Background Ratemeter Analysis

I assessed the reliability of the accumulated background spectra by analyzing the ASIM instrument's background ratemeter at the given magnetic latitude (mlat). The background ratemeter data, recorded every 30 seconds, includes information about count rate, time [UT], latitude, longitude, and altitude of the ISS. ASIM encounters high background radiation at high mlat due to cosmic rays, which increase the background rate by allowing more low-energy particles (protons) to penetrate deeper into the magnetosphere. In contrast, at lower mlat, ASIM experiences a lower background rate as low-energy particles are deflected or scattered at higher altitudes in Earth's magnetosphere.

ASIM employs a protective mechanism called 'decimation mode' to handle extremely high count rates and prevent overloading the data handling unit. The detector remains on (PMT HV on) during decimation mode. However, when the ISS passes through the South Atlantic Anomaly (SAA), where charged particles penetrate deeper into the magnetosphere, the detector is turned off (PMT HV off) to protect the PMTs. For more information, refer to Section 4.6 in Østgaard et al. (2019). I confirmed that the decimation mode was not activated during any background spectrum accumulation times.

The analysis commenced with a ratemeter examination of 15 ISS orbits, during which the background count rate, datetime, latitude, longitude, and altitude of ASIM were extracted for each sample. The mlat was then estimated using the `ApexPy` library, and a scatter plot of the ratemeter versus mlat was created using MATLAB. Mathematical polynomials and functions were employed to approximate the data and estimate the envelope of the ratemeter data points.

Subsequently, the background count rate (cts/s) for all background files used in the spectral analysis was calculated. In some instances, the background found in the same trigger data as the burst was utilized, while in others, a separate trigger file sufficiently close in time to the burst trigger was employed to accumulate a background.

A similar ratemeter analysis has been conducted previously, with the scatter plot of the background count rate as a function of mlat from the earlier analysis presented in Figure 15.

Lastly, to verify that the background count rate found in the data files used in the analysis was as expected, these values were plotted on top of the estimated background envelope. The background envelope serves as a visual representation of the anticipated range of background count rates for a given mlat. The new ratemeter analysis is presented in Figure 16, which displays the previously described envelope. In this plot, the background count rate from the GRBs, along with the corresponding mlat, are depicted as data points (stars and GRB identification). The plot demonstrates that the data points fall within the background envelope, suggesting that the background spectral files used in the spectral analysis possess the expected count rate at the specified mlat. Consequently, an incorrect background is ruled out as the cause for the anomalous cross-calibration coefficients.

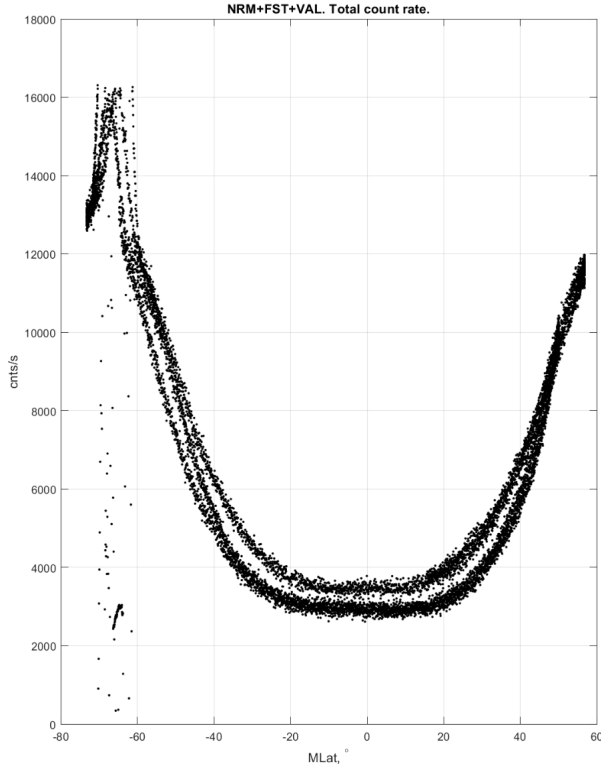


Figure 15: Previously conducted ratemeter analysis taken during the commissioning phase of ASIM

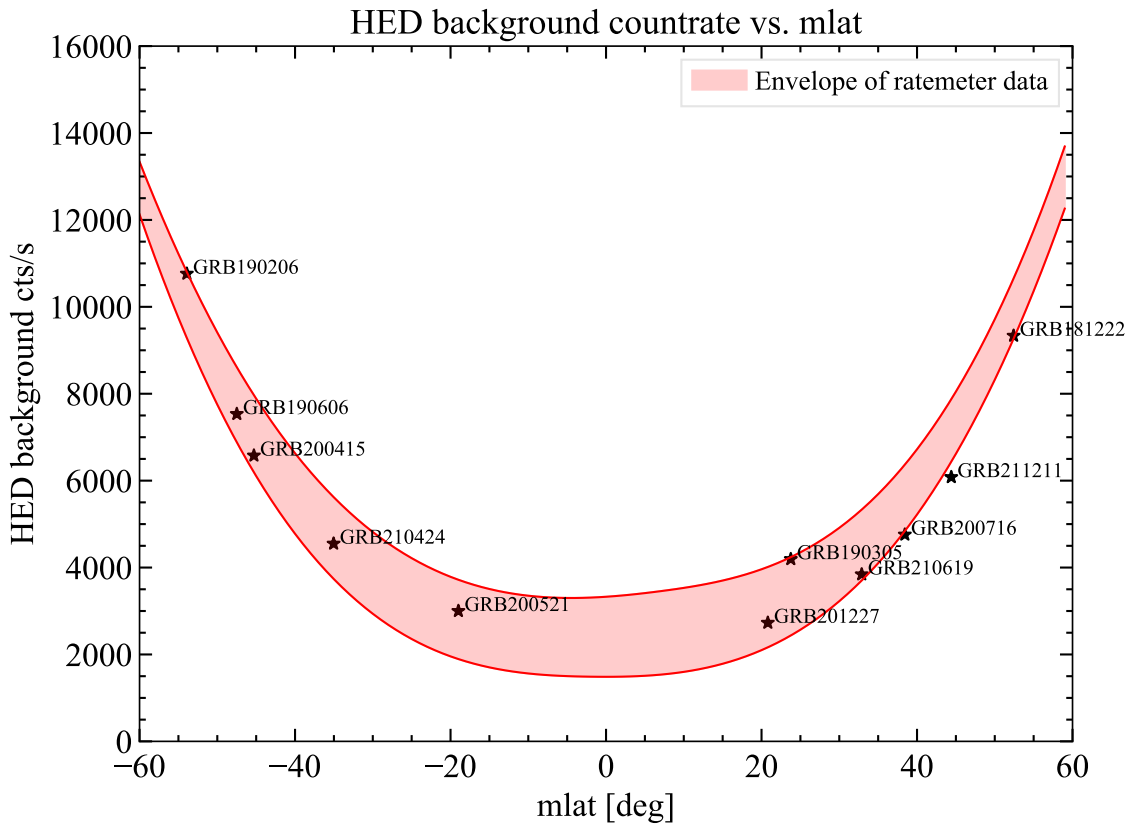
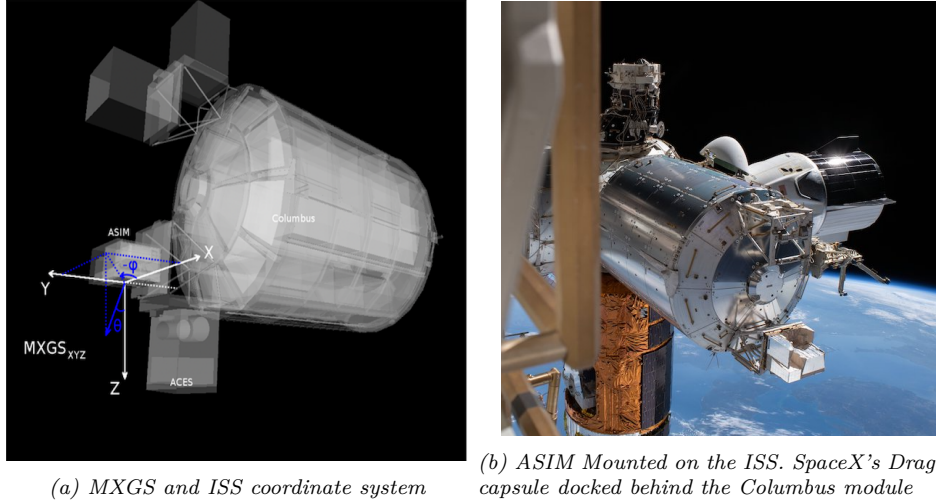


Figure 16: Envelope in shaded red showing the expected count rate for the given magnetic latitude.

### 5.3.3 DRM Analysis

Preparing the Detector Response Matrix (DRM) is a critical step in the data pipeline, and obtaining the appropriate DRM for each burst is essential and based on its incident angle ( $\vartheta, \varphi$ ). For further details on the DRMs analyzed in this section, refer to section 3.2.1. Note that I only analyzed the DRMs applicable for HED, since I used data from HED in the joint spectral analysis.

To ensure that the reference frames for the DRM and GRBs were aligned, I investigated the coordinate system used. Figure 17a shows the MXGS coordinate system, with polar  $\vartheta$  and azimuthal  $\varphi$  indicated on the axis. The Columbus module is located at  $\varphi \approx 90^\circ$  due to the **negative definition of  $\varphi$**  in the coordinate system. See also Figure 17b for another point of view of ASIM.



(b) ASIM Mounted on the ISS. SpaceX's Dragon capsule docked behind the Columbus module

Figure 17

In order to identify potential discrepancies, it was crucial to verify that the DRMs accurately account for the absorption caused by the Columbus module around  $+90^\circ$ . The DRMs are defined for specific polar and azimuthal angles with  $15^\circ$  steps, as outlined in Section 3.2.1. To validate the DRMs and examine if the opposite  $\varphi$ -angle led to discrepancies, I selected a  $\vartheta$  of  $120^\circ$  and an energy channel corresponding to a 1 MeV photon. I then calculated the effective area across the  $\varphi$ -angles by summing up energy channels in the DRMs that met these criteria.

Figure 18, which was generated using data from 13 DRMs, displays the effective area in  $\text{cm}^2$  for the DRMs with  $\vartheta = 120^\circ$  on the y-axis, plotted against the  $\varphi$ -angle range on the x-axis. The observed decrease in effective area around the  $\varphi$  region where the Columbus module is situated ( $45^\circ$  to  $135^\circ$ ) suggests that the DRMs correctly account for the module. Furthermore, I examined the responses for  $\vartheta = 90^\circ$  and  $105^\circ$  at 0.5 and 1 MeV and found no discrepancies in the effective area. I also confirmed the anticipated occultation due to the Columbus module within the same  $\varphi$  interval observed in Figure 18. These results indicate that the reference frames for the DRM and GRBs are consistent.

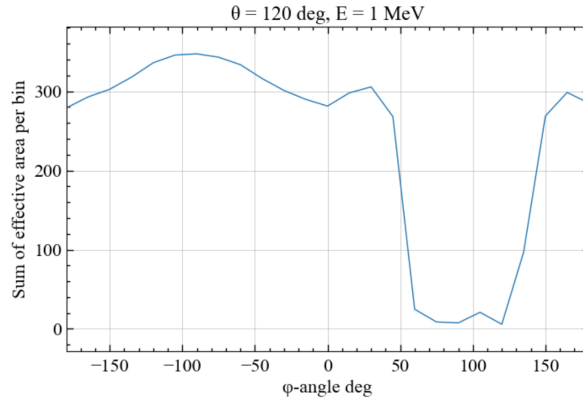


Figure 18: Effective area for HED

### 5.3.4 Energy Calibration Coefficients Analysis

Our investigation led us to clarify whether discrepancies in the constant normalization factor can result from energy calibration coefficients that are significantly off during a specific burst (e.g., due to peak misidentification). I analyzed our sample of GRBs with this question in mind. Consequently, I extracted the energy calibration coefficients used in our GRB sample and sampled those closest in time to our T0. I computed the mean, standard deviation, minimum, and maximum of these coefficients for each BGO detector.

Ultimately, I produced scatter plots of each coefficient's mean as data points and the standard deviations of the mean as vertical error bars. These statistics can be found in Figure 19. The top row is for the energy calibration coefficients sampled for the GRBs that had a constant factor ( $C_A$ ) close to unity, while the second row is the coefficients from the GRB sample that have a constant factor that have a large deviation from unity. The left plot shows the cross-calibration coefficient "a", while "b" is in the middle. The leftmost scatter plot details coefficient "c," and it revealed that "DAU 2 DET 3" and "DAU 4 DET 2" had a large error compared to the other data points. This discrepancy suggested that the "c"-value had a wider distribution than other coefficients in the dataset, with a minimum and maximum of 35 and 216, respectively, and a mean of about 60.

Despite this significant variability, we've concluded that energy calibration coefficients are not the source of error. I have to keep in mind that the energy calibration coefficients were sampled over a wide time period. We also applied different sets of calibration parameters to events with non-optimal cross calibration parameter, and we did not obtain significant changes in the fit results.

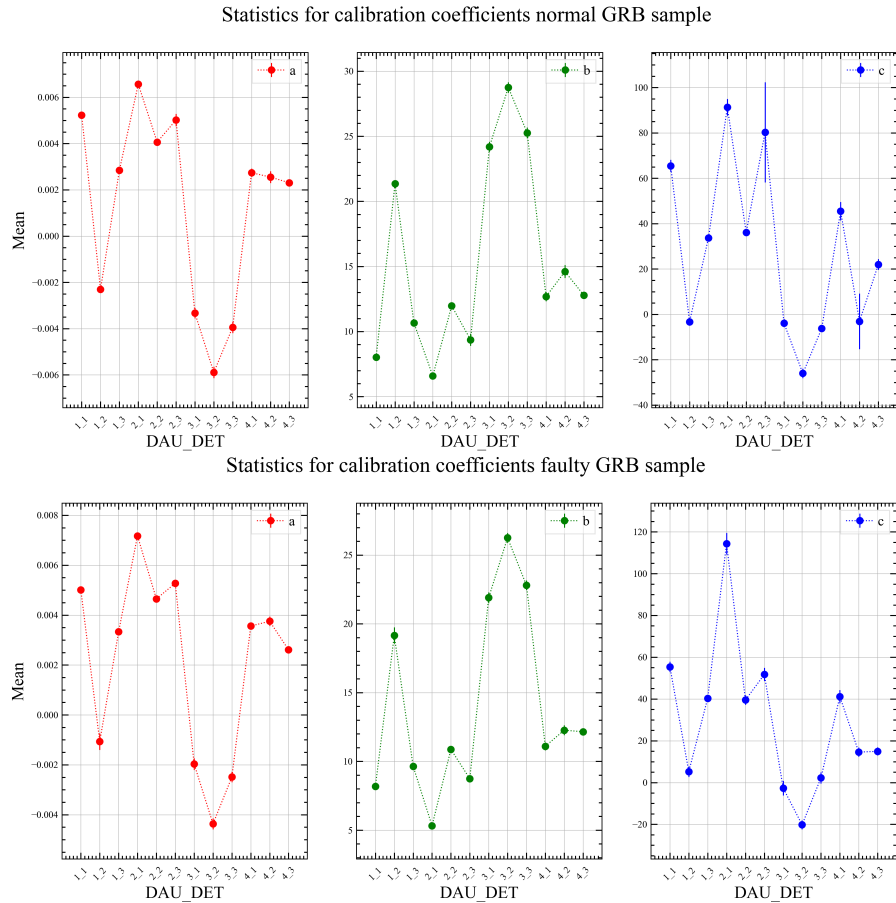


Figure 19: Top plot showing the energy calibration coefficients for all 12 detectors in the "reliable" GRBs, and the bottom showing it for the "unreliable" GRBs

### 5.3.5 Consistency of the Mass Model

Please refer to Figure 14, where GRB 190305A and 211211A are marked as blue data points, indicating a cross-calibration coefficient  $C_A$  less than or equal to 0.5. The mass model may not account for some ASIM payload components at this angle of incidence, as seen in the case of GRB 190305A, which is entering from the PMT side. For 211211A, the gamma-rays also passes through the Data Handling Processing Unit (DHPU), which is not included in the mass model. Efforts are underway to examine the mass model and cross-check it with ASIM's full CAD model to improve response matrices in areas with identified inconsistencies.

### 5.3.6 ASIM FITS Analysis

I confirmed the accuracy of the developed ASIM FITS software by cross-checking the accumulated spectrum with the one used in the spectral analysis of GRB200415A, as presented in the magnetar study by Castro-Tirado et al. (2021). This validation ensures the reliability of the software used in the ASIM data preparation pipeline.

## 5.4 Case Studies

In this case study section, two peculiar gamma-ray bursts, GRB 210619B and GRB 211211A, are examined. GRB 210619B, originating from a faint dwarf galaxy with a redshift of  $z=1.937$ , provided insights into the environments of powerful GRBs. Time-resolved spectral analysis revealed a transition from thermal to non-thermal outflow, highlighting the burst's evolving spectral properties. Due to the fixed intervals of the KW spectra, it was not possible to utilize them for the time-resolved spectral analysis presented in this case study. Instead, ASIM/HED and Fermi/GBM spectra were employed for the time-resolved spectral analysis.

GRB 211211A, displaying features of both long and short bursts, was analyzed using light curve cross-correlation with Fermi, ASIM data preparation, and spectral fitting. This burst is thought to originate from the merger of two compact objects. The joint spectral analysis of intervals 1 and 3 revealed the most energetic intervals, offering a deeper understanding of this enigmatic event. Folded and unfolded spectra for GRB 211211A and 210619B can be found in Appendix A.

### 5.4.1 GRB 210619B

GRB 210619B, has a redshift of  $z=1.937$  and it originates from a faint dwarf galaxy. Dwarf galaxies are composed of 1000 up to several Billion stars. Our galaxy, the Milky Way has around 200-400 Billion stars. By using standard cosmological constants  $H_0$  (Hubble constant),  $\Omega_{matter}$  (mass density or ordinary matter plus dark energy),  $\Omega_\Lambda$  (effective mass density of dark energy), and  $E_{\gamma,iso}$  (isotropic energy release of the burst), I estimated that the 'look back time' to this dwarf galaxy is roughly 10.07 Billion years.<sup>12,13,14</sup> This GRB is contributing to our understanding of the environments in which such powerful gamma-ray bursts occur.

GRB 210619B, an exceptionally luminous burst ranking among the top 10 observed by Fermi, exhibits a prompt emission light curve characterized by a remarkably bright hard emission pulse—an intense high-energy radiation flash—followed by softer, prolonged pulses. Time-resolved spectral analysis reveals a transition from thermal to non-thermal outflow, providing insights into the burst's evolving spectral properties.

In our contribution to the comprehensive multi-wavelength study of GRB 210619B, I provided the ASIM/HED and Fermi/GBM data that was used to analyze the radiation mechanisms and jet composition of this extraordinary burst.

In Figure 20, I present the superimposed light curves of ASIM/HED and Fermi/GBM. Backgrounds have been removed from both light curves. The HED light curve has been shifted by 646 ms to achieve maximal cross-correlation between the light curves. Counts detected are plotted on the y-axis in relation to the time from the ASIM trigger time ( $T_0$ ) on the x-axis. The histogram bin size is 50 ms.

In Table 7 the time intervals that I used to extract the spectra for the our time-resolved spectral analysis.

| GRB     | Interval | $t_i$ | $t_f$ |
|---------|----------|-------|-------|
| 210619B | 1        | 0.00  | 1.00  |
|         | 2        | 1.00  | 1.70  |
|         | 3        | 1.70  | 2.18  |
|         | 4        | 2.18  | 2.79  |
|         | 5        | 2.79  | 3.60  |
|         | 6        | 3.60  | 4.50  |

Table 7: Spectrum accumulation intervals given in seconds for time-initial and time-final

<sup>12</sup>[https://uh.edu/~vanderse/astronomy/uni\\_age.html](https://uh.edu/~vanderse/astronomy/uni_age.html)

<sup>13</sup>[http://faraday.uwyo.edu/~chip/misc/Cosmo2/cosmo1.cgi?z=1.937&H0=68&OM=+0.27&OL=0.73&Lum=3.0e%2B54&c\\_show=true](http://faraday.uwyo.edu/~chip/misc/Cosmo2/cosmo1.cgi?z=1.937&H0=68&OM=+0.27&OL=0.73&Lum=3.0e%2B54&c_show=true)

<sup>14</sup><http://hyperphysics.phy-astr.gsu.edu/hbase/Astro/denpar.html>

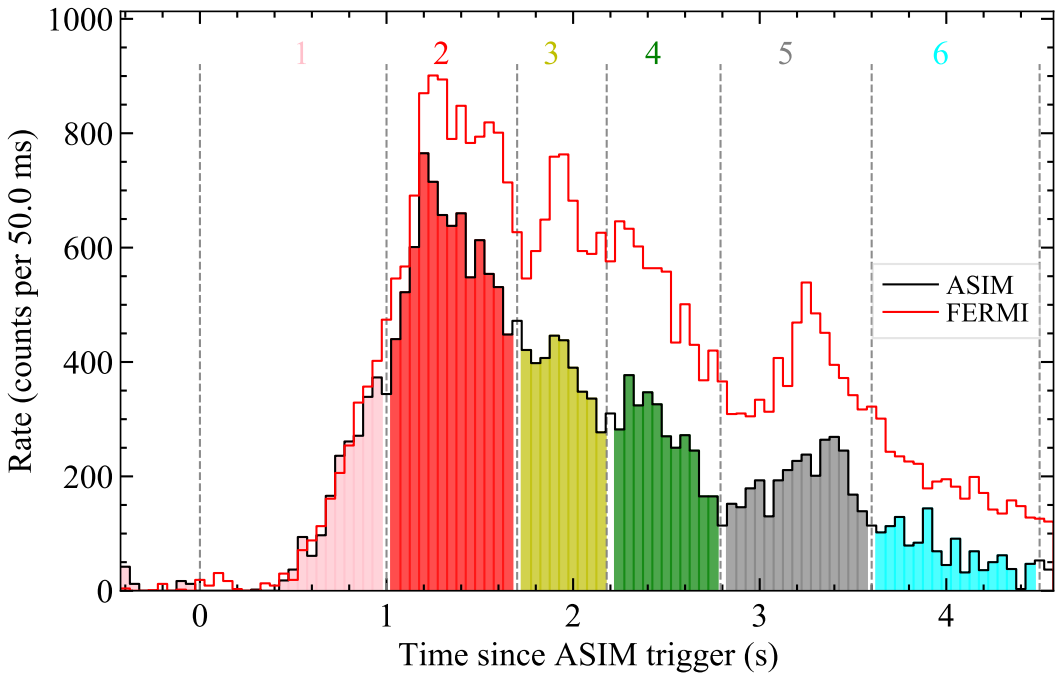


Figure 20: Superimposed LCs for GRB210619B

In Table 8 the model parameters from the fitting the Band model to the spectra. In the multi-wavelength study of the luminous GRB 210619B observed with Fermi and ASIM, it was found that the burst's spectral properties evolved throughout its duration, providing valuable insights into the environment and mechanisms behind such powerful gamma-ray bursts. The analysis demonstrated the importance of multi-wavelength observations in understanding the complex nature of these phenomena.

| GRB     | Int. | $\alpha$                   | $\beta$                   | $E_{peak}$ [keV]    | $\chi^2 / \text{dof}$ |
|---------|------|----------------------------|---------------------------|---------------------|-----------------------|
| 210619B | 1    | $-0.487^{+0.129}_{-0.096}$ | $-1.87^{+0.102}_{-0.120}$ | $755^{+214}_{-187}$ | 323/298 (1.08)        |
|         | 2    | $-0.398^{+0.032}_{-0.030}$ | $-2.16^{+0.025}_{-0.032}$ | $455^{+24}_{-25}$   | 486/344 (1.41)        |
|         | 3    | $-0.555^{+0.039}_{-0.037}$ | $-2.41^{+0.055}_{-0.067}$ | $409^{+31}_{-28}$   | 390/310 (1.26)        |
|         | 4    | $-0.513^{+0.041}_{-0.036}$ | $-2.41^{+0.063}_{-0.065}$ | $312^{+19}_{-19}$   | 468/313 (1.50)        |
|         | 5    | $-0.510^{+0.043}_{-0.041}$ | $-2.30^{+0.057}_{-0.061}$ | $252^{+15}_{-14}$   | 534/322 (1.66)        |
|         | 6    | $-0.706^{+0.090}_{-0.083}$ | $-1.86^{+0.023}_{-0.030}$ | $179^{+19}_{-16}$   | 405/258 (1.57)        |

Table 8: Model parameters for GRB210619B. Errors given in  $2.706\sigma$

In the GRB 210619B paper by Caballero-García et al. (2023), the time-resolved spectral analysis of the burst reveals a transition between thermal outflow during the harder pulse to non-thermal outflow during the softer pulse. The correlation between spectral parameters shows that both peak energy and  $\alpha$  exhibit a flux tracking pattern, which means that these parameters evolve in tandem with the flux, resulting

in a strong correlation. Caballero-García et al. (2023) also report on the electron distribution in the shock is denser or more energetic than what is usually seen in gamma-ray bursts. Overall, the study by Caballero-García et al. (2023) advances our understanding of the complex nature of gamma-ray bursts and their environments, including the radiation mechanisms, jet composition, and the properties of the host galaxies.

#### 5.4.2 GRB 211211A

Consider the peculiar gamma-ray burst, GRB 211211A, which resembles a long burst, yet exhibits numerous characteristics indicative of a short burst typically associated with a merger. This event is believed to result from the union of a  $1.23 M_{\odot}$  neutron star (NS) and an  $8.21 M_{\odot}$  black hole (BH), or a pair of NSs, one of which is a highly magnetized magnetar. Notably, a super flare was observed in the precursor of GRB 211211A. Zhang et al. (2022) propose that this precursor super flare was triggered by tidal forces tearing apart the magnetized magnetar during the terminal stages of the binary system's inspiral phase. Consequently, energy was released from the magnetar's crust and its potent internal and external magnetic fields. The super flare is estimated to be 100s of times more powerful than giant magnetar flares like those reported by Castro-Tirado et al. (2021).

In our study, we performed a light curve cross-correlation with Fermi, prepared ASIM data, and conducted spectral fitting. Figure 21 displays the complete light curve of GRB 211211A, as recorded by ASIM/HED and Fermi/BGO detector. The light curve reveals a multi-peaked complex structure, with the first interval exhibiting the Super Flare precursor, a consequence of the magnetic energy release following the highly magnetized magnetar's disintegration.

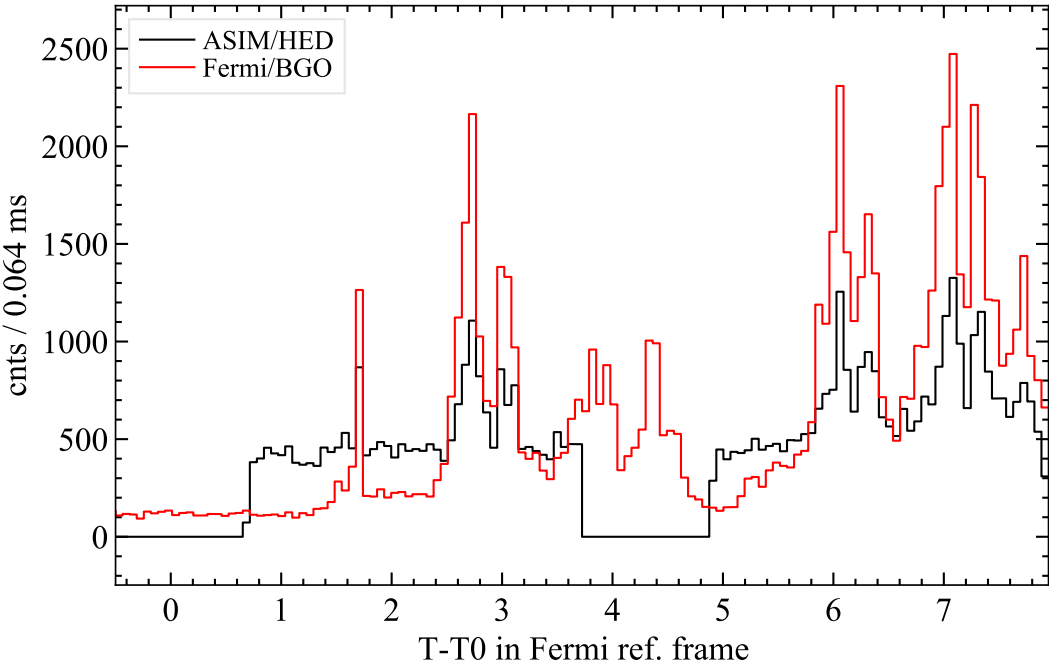


Figure 21: GRB 211211A full light curve

A close-up of intervals 1 to 4 is presented in Figure 22. The start and stop times for these intervals are provided in Table 9.

Table 10 contains the joint spectral analysis of intervals 1 through 4. We fitted the data in Xspec using the Band model. Our time-resolved joint spectral analysis uncovers that intervals 1 and 3 are the most energetic, with  $E_{peak} \sim 1467$  keV and 1563 keV, respectively.

Curiously, the cross-calibration coefficient ( $C_A$ ) for ASIM is lower for intervals with higher  $E_{peak}$  values. This burst is one of our outliers (constant  $\sim 0.5$ ), but as can be inferred from Figure 13, the spectral

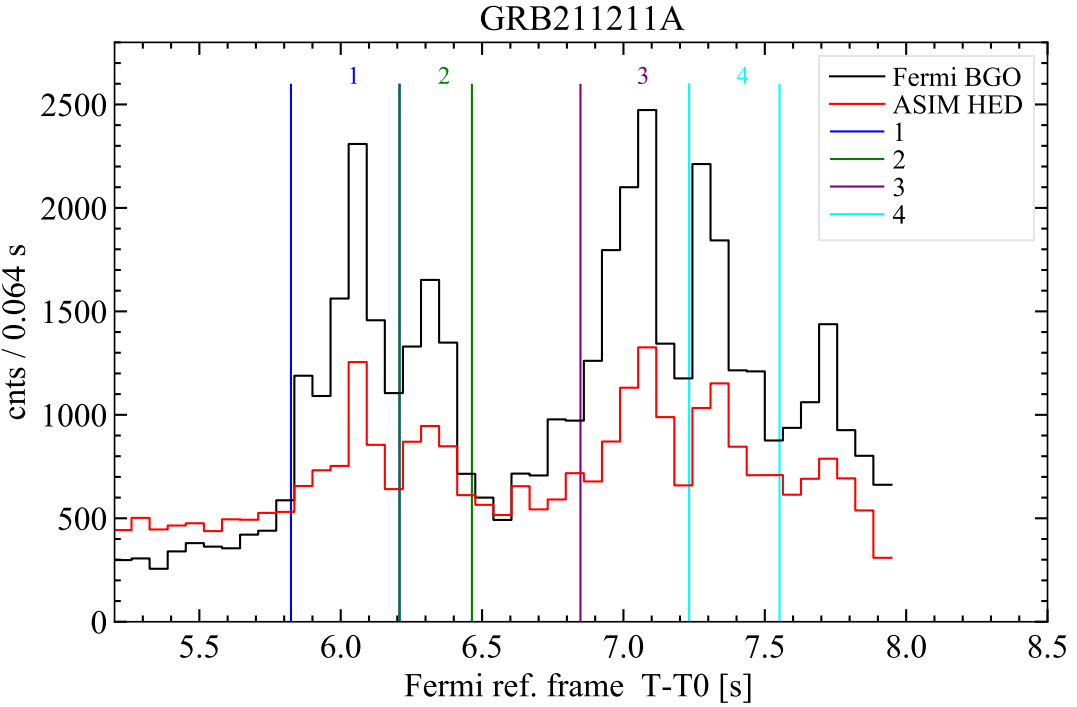


Figure 22: GRB 211211A zoomed in light curve showing spectral intervals

| GRB     | Interval | $t_i$ | $t_f$ |
|---------|----------|-------|-------|
| 211211A | 1        | 5.824 | 6.208 |
|         | 2        | 6.208 | 6.464 |
|         | 3        | 6.848 | 7.232 |
|         | 4        | 7.232 | 7.552 |

Table 9: Spectrum accumulation intervals given in seconds for time-initial and time-final

| GRB     | Int. | $\alpha$                   | $\beta$                   | $E_{peak}$ [keV]     | $\chi^2 / \text{dof}$ | $C_A$                     |
|---------|------|----------------------------|---------------------------|----------------------|-----------------------|---------------------------|
| 211211A | 1    | $-1.073^{+0.030}_{-0.024}$ | $-2.75^{+0.102}_{-0.189}$ | $1467^{+224}_{-82}$  | 246/148 (1.66)        | $0.359^{+0.014}_{-0.036}$ |
|         | 2    | $-0.869^{+0.043}_{-0.041}$ | $-2.38^{+0.084}_{-0.107}$ | $879^{+116}_{-98}$   | 305/168 (1.82)        | $0.504^{+0.043}_{-0.044}$ |
|         | 3    | $-1.08^{+0.026}_{-0.023}$  | $-2.92^{+0.155}_{-0.201}$ | $1563^{+102}_{-122}$ | 222/141 (1.57)        | $0.442^{+0.028}_{-0.027}$ |
|         | 4    | $-0.836^{+0.033}_{-0.030}$ | $-2.52^{+0.087}_{-0.102}$ | $920^{+77}_{-74}$    | 244/168 (1.45)        | $0.525^{+0.04}_{-0.035}$  |

Table 10: Model parameters for GRB 211211A. Errors given in  $2.706\sigma$

parameters should still be representative.

Additionally, ASIM could contribute to the timing analysis of the precursor, given its performance obtained for the 200415A magnetar flare. This detailed examination of GRB 211211A provides valuable

insights into the nature of this peculiar burst, which exhibits characteristics of both long and short gamma-ray bursts, further enhancing our understanding of such enigmatic astronomical events

In Appendix A, the reader can find both the folded and unfolded spectra for the discussed gamma-ray burst, GRB 211211A. These spectra offer additional insights into the burst's behavior, complementing the analysis presented in this main text.

## 6 Summary and outlook

In this master's thesis, I systematically explored cosmic gamma-ray bursts (GRBs) detected by the ASIM instrument for the first time. Between June 1st, 2018 and December 31st, 2021, I identified 12 verified bursts. The case study section highlights two peculiar bursts: GRB 210619B, believed to originate from a distant dwarf galaxy, and GRB 211211A, which is thought to result from the merger of two compact objects. I developed an architecture for extracting ASIM spectra and streamlined the data preparation process using the ASIM Fits program. Additionally, I extracted Fermi spectra for relevant bursts and performed joint spectral analysis of ASIM, KW, and Fermi spectra for a subset of the 12 verified bursts. This thesis presents crucial information about the joint spectral analysis, while Appendix A features the folded and unfolded models for the relevant GRBs.

This work expands the scientific impact of ASIM in directions divergent from the primary mission goals, building upon the foundation laid by the magnetar flare paper Castro-Tirado et al. (2021). The current work will be compiled into a paper, submitted to an Astrophysics journal in collaboration with international partners.

Regarding future work and outlook, efforts have commenced to examine the mass model and cross-check it with the full CAD model of ASIM in order to enhance response matrices in regions where inconsistencies were detected. The analysis of the identified GRB sample will be expanded to include the calculation of duration (T90, T50) and the distribution of ASIM GRBs with respect to the available GRB catalog. The hypothesis is that ASIM detects a low number of GRBs, but these are typically short, bright, and energetic, making them highly interesting for follow-up analysis.

The expertise and code developed will be employed for future GRB analysis from ASIM, particularly as the new LIGO-VIRGO gravitational waves observing run commences in May 2023. A follow-up study of the timing properties of ASIM GRBs will be conducted, leveraging ASIM's excellent timing capabilities. Additionally, the team is studying a follow-up mission of ASIM called TOTEM, which will include a smaller version of MXGS with improved features. The expertise gained now will be utilized to establish a GRB data analysis pipeline for TOTEM.

## A GRB Archive

### A.1 GRB 181222B

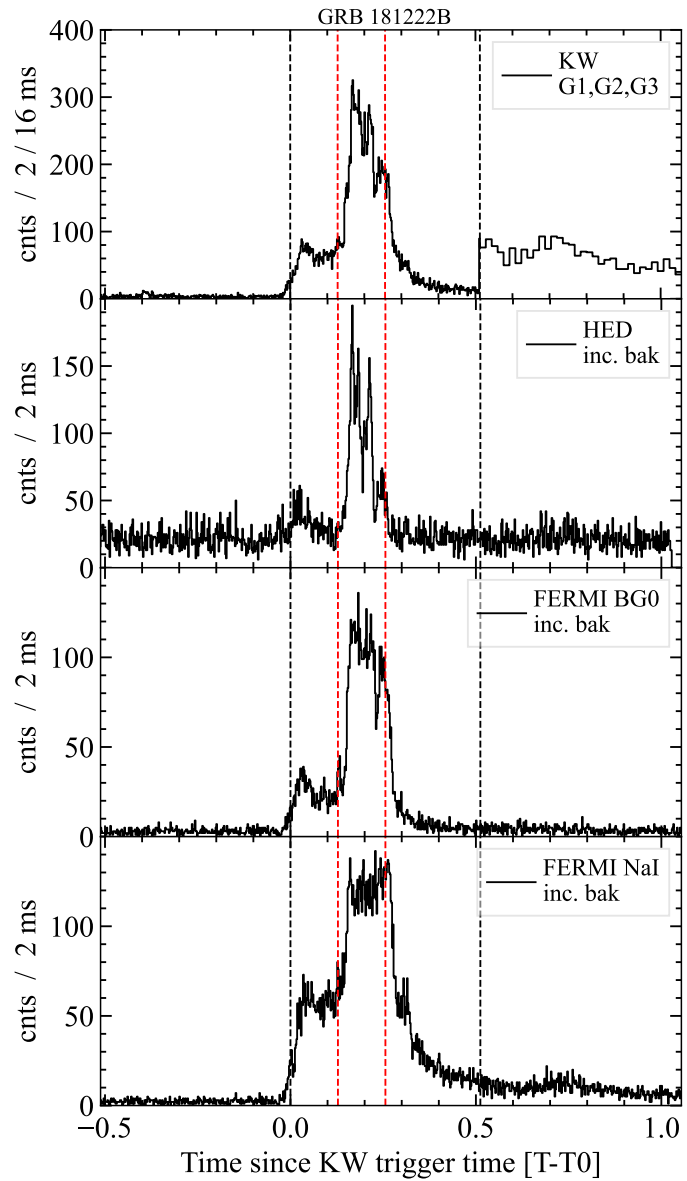


Figure 23:  $T0_{ASIM} = 2018-12-22\ 20:11:36.136$

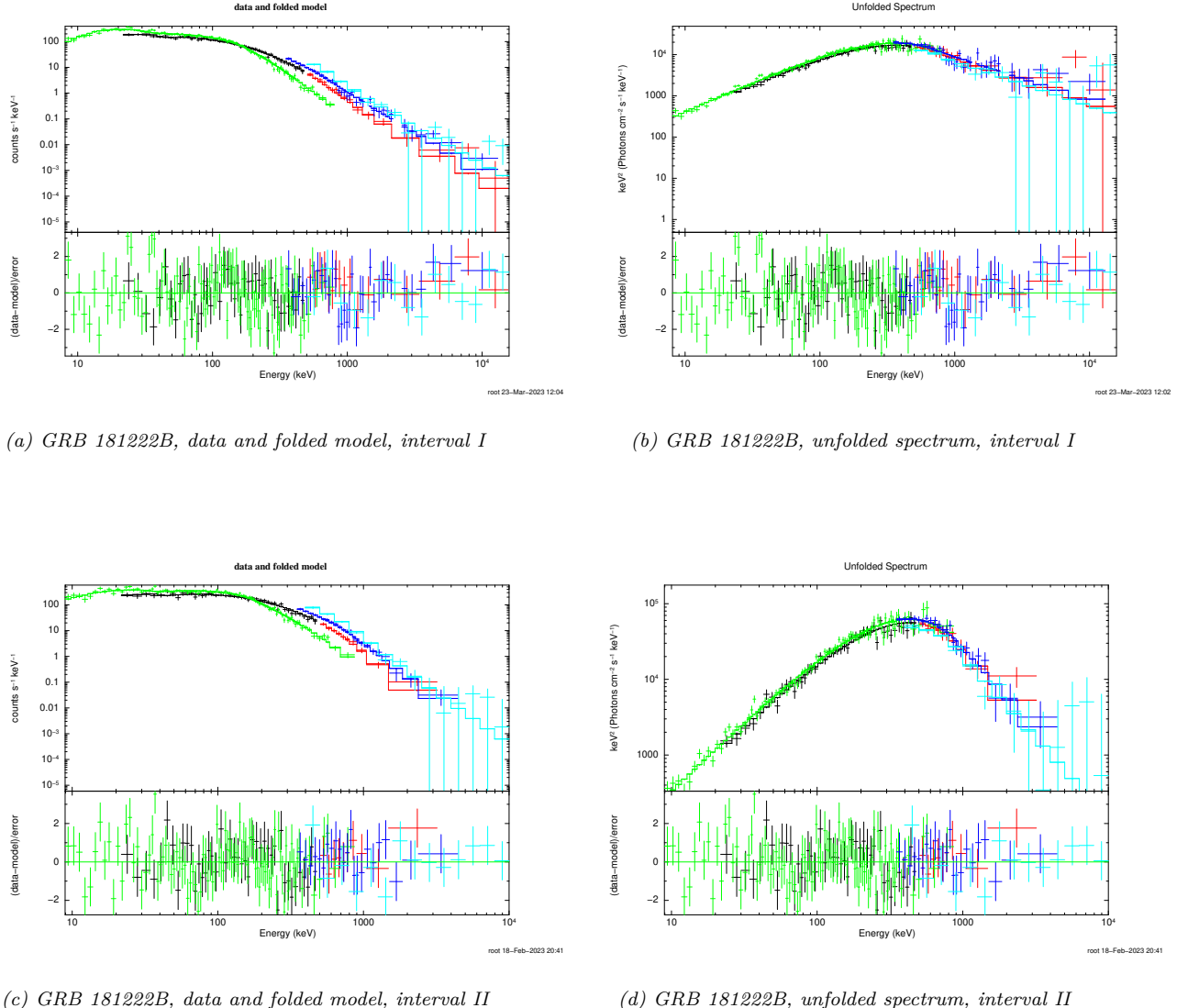
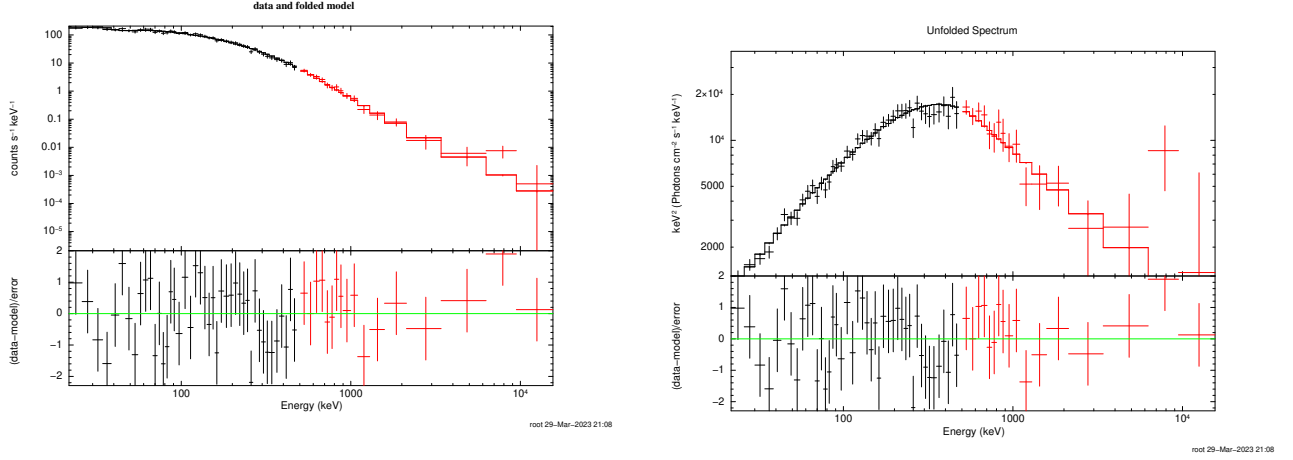


Figure 24: Joint spectral fit of GRB 181222B. Band model used to fit all spectra. Color coding; black & red: KW low and high energy spectra, green & blue: Fermi/GBM NaI and BGO, cyan: HED

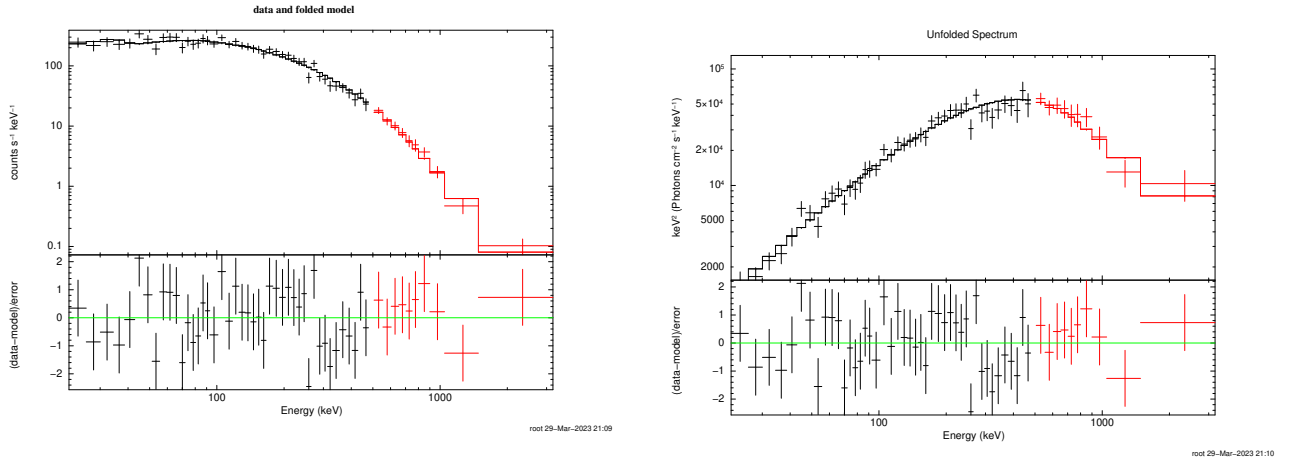
### A.1.1 KW spectra



(a) GRB 181222B, KW data and folded model, interval I

(b) GRB 181222B, KW unfolded spectrum, interval I

Figure 25: KW fit of GRB 181222B. Band model used to fit spectra. Color coding; black & red: KW low and high energy spectra



(a) GRB 181222B, KW data and folded model, interval II

(b) GRB 181222B, KW unfolded spectrum, interval II

Figure 26: KW fit of GRB 181222B. Band model used to fit spectra. Color coding; black & red: KW low and high energy spectra

## A.2 GRB 190206A

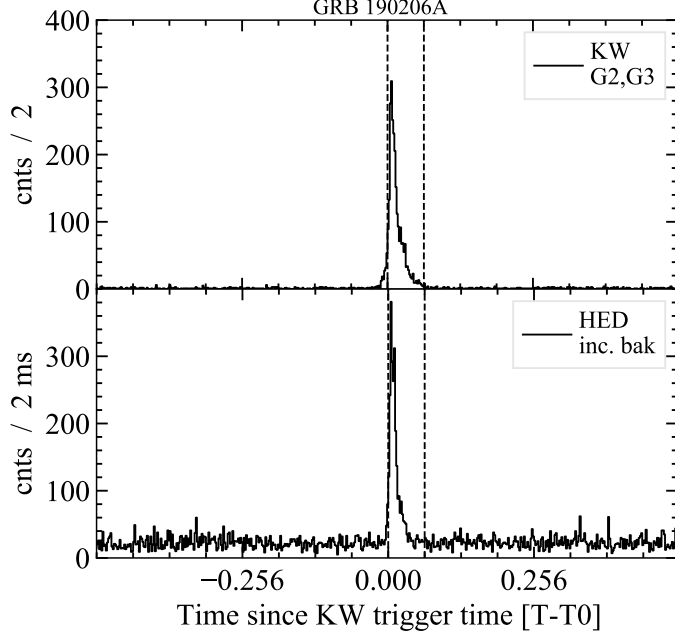
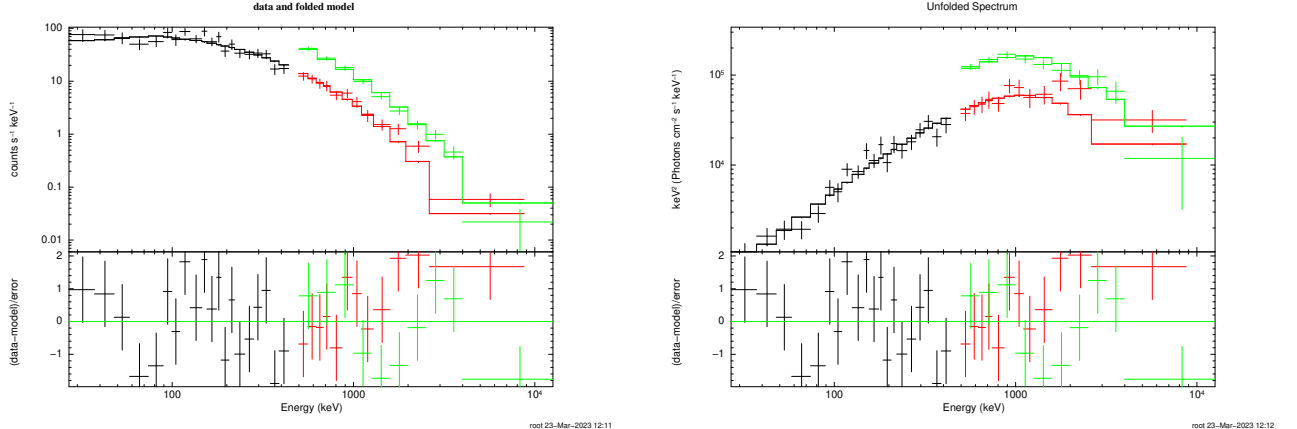


Figure 27:  $T0_{ASIM} = 2019-02-06\ 03:49:28.229$



(a) GRB 190206A, data and folded model, interval I

(b) GRB 190206A, unfolded spectrum, interval I

Figure 28: Joint spectral fit of GRB 190206A. Band model used to fit all spectra. Color coding; black & red: KW low and high energy spectra, green: HED

### A.2.1 KW spectra

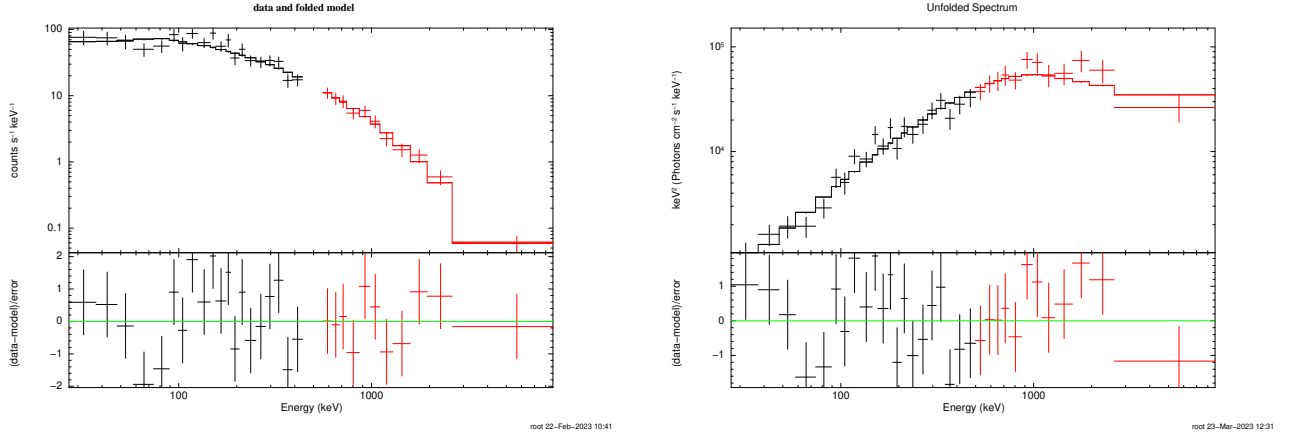


Figure 29: Spectral fit of KW spectra for GRB 190206A. Color coding; black & red: KW low and high energy spectra

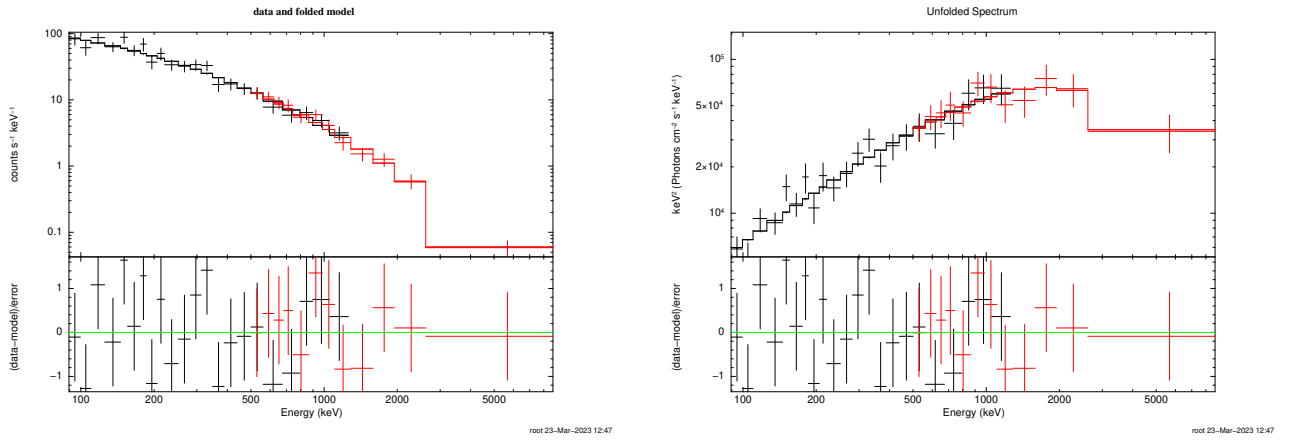


Figure 30: Spectral fit of KW spectra for GRB 190206A. Color coding; black & red: KW low and high energy spectra

### A.3 GRB190305A

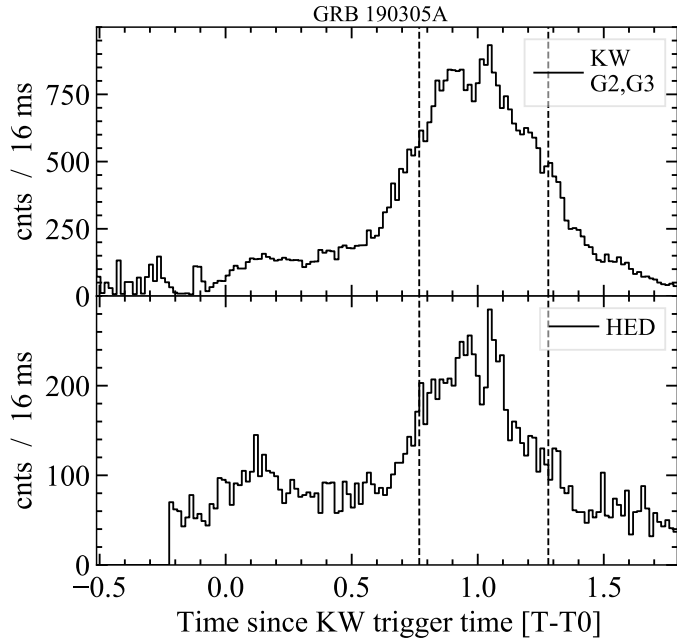
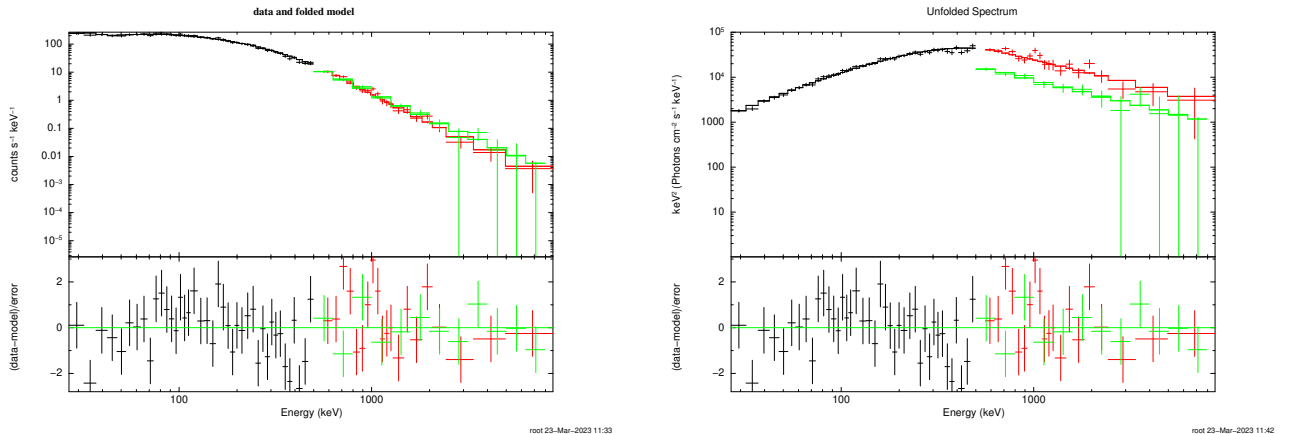


Figure 31:  $T0_{ASIM} = 2019-03-05\ 13:05:20.615$

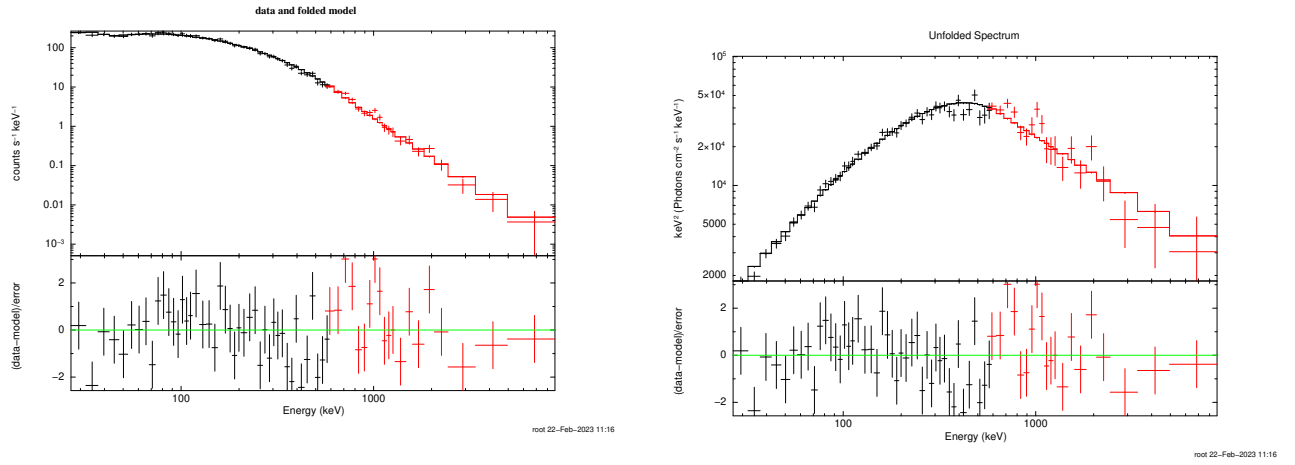


(a) GRB 190305A, data and folded model, interval I

(b) GRB 190305A, unfolded spectrum, interval I

Figure 32: Joint spectral fit of GRB 190305A. Band model used to fit all spectra. Color coding; black & red: KW low and high energy spectra, green: HED

### A.3.1 KW spectra



(a) *GRB 190305A, KW data and folded model, interval I*

(b) *GRB 190305A, KW unfolded spectrum, interval I*

*Figure 33: KW fit of GRB 190305A. Band model used to fit all spectra. Color coding; black & red: KW low and high energy spectra*

#### A.4 GRB 190606A

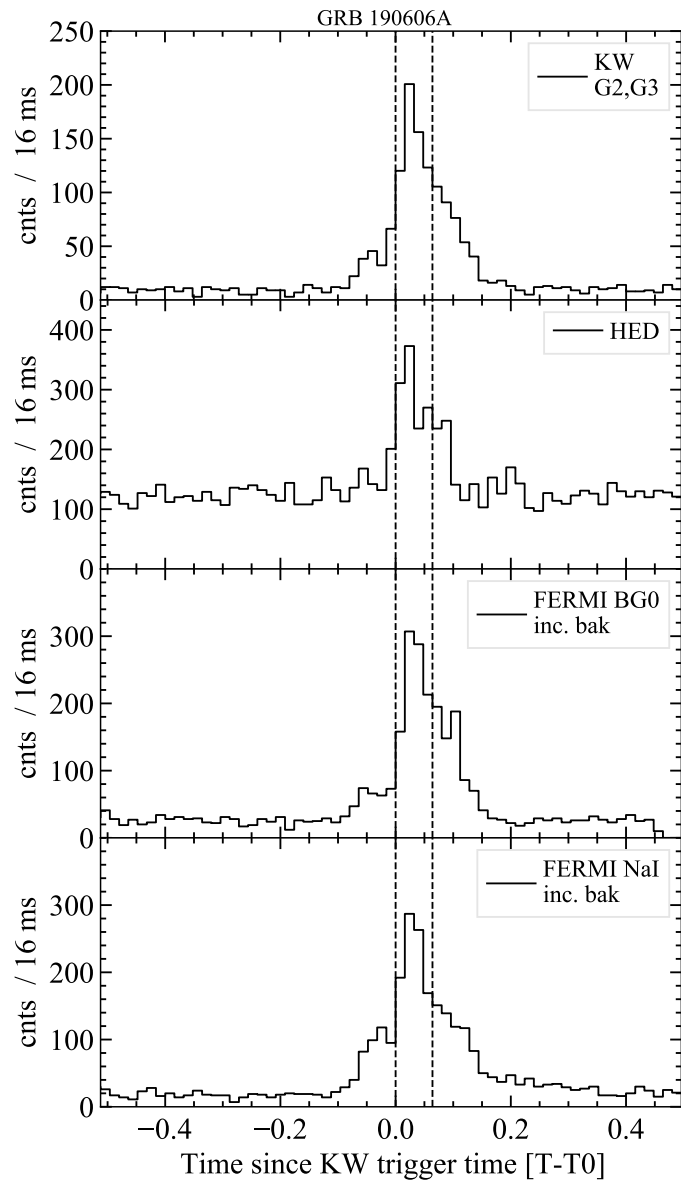


Figure 34:  $T0_{ASIM} = 2019-06-06\ 01:55:06.781$

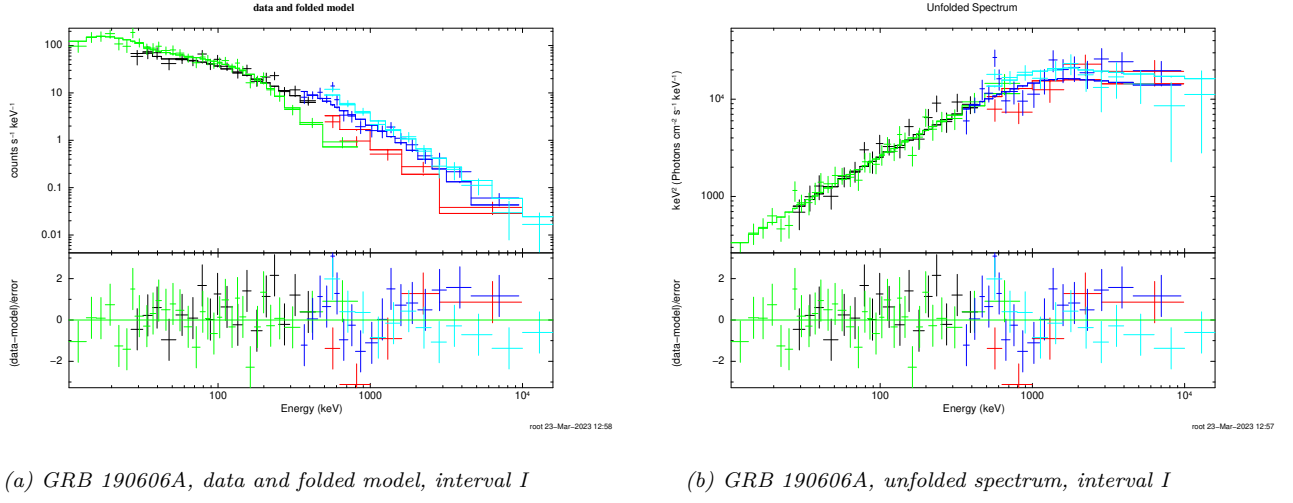


Figure 35: Joint spectral fit of GRB 190606A. Band model used to fit all spectra. Color coding; black & red: KW low and high energy spectra, green: HED

#### A.4.1 KW spectra

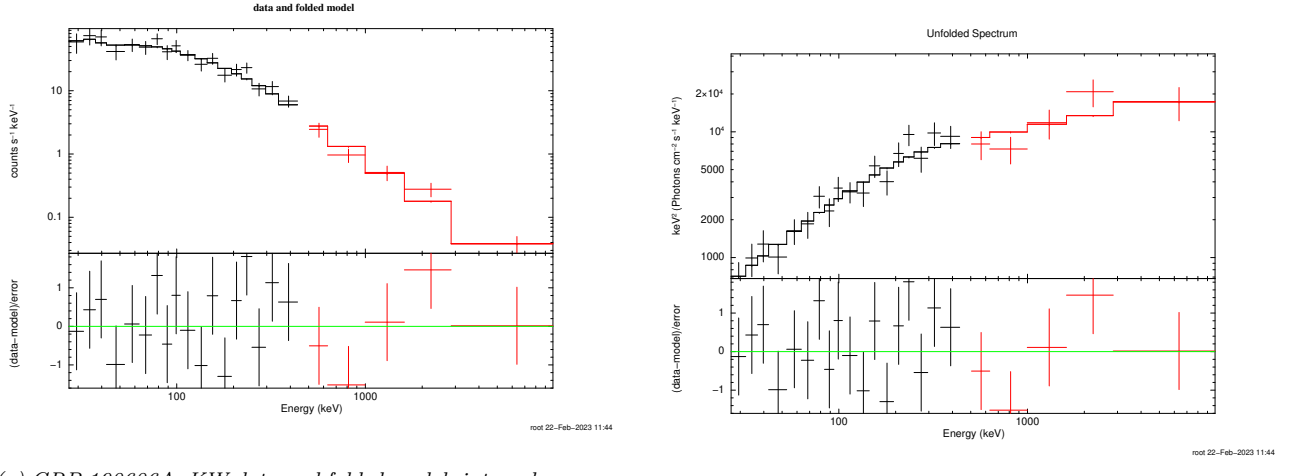


Figure 36: KW fit of GRB 190606A. Band model used to all spectra. Color coding; black & red: KW low and high energy spectra

## A.5 GRB 200521A

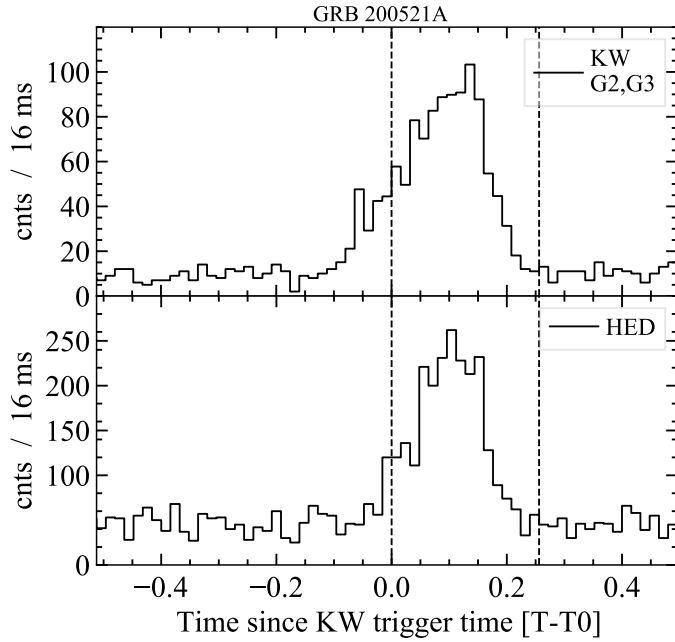


Figure 37:  $T0_{ASIM} = 2020-05-21\ 12:16:39.004$

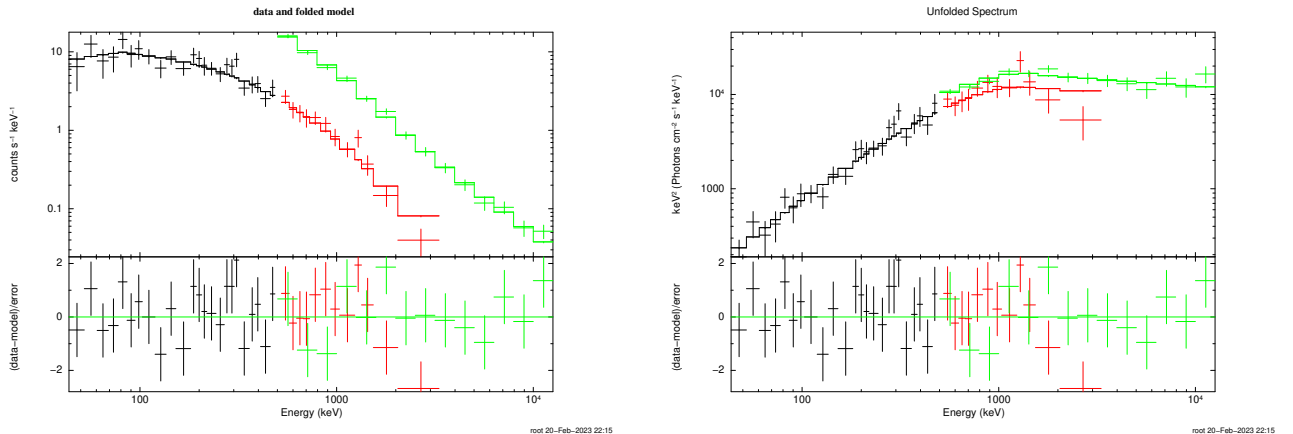
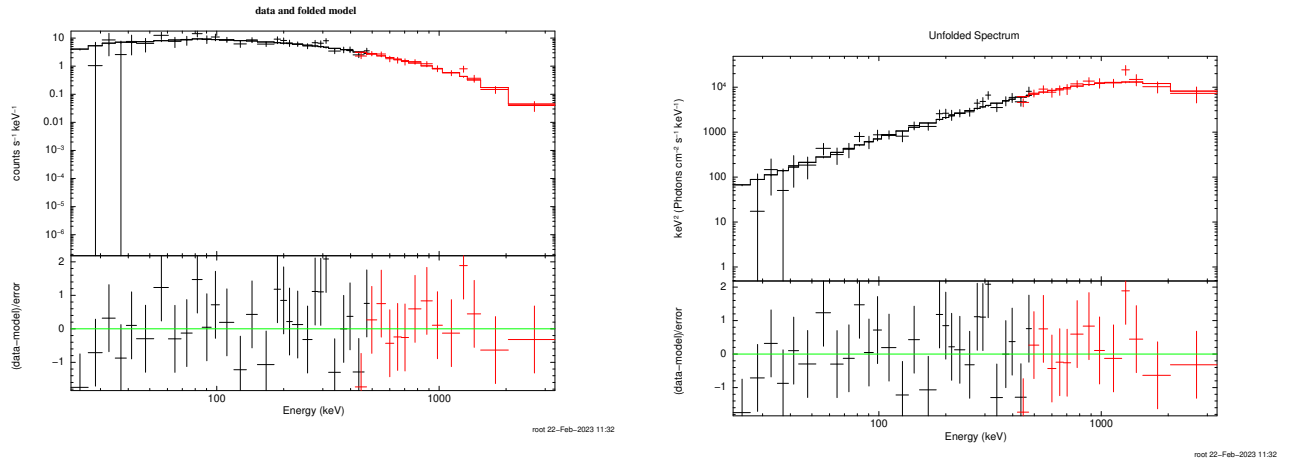


Figure 38: Joint spectral fit of GRB 200521A. Band model used to fit all spectra. Color coding; black & red: KW low and high energy spectra, green: HED

### A.5.1 KW spectra



(a) GRB 200521A, KW data and folded model, interval I

(b) GRB 200521A, KW unfolded spectrum, interval I

Figure 39: Joint spectral fit of GRB 200521A. CPL model used to fit spectra. Color coding; black & red: KW low and high energy spectra

## A.6 GRB 200716C

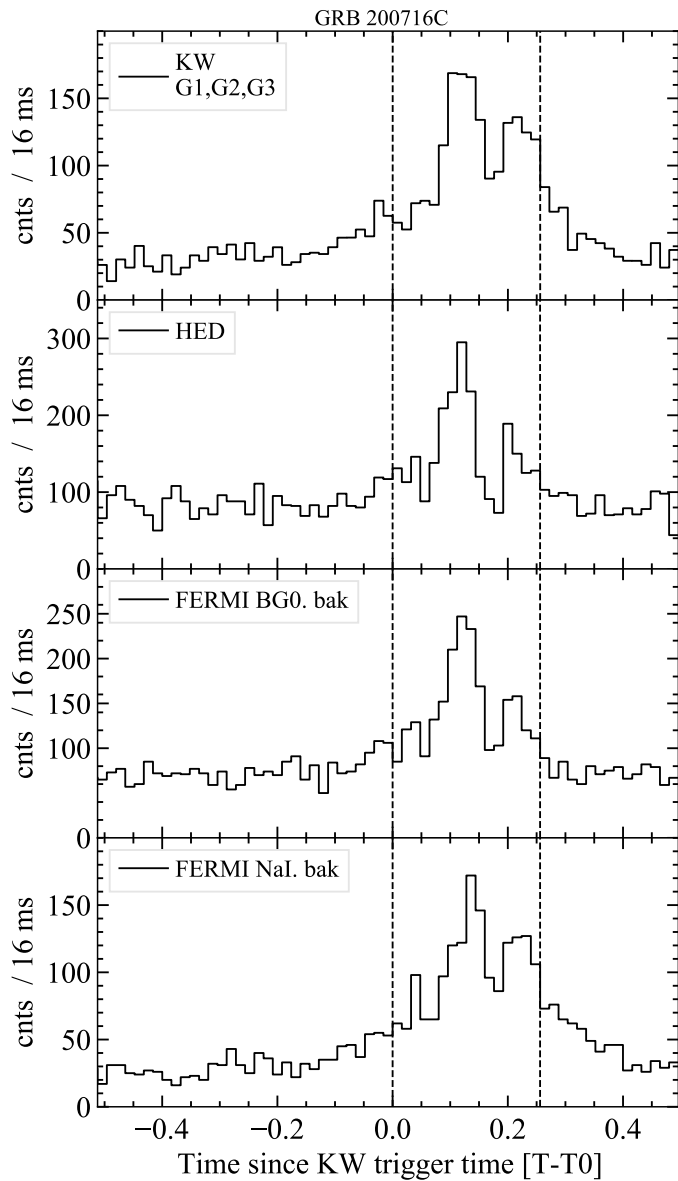


Figure 40:  $T0_{ASIM} = 2020-07-16\ 22:57:39.947$

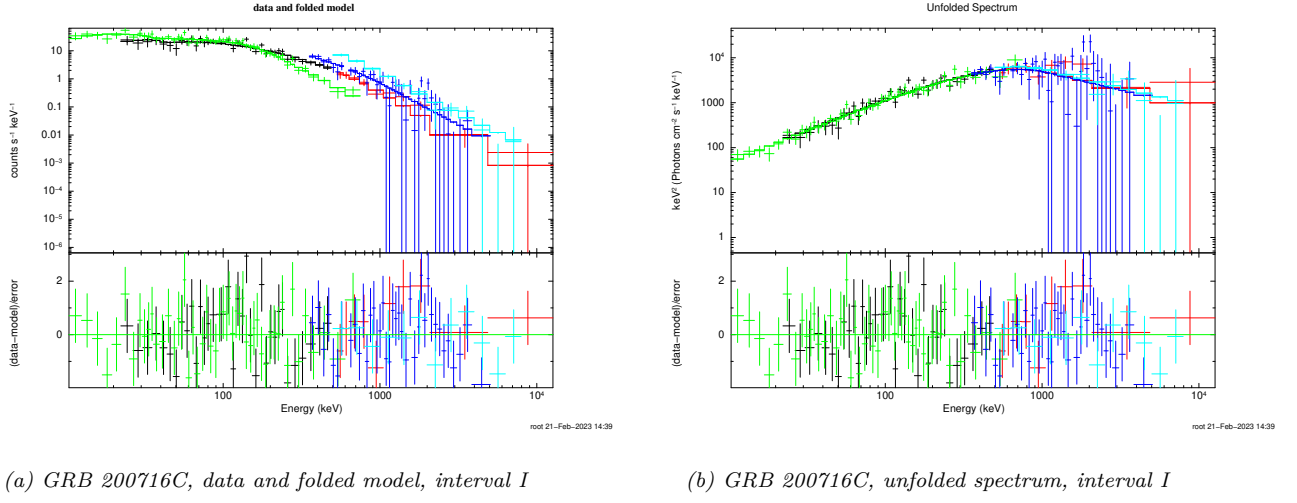


Figure 41: Joint spectral fit of GRB 200716C. Band model used to fit all spectra. Color coding; black & red: KW low and high energy spectra, green: Fermi/GBM NaI, blue: Fermi/GBM BGO, cyan: HED

### A.6.1 KW spectra

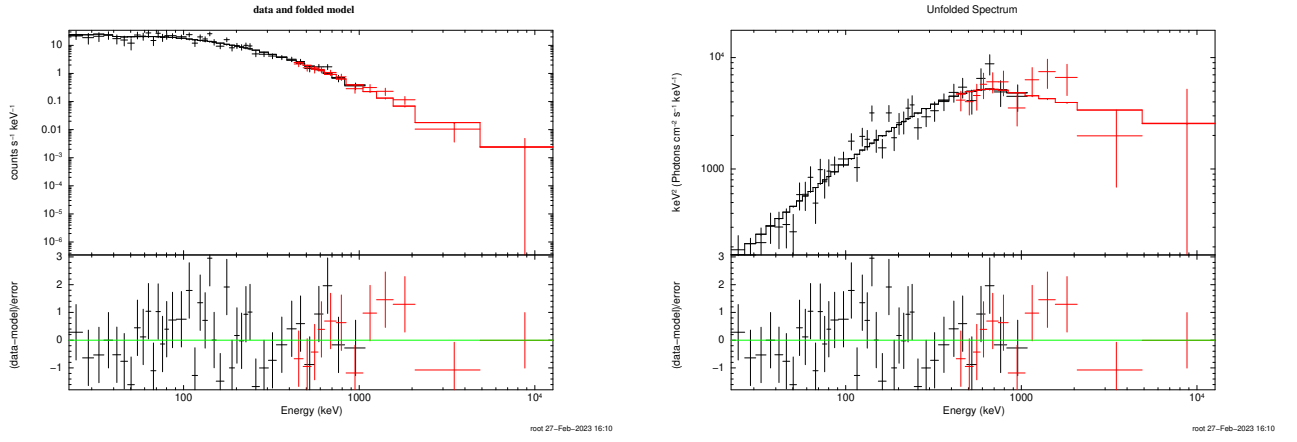


Figure 42: KW fit of GRB 200716C. Band model used to fit all spectra. Color coding; black & red: KW low and high energy spectra

## A.7 GRB 201227A

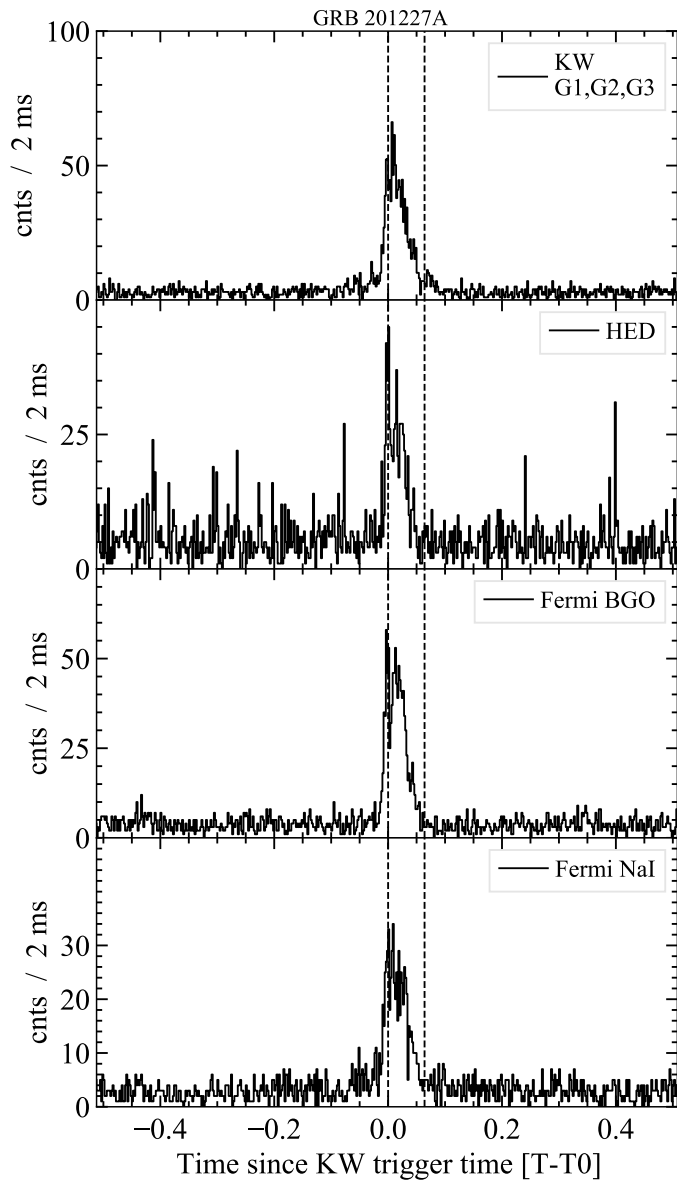


Figure 43:  $T0_{ASIM} = 2020-12-27\ 15:14:06.322$

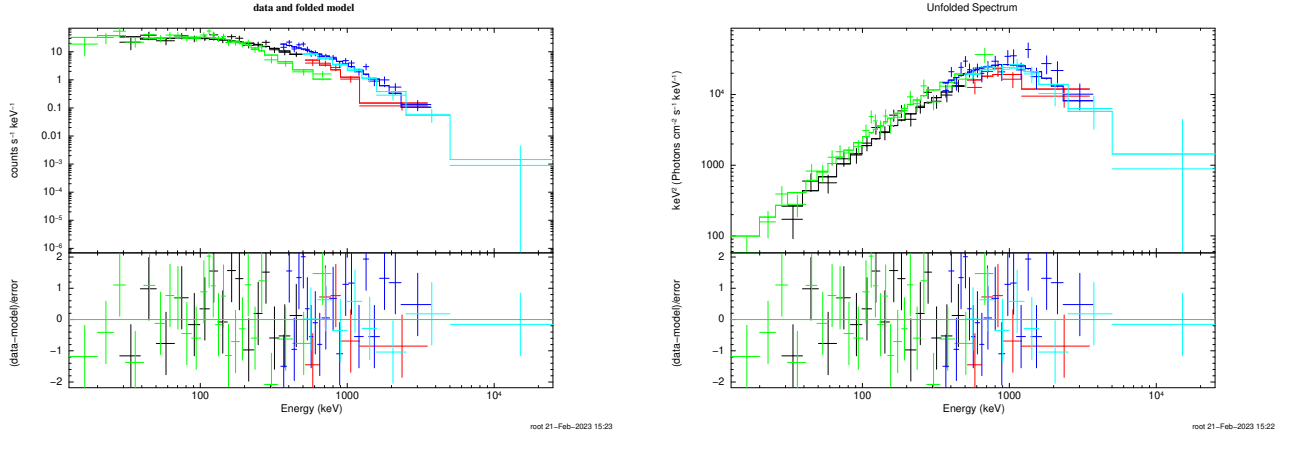


Figure 44: Joint spectral fit of GRB 201227A. Band model used to fit all spectra. Color coding; black & red: KW low and high energy spectra, green: HED

### A.7.1 KW spectra

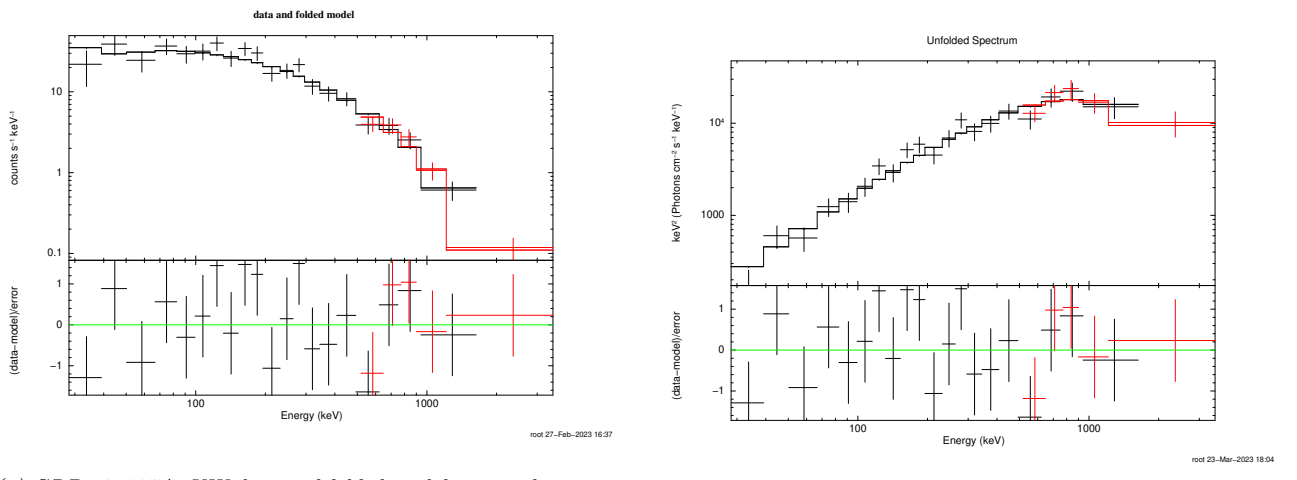
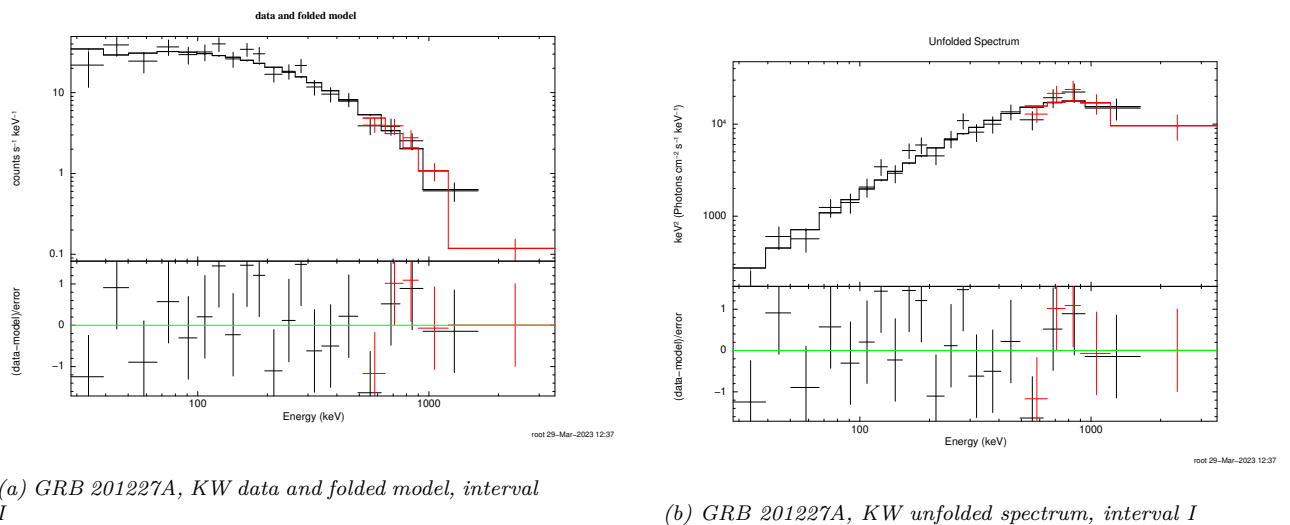


Figure 45: KW fit of GRB 201227A. CPL model used to fit spectra. Color coding; black & red: KW low and high energy spectra



*Figure 46: KW fit of GRB 201227A. Band model used to fit spectra. Color coding; black & red: KW low and high energy spectra*

## A.8 GRB 210619B

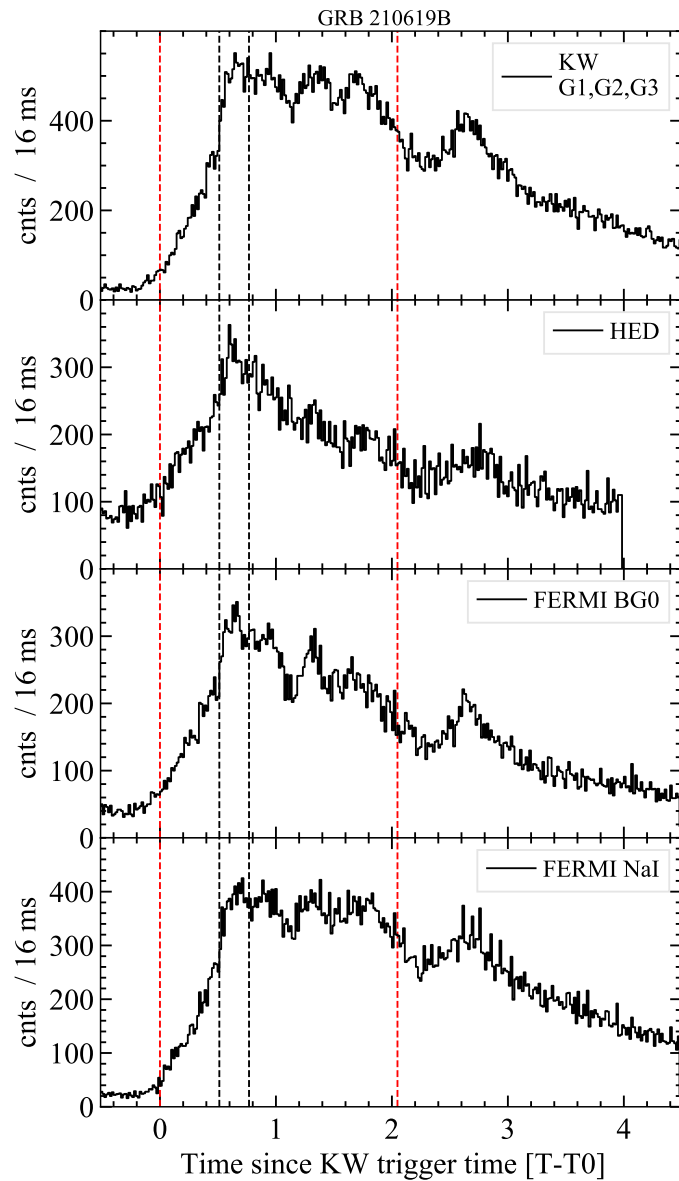
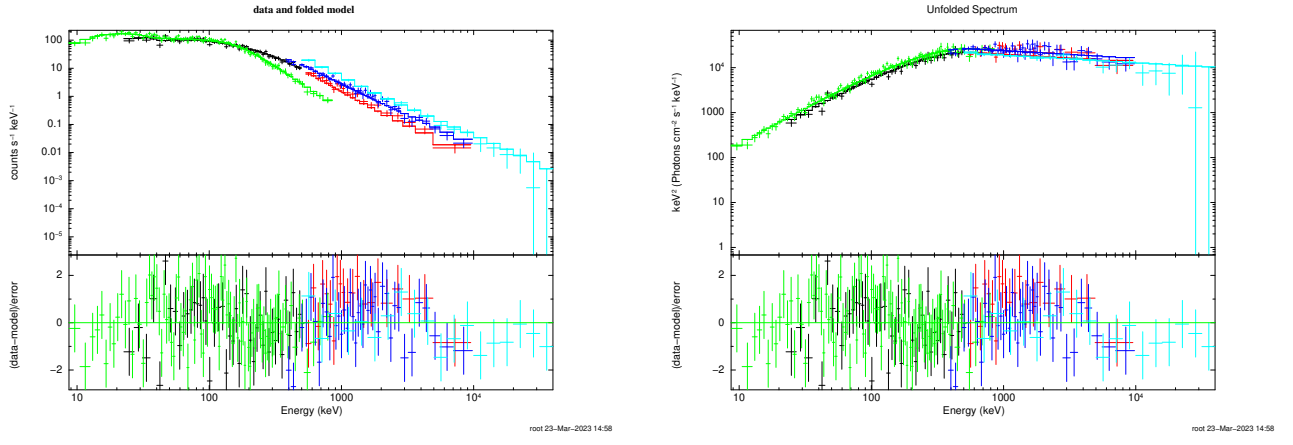


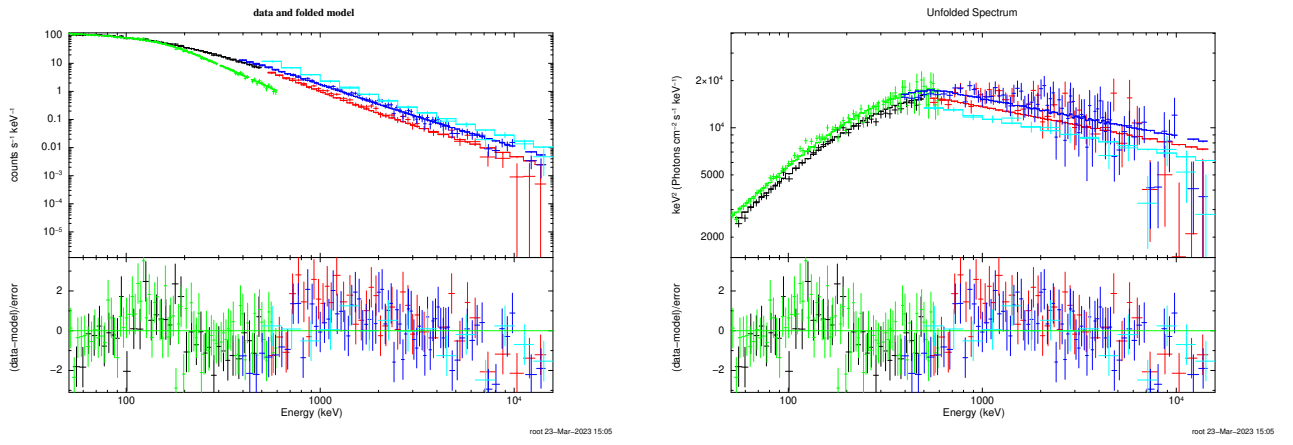
Figure 47:  $T_{0\text{ASIM}} = 2021-06-19 23:59:24.910$ , black dotted line: Interval I, red: Interval II



(a) GRB 210619B, data and folded model, interval I

(b) GRB 210619B, unfolded spectrum, interval I

Figure 48: Joint spectral fit of GRB 210619B on interval I. Band model used to fit spectra. Color coding; black & red: KW low and high energy spectra, green & blue: Fermi/GBM NaI & BGO, cyan: HED



(a) GRB 210619B, data and folded model, interval II

(b) GRB 210619B, unfolded spectrum, interval II

Figure 49: Joint spectral fit of GRB 210619B on interval II. Band model used to fit spectra. Color coding; black & red: KW low and high energy spectra, green & blue: Fermi/GBM NaI & BGO, cyan: HED

### A.8.1 KW spectra

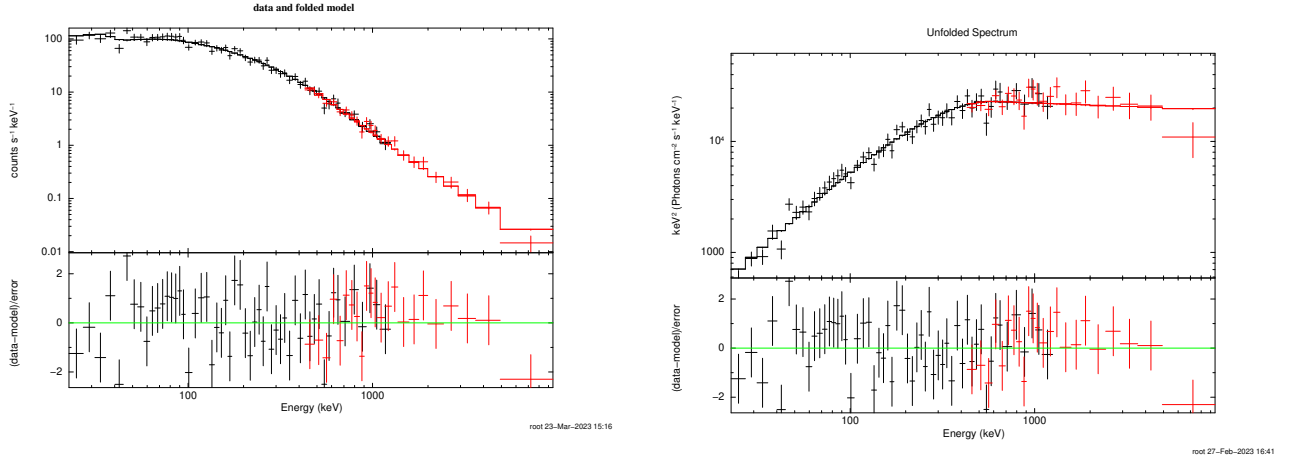


Figure 50: KW fit of GRB 210619B. Band model used to fit spectra. Color coding; black & red: KW low and high energy spectra

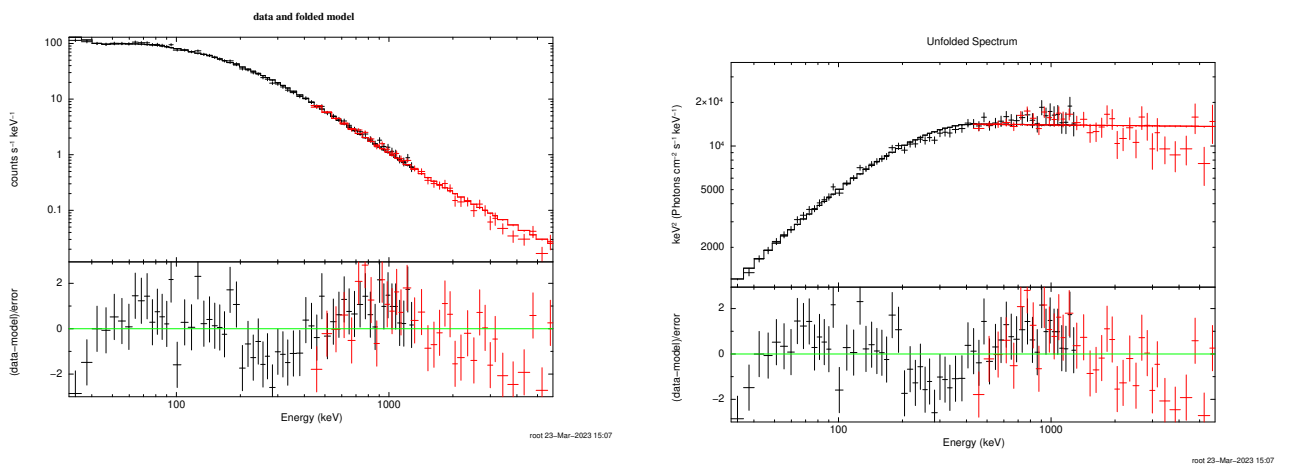


Figure 51: KW fit of GRB 210619B. Band model used to fit spectra. Color coding; black & red: KW low and high energy spectra

## A.9 GRB 211211A

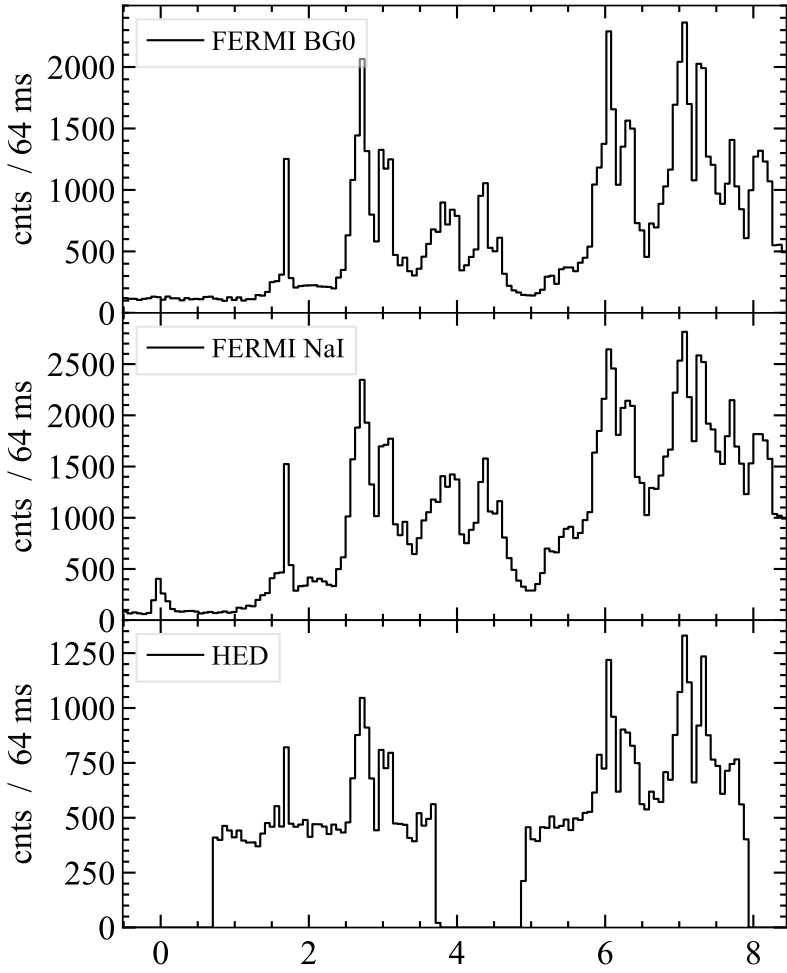
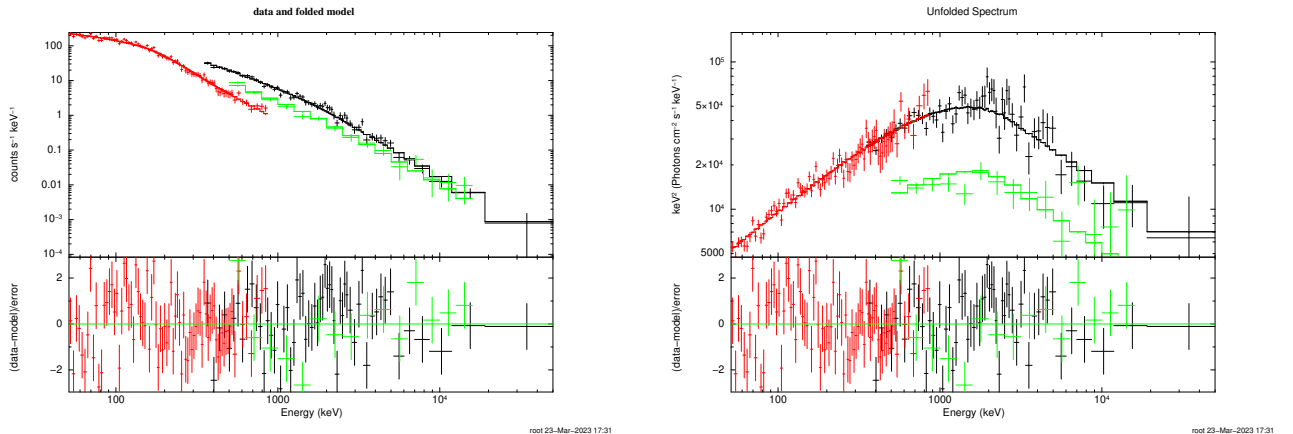


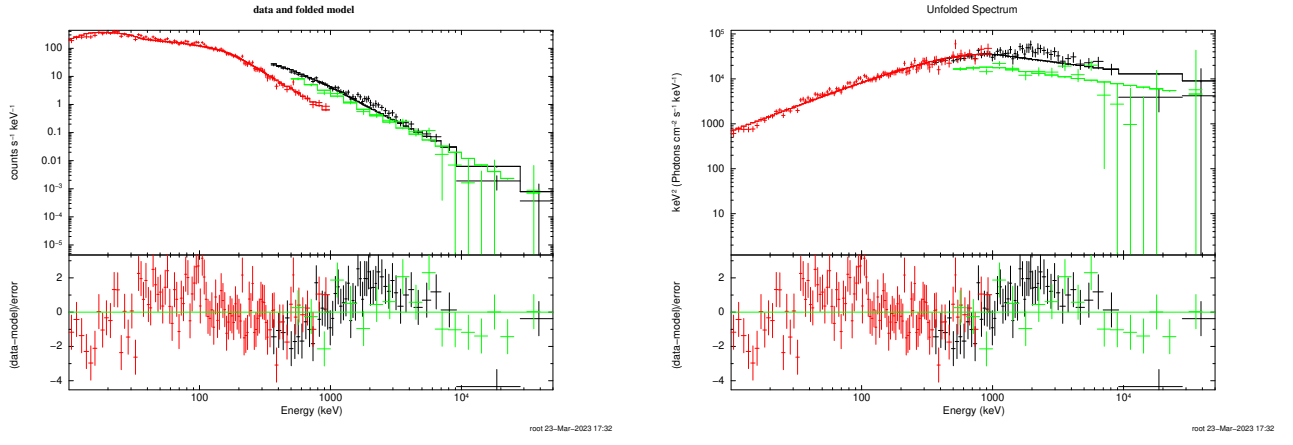
Figure 52:  $T0_{ASIM} = 2021-12-11\ 13:10:03.099$



(a) GRB 211211A, data and folded model, interval 1

(b) GRB 211211A, unfolded spectrum, interval 1

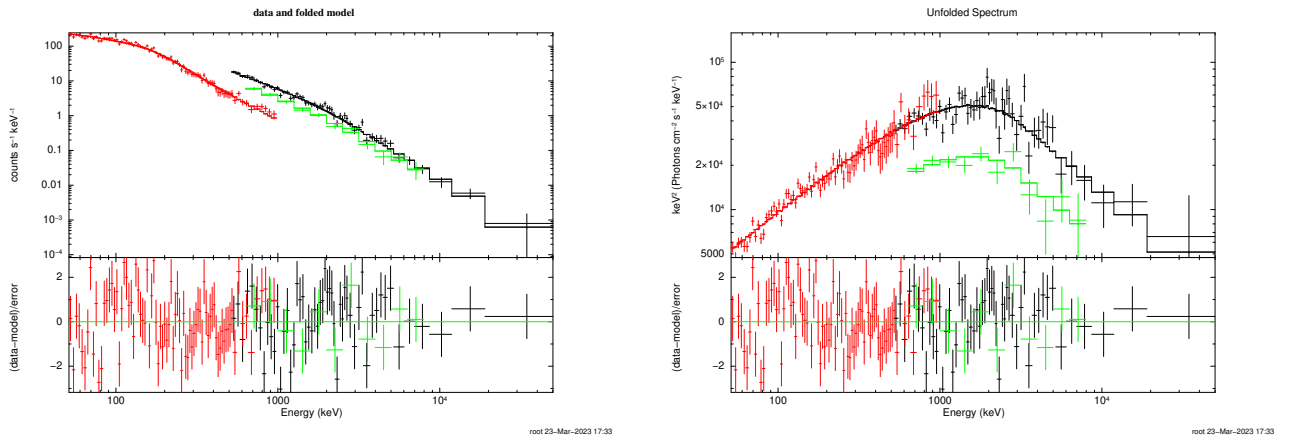
Figure 53: Joint spectral fit of GRB 211211A on interval 1. Band model used to fit spectra. Color coding; black & red: Fermi/GBM NaI & BGO, green: HED



(a) GRB 211211A, data and folded model, interval 2

(b) GRB 211211A, unfolded spectrum, interval 2

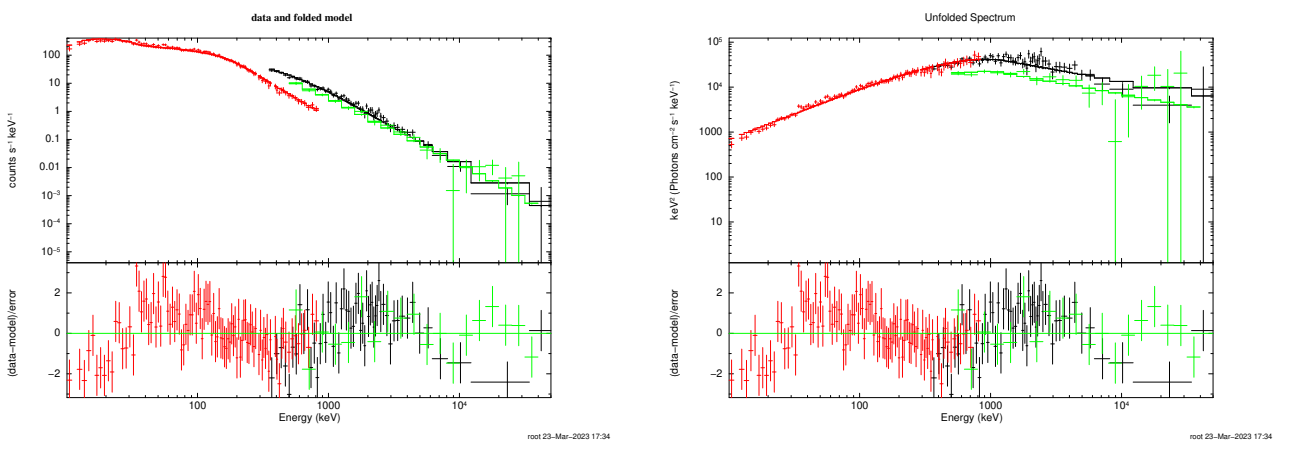
Figure 54: Joint spectral fit of GRB 211211A on interval 2. Band model used to fit spectra. Color coding; black & red: Fermi/GBM NaI & BGO, green: HED



(a) GRB 211211A, data and folded model, interval 3

(b) GRB 211211A, unfolded spectrum, interval 3

Figure 55: Joint spectral fit of GRB 211211A on interval 3. Band model used to fit spectra. Color coding; black & red: Fermi/GBM NaI & BGO, green: HED



(a) GRB 211211A, data and folded model, interval 4

(b) GRB 211211A, unfolded spectrum, interval 4

*Figure 56: Joint spectral fit of GRB 211211A on interval 4. Band model used to fit spectra. Color coding; black & red: Fermi/GBM NaI & BGO, green: HED*

## B ASIM Data Processing and Spectral Analysis Tools

The development of a new framework and effective software for the production of Flexible Image Transport System (FITS) files for ASIM became essential for the efficient analysis of the data obtained from the ASIM mission. FITS files are a standard data format widely used in astronomy, designed to store, transmit, and manipulate scientific data, such as images and spectra. These files are crucial for spectral analysis, as they provide a consistent format that can be easily read and processed by various software tools. In response to this need, a dedicated GitLab repository<sup>15</sup> was created, housing the developed framework and tools for generating and handling ASIM FITS files.

Investing time and effort into creating a robust and user-friendly codebase for the analysis and management of ASIM data has proved invaluable for this thesis. This codebase not only streamlines the data processing and analysis tasks but also facilitates collaboration and knowledge sharing among researchers working on similar projects. The developed code, encompassing the tools and scripts employed in this work, can be accessed through a public GitHub repository<sup>16</sup>. This open-source approach encourages further development and improvement of the code, allowing the broader scientific community to benefit from the advancements made in this thesis.

---

<sup>15</sup> ASIM FITS at GitLab: [https://git.app.uib.no/ASIM-MXGS/asim\\_fits](https://git.app.uib.no/ASIM-MXGS/asim_fits)

<sup>16</sup> GitHub: <https://github.com/AndreasRamsli/GRB>

## References

- B. P. Abbott, R. Abbott, T. Abbott, F. Acernese, K. Ackley, C. Adams, T. Adams, P. Addesso, R. Adhikari, V. B. Adya, et al. Gw170817: observation of gravitational waves from a binary neutron star inspiral. *Physical review letters*, 119(16):161101, 2017.
- S. Agostinelli, J. Allison, K. a. Amako, J. Apostolakis, H. Araujo, P. Arce, M. Asai, D. Axen, S. Banerjee, G. Barrand, et al. Geant4—a simulation toolkit. *Nuclear instruments and methods in physics research section A: Accelerators, Spectrometers, Detectors and Associated Equipment*, 506(3):250–303, 2003.
- R. Aptekar, D. Frederiks, S. Golenetskii, V. Ilynskii, E. Mazets, V. Panov, Z. Sokolova, M. Terekhov, L. Sheshin, T. Cline, et al. Konus-w gamma-ray burst experiment for the ggs wind spacecraft. *Space Science Reviews*, 71:265–272, 1995.
- W. Atwood, A. A. Abdo, M. Ackermann, W. Althouse, B. Anderson, M. Axelsson, L. Baldini, J. Ballet, D. Band, G. Barbiellini, et al. The large area telescope on the fermi gamma-ray space telescope mission. *The Astrophysical Journal*, 697(2):1071, 2009.
- D. Band, J. Matteson, L. Ford, B. Schaefer, D. Palmer, B. Teegarden, T. Cline, M. Briggs, W. Paciesas, and G. Pendleton. Batse observations of gamma-ray burst spectra. i - spectral diversity. *Astrophysical Journal*, 413(2):281–292, 1993.
- E. Bissaldi, A. von Kienlin, G. Lichti, H. Steinle, P. N. Bhat, M. S. Briggs, G. J. Fishman, A. S. Hoover, R. M. Kippen, M. Krumrey, et al. Ground-based calibration and characterization of the fermi gamma-ray burst monitor detectors. *Experimental Astronomy*, 24:47–88, 2009.
- M. Caballero-García, R. Gupta, S. Pandey, S. Oates, M. Marisaldi, A. Ramsli, Y. Hu, A. Castro-Tirado, R. Sánchez-Ramírez, P. Connell, et al. Multiwavelength study of the luminous grb 210619b observed with fermi and asim. *Monthly Notices of the Royal Astronomical Society*, 519(3):3201–3226, 2023.
- A. J. Castro-Tirado, N. Østgaard, E. Göğüş, C. Sánchez-Gil, J. Pascual-Granado, V. Reglero, A. Mezentsev, M. Gabler, M. Marisaldi, T. Neubert, et al. Very-high-frequency oscillations in the main peak of a magnetar giant flare. *Nature*, 600(7890):621–624, 2021.
- G. J. Fishman, P. Bhat, R. Mallozzi, J. Horack, T. Koshut, C. Kouveliotou, G. Pendleton, C. Meegan, R. Wilson, W. Paciesas, et al. Discovery of intense gamma-ray flashes of atmospheric origin. *Science*, 264(5163):1313–1316, 1994.
- N. Gehrels, G. Chincarini, P. e. Giommi, K. Mason, J. Nousek, A. Wells, N. White, S. Barthelmy, D. Burrows, L. Cominsky, et al. The swift gamma-ray burst mission. *The Astrophysical Journal*, 611(2):1005, 2004.
- A. Goldstein, J. M. Burgess, R. D. Preece, M. S. Briggs, S. Guiriec, A. J. van der Horst, V. Connaughton, C. A. Wilson-Hodge, W. S. Paciesas, C. A. Meegan, et al. The fermi gbm gamma-ray burst spectral catalog: the first two years. *The Astrophysical Journal Supplement Series*, 199(1):19, 2012.
- A. Goldstein, W. H. Cleveland, and D. Kocevski. Fermi gbm data tools: v1.1.1, 2022. URL <https://fermi.gsfc.nasa.gov/ssc/data/analysis/gbm>.
- R. J. Gould and G. P. Schréder. Pair production in photon-photon collisions. *Physical Review*, 155(5):1404, 1967.
- D. Gruber, A. Goldstein, V. W. von Ahlefeld, P. N. Bhat, E. Bissaldi, M. S. Briggs, D. Byrne, W. H. Cleveland, V. Connaughton, R. Diehl, et al. The fermi gbm gamma-ray burst spectral catalog: four years of data. *The Astrophysical Journal Supplement Series*, 211(1):12, 2014.
- P. Halpern and N. Tomasello. Size of the observable universe. *Advances in Astrophysics*, 1(3):135–137, 2016.
- B. Harmon, C. Wilson-Hodge, G. Fishman, W. Paciesas, S. Zhang, M. Finger, V. Connaughton, T. Koshut, W. Henze, M. McCollough, et al. The batse earth occultation catalog of low energy gamma-ray sources. In *American Astronomical Society Meeting Abstracts*, volume 199, pages 130–07, 2001.
- A. Hoover, R. Kippen, M. Wallace, G. Pendleton, G. Fishman, C. Meegan, C. Kouveliotou, C. Wilson-Hodge, E. Bissaldi, R. Diehl, et al. Glast burst monitor instrument simulation and modeling. In *AIP Conference Proceedings*, volume 1000, pages 565–568. American Institute of Physics, 2008.

- G. F. Knoll. *Radiation detection and measurement*. John Wiley & Sons, 2010.
- L. Knox, N. Christensen, and C. Skordis. The age of the universe and the cosmological constant determined from cosmic microwave background anisotropy measurements. *The Astrophysical Journal*, 563(2):L95, 2001.
- W. R. Leo. *Techniques for nuclear and particle physics experiments: a how-to approach*. Springer Science & Business Media, 2012.
- A. Lindanger, M. Marisaldi, D. Sarria, N. Østgaard, N. Lehtinen, C. Skeie, A. Mezentzev, P. Kochkin, K. Ullaland, S. Yang, et al. Spectral analysis of individual terrestrial gamma-ray flashes detected by asim. *Journal of Geophysical Research: Atmospheres*, 126(23):e2021JD035347, 2021.
- V. Lipunov, J. Gorosabel, M. Pruzhinskaya, A. d. U. Postigo, V. Pelassa, A. Tsvetkova, I. Sokolov, D. Kann, D. Xu, E. Gorbovskoy, et al. The optical identification of events with poorly defined locations: the case of the fermi gbm grb 140801a. *Monthly Notices of the Royal Astronomical Society*, 455(1):712–724, 2016.
- C. Meegan, G. Lichti, P. Bhat, E. Bissaldi, M. S. Briggs, V. Connaughton, R. Diehl, G. Fishman, J. Greiner, A. S. Hoover, et al. The fermi gamma-ray burst monitor. *The Astrophysical Journal*, 702(1):791, 2009.
- T. Neubert, N. Østgaard, V. Reglero, E. Blanc, O. Chanrion, C. A. Oxborow, A. Orr, M. Tacconi, O. Hartnack, and D. D. Bhandari. The asim mission on the international space station. *Space Science Reviews*, 215:1–17, 2019.
- N. Østgaard, J. E. Balling, T. Bjørnsen, P. Brauer, C. Budtz-Jørgensen, W. Bujwan, B. Carlson, F. Christiansen, P. Connell, C. Eyles, et al. The modular x-and gamma-ray sensor (mxgs) of the asim payload on the international space station. *Space Science Reviews*, 215:1–28, 2019.
- W. S. Paciesas, C. A. Meegan, G. N. Pendleton, M. S. Briggs, C. Kouveliotou, T. M. Koshut, J. P. Lestrade, M. L. McCollough, J. J. Brainerd, J. Hakkila, et al. The fourth batse gamma-ray burst catalog (revised). *The Astrophysical Journal Supplement Series*, 122(2):465, 1999.
- G. B. Rybicki and A. P. Lightman. *Radiative processes in astrophysics*. John Wiley & Sons, 1991.
- T. Sakamoto, V. Pal’Shin, K. Yamaoka, M. Ohno, G. Sato, R. Aptekar, S. D. Barthelmy, W. H. Baumgartner, J. R. Cummings, E. E. Fenimore, et al. Spectral cross-calibration of the konus-wind, the suzaku/wam, and the swift/bat data using gamma-ray bursts. *Publications of the Astronomical Society of Japan*, 63(1):215–277, 2011.
- D. Sarria, P. Kochkin, N. Østgaard, N. Lehtinen, A. Mezentsev, M. Marisaldi, E. Carlson, Brant, C. Maiorana, K. Albrechtsen, T. Neubert, et al. The first terrestrial electron beam observed by the atmosphere-space interactions monitor. *Journal of Geophysical Research: Space Physics*, 124(12):10497–10511, 2019.
- I. B. Strong, R. W. Klebesadel, and R. A. Olson. A preliminary catalog of transient cosmic gamma-ray sources observed by the vela satellites. *The Astrophysical Journal*, 188:L1, 1974.
- R. Sunyaev and L. Titarchuk. Comptonization of x-rays in plasma clouds-typical radiation spectra. *Astronomy and Astrophysics*, 86:121–138, 1980.
- D. Svinkin, D. Frederiks, R. Aptekar, S. Golenetskii, V. Pal’Shin, P. P. Oleynik, A. Tsvetkova, M. Ulanov, T. Cline, and K. Hurley. The second konus-wind catalog of short gamma-ray bursts. *The Astrophysical Journal Supplement Series*, 224(1):10, 2016.
- E. F. Taylor and J. A. Wheeler. *Exploring black holes*, volume 98. Addison Wesley Longman San Francisco, 2000.
- M. Terekhov, R. Aptekar, D. Frederiks, S. Golenetskii, V. Il’inskii, and E. Mazets. The konus-wind and konus-a instrument response functions and the spectral deconvolution procedure. In *AIP Conference Proceedings*, volume 428, pages 894–898. American Institute of Physics, 1998.
- A. Tsvetkova, D. Frederiks, S. Golenetskii, A. Lysenko, P. Oleynik, V. Pal’shin, D. Svinkin, M. Ulanov, T. Cline, K. Hurley, et al. The konus-wind catalog of gamma-ray bursts with known redshifts. i. bursts detected in the triggered mode. *The Astrophysical Journal*, 850(2):161, 2017.

- J. Van Paradijs, P. Groot, T. Galama, C. Kouveliotou, R. Strom, J. Telting, R. Rutten, G. Fishman, C. Meegan, M. Pettini, et al. Transient optical emission from the error box of the  $\gamma$ -ray burst of 28 february 1997. *Nature*, 386(6626):686–689, 1997.
- R. A. Wijers, M. J. Rees, and P. Meszaros. Shocked by grb 970228: the afterglow of a cosmological fireball. *Monthly Notices of the Royal Astronomical Society*, 288(4):L51–L56, 1997.
- B. Zhang. *The physics of gamma-ray bursts*. Cambridge University Press, 2018.
- Z. Zhang, S.-X. Yi, S.-N. Zhang, S.-L. Xiong, and S. Xiao. Tidally-induced magnetar super flare at the eve of coalescence with its compact companion. *The Astrophysical Journal Letters*, 939(2):L25, 2022.